Ice Particle Size and Roughness from Novel Techniques – *In Situ* Measurements and Validation

Jenna Louise Thornton

Centre for Atmospheric and Instrumentation Research

Department of Physics, Astronomy, and Mathematics

University of Hertfordshire

Submitted to the University of Hertfordshire in partial fulfilment of the requirements of the degree of Doctor of Philosophy

July 2016

ABSTRACT

The roughness of ice crystals, defined by small-scale surface roughness and large scale complexity, in high-altitude cloud, has been studied due to its important influence on the radiative properties of ice cloud. The Small Ice Detector 3 (SID-3) created at the University of Hertfordshire was used to measure the characteristics of individual ice crystals *in situ*. These are supplemented by a range of meteorological *in situ* measurements, including temperature, relative humidity, and wind velocity to investigate the influence of atmospheric conditions on ice crystal roughness/complexity.

Since the method of roughness retrieval was novel, for atmospheric ice particles, laboratory experiments were setup to test and improve the characterization techniques. Criteria were set as a result of the laboratory experiments which data was expected to meet for it to be deemed reliable. These criteria and techniques were applied to data collected *in situ* on research aircraft.

A range of degrees of ice crystal roughness were observed over five flights from two campaigns based out of Scotland in 2012 and 2015 (PIKNMIX and CIRCCREX). When all the flights were combined the majority of particles (51%) were categorised as lightly rough; the second most common roughness type was moderately rough (39%). Smooth particles made up 10% of the total particles, and <0.02% were classed as severely rough. When considering a wave-cloud case separately, a similar range of roughness values were seen, however, smooth particles were only observed at the cloud leading-edge where nucleation was expected to occur during the only straight level run of the aircraft to probe this region.

During the same wave-cloud flight smooth particles were more common in supersaturated regions and moderately rough crystals were more common in subsaturated regions, suggesting that crystals are more likely to tend towards rougher values when observed in subsaturated environments (a statistical T-test showed this hypothesis to be statistically significant).

It was found that due to limitations associated with instantaneous measurements, it was challenging to observe how ice particle roughness evolved *in situ*, since the history of the individual crystals was unknown in most cases. Orographic cloud, however, was found to provide a more robust estimation of crystal evolution as a consequence of having sharp-leading edges where nucleation events were expected to occur, and since crystals then follow streamlines, the distance from the sharp-leading edge can act as a proxy for time since nucleation.

Content Page

TABLE OF FIGURES

LIST OF ACRONYMS

2D-C	2-Dimensional Cloud (probe)
2D-S	2-Dimensional Stereo (probe)
AGW	Atmospheric Gravity Wave
AIITS	Aerosol Ice Interface Transition Spectrometer
AIMMS	Aircraft Integrated Meteorological Measurement System
CALIOP	Cloud-Aerosol Lidar with Orthogonal Polarization
CAS	Cloud and Aerosol Spectrometer
CAS-DPOL	Cloud and Aerosol Spectrometer with Depolarization
CAST	Coordinated Airborne Studies in the Tropics
CCD	Charge-Coupled Device
CDP	Cloud Droplet Probe
CIN	Cloud Integrating Nephelometer
CIP	Cloud Imaging Probe
CIRCCREX	Cirrus Coupled Cloud-Radiation Experiment
COSMICS	Cold-air Outbreak and sub-Millimetre Ice Cloud Study
CPI	Cloud Particle Imager
DMT	Droplet Measurement Technologies
FAAM	Facility for Airborne Atmospheric Measurements
FSSP	Forward Scattering Spectrometer Probe
GIN	GPS-aided Inertial Navigation system
GLCM	Grey-Level Co-occurrence Matrix
HOLODEC	HOLOgraphic DEtector for Clouds
HYSPLIT	Hybrid Single Particle Lagrangian Integrated Trajectory model
ICCD	Intensified Charge-Coupled Device
ICE-D	Ice in Clouds Experiment – Dust
IN	Ice Nuclei
IPCC	Inter-governmental Panel on Climate Change
LW	Long-Wave (radiation)
MODIS	Moderate Resolution Imaging Spectroradiometer

NASA	National Aeronautics and Space Administration
NOAA	National Oceanic and Atmospheric Administration
PARASOL	Polarization & Anisotropy of Reflectances for Atmospheric Sciences coupled with Observations from a Lidar
PCASP	Passive Cavity Aerosol Spectrometer Probe
PMT	Photo-Multiplier Tube
PN	Polar Nephelometer
PSD	Particle Size Distribution
RH_{ice}	Relative Humidity with respect to ice
RMS/SD	Root-Mean-Square divided by Standard Deviation
SEM	Scanning Electron Microscope
SID	Small Ice Detector
SLR	Straight Level Run
SUCCESS	Subsonic aircraft Contrails and Cloud Effects Special Study
SW	Short-Wave (radiation)
TIFF	Tagged Image File Format
TWC	Total Water Content
VIPS	Video Ice Particle Sampler
WMO	World Meteorological Organisation
WVSS2-F	Water Vapor Sensing Systems Version 2 – Flush inlet
WVSS2-R	Water Vapor Sensing Systems Version 2 – Rosemount inlet

1 Introduction

1.1 Aims

The aim of this thesis research is to study the degree of surface roughness and complexity of ice particles present in high-altitude cloud, and the atmospheric conditions which may influence ice crystal morphology. This is principally achieved by analysing data from the Small Ice Detector 3 (SID-3, discussed in section 2.2) collected *in situ* during two science campaigns out of Prestwick, Scotland on-board the FAAM (Facility for Airborne Atmospheric Measurements) research aircraft. Data from other instruments on the aircraft have also been used, including multiple cloud-probes that are mounted under the wings of the aircraft, and a suite of instruments to provide meteorological information.

The Small Ice Detector 3 (SID-3) can be used to uniquely determine particle size and roughness/complexity from two-dimensional scattering patterns that are imaged when a particle passes through the laser path. The light scattered in the forward direction (6-25°) is directed onto an intensified charge-coupled device (ICCD) (discussed in section 2.2.3). Since this method of retrieval is novel, for atmospheric ice particles, laboratory experiments were also required to test and improve the characterization techniques (discussed in depth in chapter 3).

The motivation for the project is to gain a better understanding of ice-cloud microphysics to contribute to improving the accuracy of global climate models by better representing high-altitude cloud. Ice crystal habits, crystal size, growth processes, and nucleation modes are all important influences on the radiative forcing of clouds; ice crystals with rough surfaces can reflect almost twice as much incident solar SW radiation as smooth surfaces. The difference in the cooling effect between a cloud of only severely roughened ice and a cloud of only smooth ice is comparable to the magnitude of warming by greenhouse gases. This highlights the importance of current and future research into ice particle roughness in cirrus.

1.2 Thesis Outline

This chapter covers the background to the Earth's atmosphere and, in particular, the parts and processes that are relevant to the work in this thesis. There is an emphasis on radiative forcing and the influence that ice clouds and their constituents have on the net effect. Chapter 2 outlines the current and upcoming instruments that can be used to take measurements of atmospheric ice crystals. It also includes an in-depth discussion on how SID-3 operates and how particle characteristics can be retrieved from the data. In Chapter 3 the laboratory experiments to test and

improve the methods used for particle property estimation are presented with results. Chapter 4 discusses the degree of ice crystal roughness observed *in situ* over five different flights. These results are compared to meteorological measurements to investigate possible cause for the different levels of particle roughness. Chapter 5 is a more in-depth investigation of cirrus cloud during only one of the flights. In this chapter the observed ice crystal roughness throughout the cirrus cloud is presented and compared to the atmospheric conditions at the time of ice-crystal observation. The particle size distributions throughout the cloud from different probes are also briefly compared, and used to characterise the cloud. A second case study is presented in Chapter 6, this time the cloud is an orographic cloud formed in the presence of lee waves over the Scottish Highlands. The roughness of ice particles is investigated at the sharp-leading edge of the cloud where nucleation is expected to occur, and is compared to the values further into the cloud. The influence of supersaturation and subsaturation on ice particle roughness is also discussed. The key results are then summarised in Chapter 7 and additional future directions of this work are discussed.

1.3 The Earth's Atmosphere and Interaction with Radiation

1.3.1 Global Energy Budget

The global energy budget quantifies the amount of radiation entering the Earth's climate system from the sun and the amount that is radiated out, and accounts for the remainder within the Earth's atmosphere and at its surface. The incoming radiation is shortwave (SW) which consists of ultraviolet (UV) radiation and, primarily, visible radiation. Approximately 30% of this incoming SW radiation is either reflected by clouds and the Earth's surface, or scattered back out to space by molecules. Another 20% is absorbed by the atmosphere; this includes absorption by clouds, water vapour, aerosol, and ozone, the latter of which protects life at the Earth's surface from many harmful UV rays. The remainder of the SW radiation, around 50% of the incident radiation, is absorbed by the surface itself.

The solar SW radiation that is absorbed by the Earth's surface is re-emitted to maintain thermal equilibrium. This radiation takes the form of longwave (LW) radiation in the infrared (IR) part of the spectrum. This LW radiation is absorbed by clouds and aerosol, which re-emit half of this energy back to the surface and the rest out towards space.

Energy is also transferred from the Earth's surface via sensible heat transfer and latent heat transfer. Sensible heat transfer occurs through conduction between the surface and the atmosphere. Latent

heat is transferred into the atmosphere when the heat absorbed by the oceans to evaporate water is released during condensation of the water vapour, which then precipitates back to the Earth's surface.

The contributions of all of these mechanisms to the global energy budget can be seen in Figure 1.1. All of the outgoing contributions must equal all of the incoming contributions to maintain thermal equilibrium. Any changes in the global energy budget can result in a warming or cooling of the Earth's surface. An example of this is the increase in some greenhouse gases which have caused an increase in the temperature of the Earth's surface observed over the past few decades, as illustrated in Figure 1.2. Greenhouse gases and atmospheric constituents enable a warming of the Earth's surface relative to its temperature if the atmosphere was absent, otherwise known as the Greenhouse Effect.

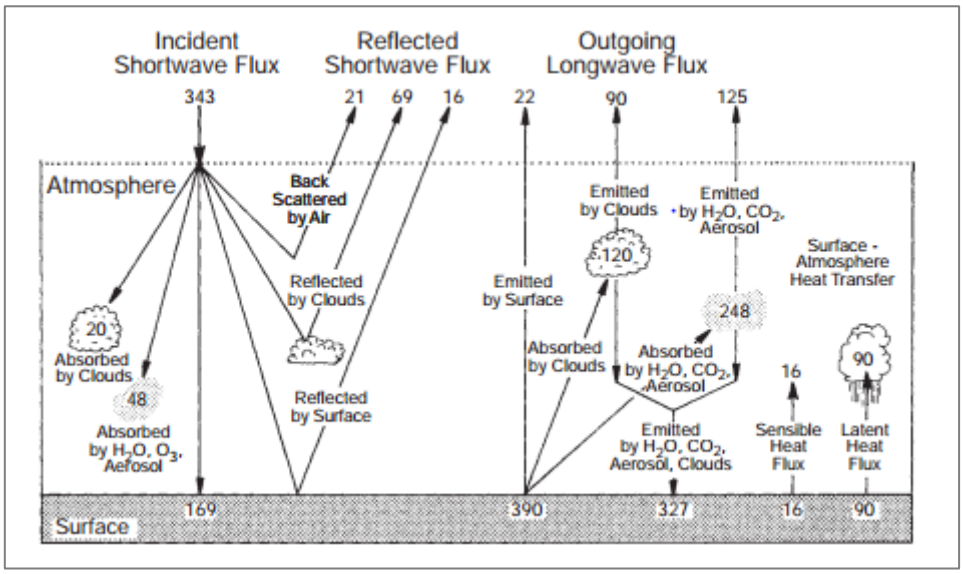

Figure 1.1: Global mean energy budget (Wm-2) (Salby, 2012). The interaction of atmospheric constituents with both SW and LW radiation are represented; the amount of emitted/absorbed radiation for the individual components are shown and given in Wm-2.

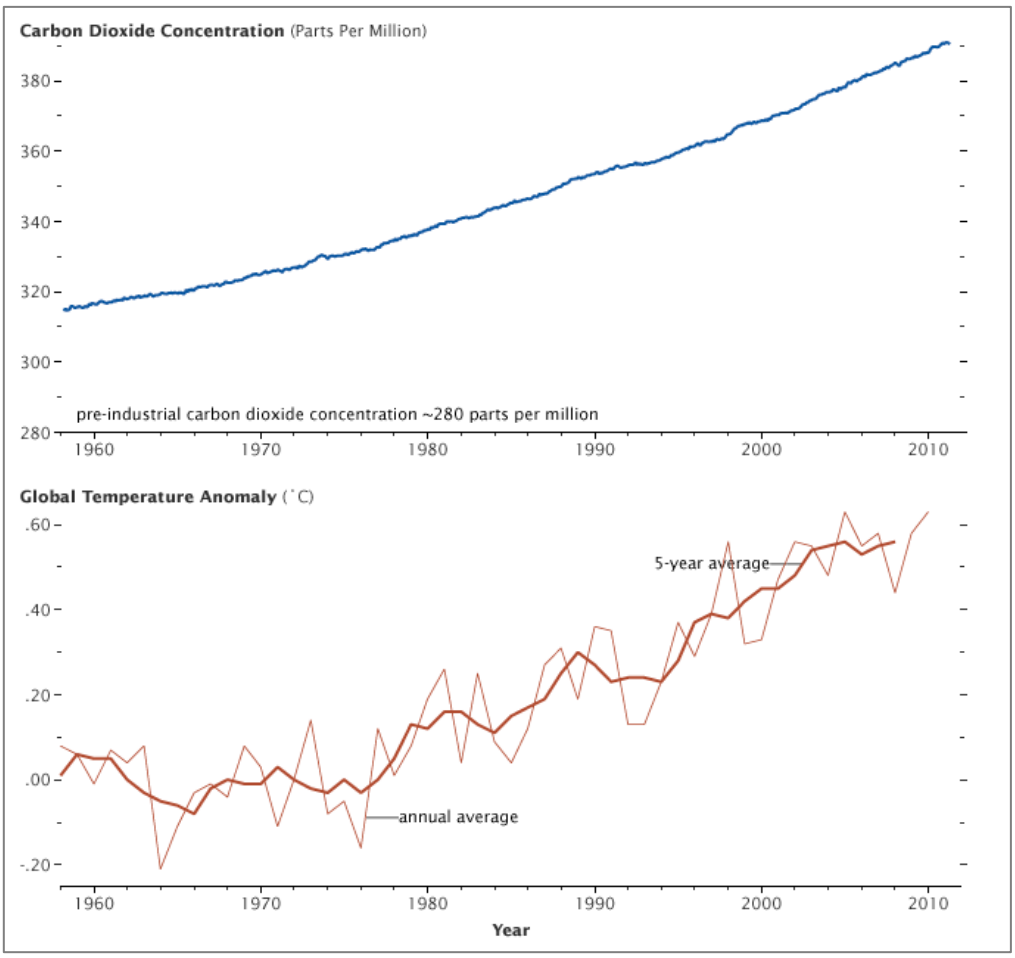

Figure 1.2: Two plots demonstrating the correlation between the increase in CO2 since 1960 and the increase in the average global temperature over the same time period (NASA, 2010). The top plot shows CO2 concentration as a function of time; the bottom plot shows.

1.3.2 Greenhouse Effect

If the Earth is assumed to be in thermal equilibrium then the absorption of SW radiation from the Sun will equal the emitted LW radiation by the Earth. If the portion of SW radiation cut by the Earth's disc is modelled as a beam with a cross-sectional area of πa^2, flux F, and originates at a distance R from the Earth, then the incident radiation at the Earth will be $\frac{F}{R^2}\pi a^2$, of which a fraction, A, is reflected. Therefore the absorbed power is

$$\frac{F}{R^2}\pi a^2 - A\frac{F}{R^2}\pi a^2 = \frac{F(1-A)}{R^2}\pi a^2 \qquad [1.1]$$

To estimate the emitted power by the Earth, the Stefan-Boltzmann law is required

$$\pi B = \sigma T_e^4 \quad [1.2]$$

where πB is the energy flux integrated over wavelength that is emitted by a blackbody of temperature T_e and σ is the Stefan-Boltzmann constant

$$\sigma = 5.67032 \text{ x } 10^{-8}\ Wm^{-2}K^{-4} \text{ (Gordon, 1998)} \quad [1.3]$$

The emitted power can be written

$$4\pi a^2\ \sigma T_e^4 \quad [1.4]$$

Putting the emitted power and the absorbed power equal to each other, and noting that for the Earth R is equal to 1AU, provides an estimate for the effective blackbody temperature of the Earth

$$T_e = \left[\frac{F(1-A)}{4\sigma}\right]^{\frac{1}{4}} \quad [1.5]$$

An incident solar flux of 1372Wm^{-2} (Salby, 2012), and an average albedo of 0.3 (Ahrens, 2012) yield a blackbody temperature of 255K for the Earth, more than 30K colder than the actual global-mean surface temperature of 288K (Salby, 2012).

This increased temperature of the Earth's surface is the consequence of the repeated absorption and re-emission by the Earth's atmosphere of LW radiation from the Earth's surface. The atmosphere is almost opaque to LW radiation which is easily absorbed by the greenhouse gases and cloud; the chief greenhouse gas absorber being water vapour. The LW radiation from the Earth's surface is absorbed by these gases in an atmospheric layer, and is then reemitted in all directions. Consequently, half of the absorbed energy goes into reheating the Earth's surface and the other half is emitted towards space, Figure 1.1. The LW radiation which has been emitted upwards is then absorbed by overlying atmospheric layers, and similarly to the layer below, some of the radiation is emitted upwards and some is emitted downwards towards the Earth's surface. This process repeats until the LW energy is radiated beyond all absorbing layers of the atmosphere. This cycle of absorption and emittance traps LW energy and causes a warming effect to the Earth's surface.

The greenhouse effect is predominantly due to water vapour, which is responsible for the natural greenhouse effect, since it is not created or destroyed. This natural greenhouse effect is necessary to maintain a temperature that can sustain life. However, gases such as carbon dioxide and methane, of which an increasing amount have been introduced in to the atmosphere within the past two hundred years, are responsible for the enhanced anthropogenic greenhouse effect. This additional

warming effect is created since more of the terrestrial LW radiation is trapped below the tropopause, and results in perturbations to the radiative forcing (defined in Section 1.3.3).

1.3.3 Radiative Forcing

The difference between the incoming solar SW radiation and the outgoing terrestrial LW radiation is quantified and referred to as radiative forcing. It is typically defined as the perturbation to the downward energy flux at the top of the troposphere and is measured in units of watts per square meter of the Earth's surface. The IPCC, however, report radiative forcing values as the change in forcing relative to preindustrial conditions defined at 1750 (IPCC AR4, 2007), measured in watts per square metre, which is the definition adopted in this thesis. A positive forcing means there is more incoming solar SW radiation than outgoing terrestrial LW radiation, which corresponds to a warming effect. A negative forcing refers to a cooling of the Earth's surface. The radiative forcing can be altered by multiple influences such as changes in the intensity of incoming solar energy, the reflectivity of clouds, reduction of the Earth's albedo due to deforestation, and the absorption of radiation by greenhouse gases. Some of these changes are due to natural causes, but some are the direct consequence of human activity. The Intergovernmental Panel on Climate Change (IPCC) have attempted to quantify individual contributions to radiative forcing; however some estimates hold large uncertainties. Figure 1.3 shows radiative forcing values of some anthropogenic and natural atmospheric components from the IPCC's fifth assessment report (AR5). As evident in Figure 1.3, the greatest uncertainties in radiative forcing contributions present themselves in aerosol and cloud interactions: the confidence level of the estimated forcing is stated as low. Further research into the microphysics of clouds is required to improve understanding and minimise the level of uncertainty regarding their radiative forcing.

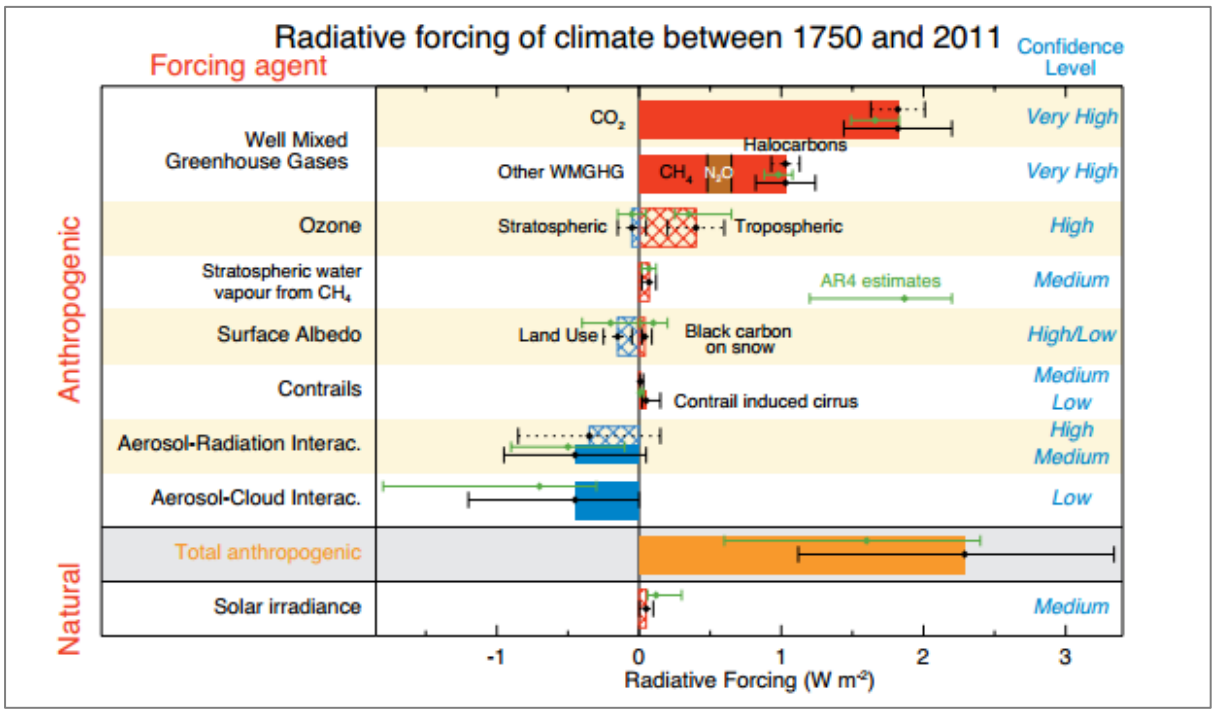

Figure 1.3: Estimate of radiative forcing of anthropogenic and natural atmospheric components from the IPCC AR5 2013

1.3.4 Clouds

At any one time, around half of the Earth is covered by cloud (Salby, 2012). This is illustrated by images collected by the Moderate Resolution Imaging Spectroradiometer (MODIS); Figure 1.4 shows the fraction of an area which was covered by cloud on average over the month of June 2015 can be very high. The instrument views the entire surface of the Earth every one to two days from NASA's Terra satellite which orbits the Earth at a height of around 705km (NASA, 2015a).

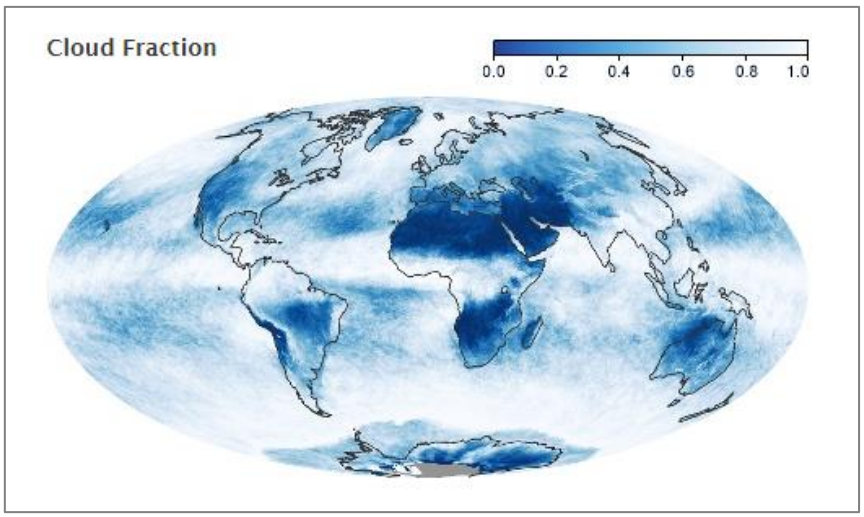

Figure 1.4: The fraction of global cloud cover averaged over month of June 2015, as derived from MODIS data (NASA, 2015b)

Due to these large spatial distributions in cloud coverage (Figure 1.4), the influence of cloud on solar SW radiation, terrestrial LW radiation, and the hydrological cycle are important for atmospheric processes.

On an elementary scale the hydrological cycle involves the evaporation of water, primarily from the Earth's oceans, followed by condensation if clouds are to be formed, and finally resulting in precipitation during which water will return back to the surface of the Earth, Figure 1.5. The formation of clouds during this cycle is important to the redistribution of water, which is necessary to sustain life, and can provide a source of water over the entire surface of the Earth in the form of rain or snow.

Cloud also plays an important role in atmospheric chemical processes. Soluble gaseous pollutants which exist in the atmosphere can be absorbed in cloud droplets and transported to the Earth's surface when the cloud droplets precipitate. Similarly, aerosol pollutants can also be transferred to the surface when they act as condensation nuclei for cloud droplets and ice crystals which then precipitate to the surface; however, although this can improve air quality, it is at the expense of surface hydrology.

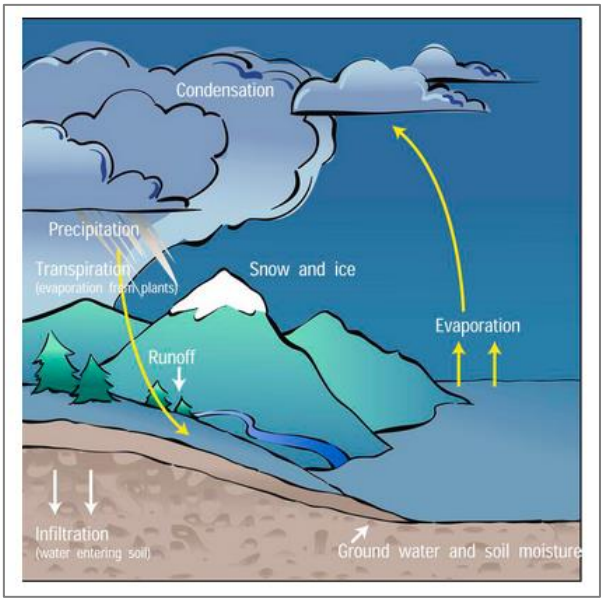

Figure 1.5: A simplified representation of the hydrological cycle (NC-Climate)

Overall, clouds provide a cooling effect; the Earth's surface is cooler than if the atmosphere were free of clouds. However, all clouds create both a heating and a cooling effect, but the degree of each differs between cloud types: high thin cirrus tend to enhance the heating effect, whilst low thick stratocumulus clouds provide an overall cooling effect.

Low clouds tend to have a higher albedo than high clouds since they are generally optically thicker than high clouds. This means they are more efficient at reflecting solar SW radiation and in turn reduce the amount of SW radiation that will reach the Earth's surface and cause a warming effect. The solar SW radiation that does reach the Earth's surface is re-emitted by the Earth as LW radiation, then absorbed and re-emitted by the cloud. The intensity of the emission from the cloud is dependent on the cloud temperature. The cloud-top is generally colder than the Earth's surface, so when introduced into clear-sky they will reduce the amount of outgoing LW radiation to space, trapping energy beneath the cloud. This provides a warming effect, which is more pronounced in high altitude clouds as they have much colder cloud tops.

Although it is known that high clouds mostly increase the Earth's surface temperature whilst low clouds provide the opposite effect, there are uncertainties in the degree of heating/cooling which clouds provide, particularly regarding high altitude clouds: the microphysics of high altitude ice clouds, such as cirrus, tend to be more poorly understood than for low clouds, and further research is required in order to minimise uncertainty regarding their radiative properties. Accurately

quantifying the forcing of clouds, and their contribution to the global energy budget, will improve the reliability of global climate models, and therefore future projections of the Earth's climate.

1.4 Cirrus Clouds

1.4.1 Classification and Properties

The World Meteorological Organisation (WMO), by international agreement, holds the responsibility for classifying clouds. In the troposphere there are ten types of cloud, which have been categorized primarily by morphology. Each of these ten cloud types are further divided into species. Properties such as temperature, altitude, and ice content are not explicitly part of the WMO's definitions, but are recognized as relevant. The ten cloud types can be thought of as either low, medium, or high clouds. The cirrus family, observed at altitudes of around 6km and greater, falls into the high cloud category. The WMO recognize three high altitude clouds and define them as follow:

Cirrus: Detached clouds in the form of white, delicate filaments or white or mostly white patches or narrow bands. These clouds have a fibrous (hair-like) appearance, or a silky sheen, or both.

Cirrocummulus: Thin, white patch, sheet or layer of cloud without shading, composed of very small elements in the form of grains, ripples, etc., merged or separate, and more or less regularly arranged; most of the elements have an apparent width of less than one degree.

Cirrostratus: Transparent, whitish cloud veil of fibrous (hair-like) or smooth appearance, totally or partly covering the sky, and generally producing halo phenomena.

Figure 1.6: Images of different types of cirrus observed and imaged from the ground. Clockwise from top left: cirrus (unicus), cirrus (fibratus), cirrostratus, cirrocumulus (stratiformis), cirrocumulus (lenticularis), cirrostratus (Hamblyn, 2008).

The WMO cloud classification does not include subvisual cirrus or contrail cirrus, although they are well recognised in meteorology. Subvisible cirrus have optical depths of less than 0.03 and area often found at the tropopause. Contrail cirrus are formed from aviation; they are usually; it is usually a consequence of water vapour from aircraft exhaust which can increase the relative humidity above saturation causing the vapour to condense into water droplets which then freeze to form ice if the temperature is low enough.

Although the WMO definitions of clouds are based on morphology, in the meteorological community cirrus clouds have properties which include low optical depth, high altitude with bases at around 5-

6km, and high ice content. These properties are also used to identify cirrus, and are particularly useful when applied to data collected *in situ* where the general appearance of the cloud as a whole is not easily recognisable.

1.4.2 Formation and Evolution of ice clouds

Cirrus clouds are made up of ice particles. How ice particles form depends upon the atmospheric conditions of the environment. Ice can form either by the process of homogeneous nucleation or heterogeneous nucleation.

Homogeneous nucleation is the spontaneous freezing of supercooled water and is expected at temperatures of around -37°C and colder. Heterogeneous nucleation is suspected to be the more common nucleation process since it can occur at temperatures warmer than those required for homogeneous nucleation. Heterogeneous nucleation requires the presence of Ice Nuclei (IN) to form ice. These IN can be either natural or anthropogenic. Common particulates which act as IN are: soot, desert dust, volcanic ash, and bacteria. Heterogeneous nucleation takes place on the surface of the IN in multiple ways, as seen in Figure 1.7, however, the type of IN involved in each of these processes is not fully known, and the properties required of the IN may differ between methods.

During heterogeneous nucleation via the deposition mode, vapour is adsorbed onto the solid surface of the IN, without becoming liquid first. However, in the other three processes, contact nucleation, condensation-freezing nucleation, and immersion-freezing nucleation, the IN causes a supercooled droplet to freeze. In contact nucleation, the IN collides with an existing droplet and causes the droplet to freeze. In condensation-freezing nucleation, water vapour condenses onto the IN, this then acts as an immersion-freezing nuclei, in which the IN already in the droplet causes the droplet to freeze.

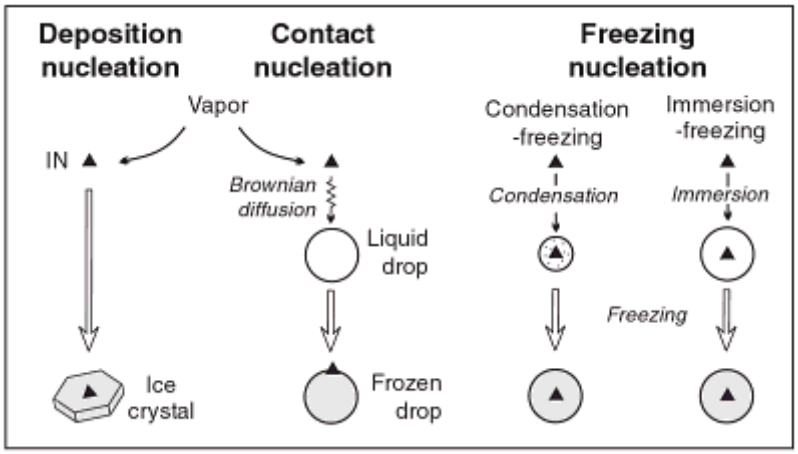

Figure 1.7: Various Methods of Heterogeneous Nucleation to form Ice Particles. Ice Nuclei (IN) are shown as solid triangles and the black dots in the condensation-freezing method represent solute (Lamb & Verlinde, 2011).

Once formed, ice particles can grow rapidly via vapour diffusion. In this case the environment is supersaturated with respect to ice, but subsaturated with respect to water: the saturation vapour pressure with respect to ice is lower than that with respect to water, therefore ice will grow at the expense of droplets since it requires less energy for vapour to leave the droplet than to leave the ice crystal. This is known as the Bergeron process. Ice can also grow by aggregation, where two or more individual ice crystals combine to form an aggregate. Both aggregation and the Bergeron process lead to more massive ice crystals, which are no longer supported by updrafts and fall under gravity. This leads to the organisation of small crystals at cloud-top, and large, often aggregated crystals towards the cloud-base. As the crystals fall through the cloud they will continue to grow via vapour diffusion and aggregation, and may also cause secondary ice formation. Collisions between the falling crystals can lead to splinters of ice breaking off; this creates new ice particles which also grow by the Bergeron process and aggregation, Figure 1.8. In warmer clouds, ice crystal growth and secondary ice formation can occur during the riming process. Riming occurs when an already formed crystal collides with a droplet; it freezes instantly and becomes part of the crystal. The process can also throw off small splinters of ice, which may then grow by the accretion of supercooled droplets, by the Bergeron process, or aggregation. Ice particles which have undergone substantial riming are referred to as graupel and can result in hail or large raindrops depending on the ambient temperature, Figure 1.9.

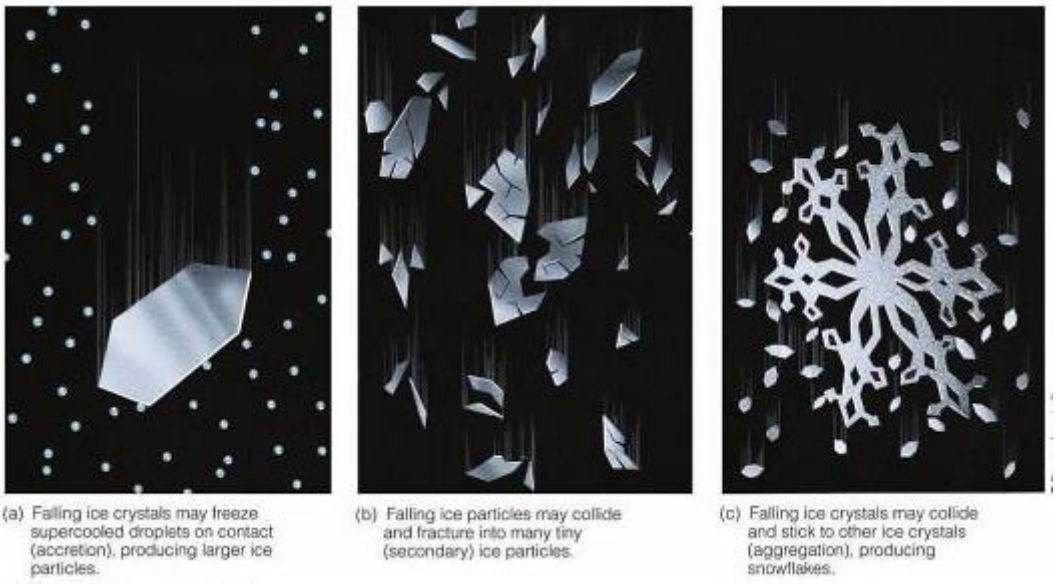

Figure 1.8: The evolution of ice crystals in cold clouds: (a) An ice crystal growing by contact freezing with supercooled droplets; (b) Secondary ice particles formed via the collision of two or more ice particle; (c) An ice crystal growing due to aggregation (Ahrens, 2012).

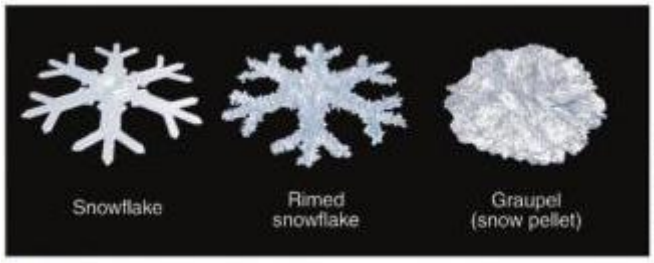

Figure 1.9: Ice undergoing riming from left to right. A substantial amount of riming leads to the crystal becoming graupel (Ahrens, 2012).

Crystals which have become more massive via the methods described above will eventually fall out of the cloud base. This can lead to weather such as rain, snow and hail, depending on the temperatures and humidity at lower altitudes. They may also be used to seed clouds at lower altitudes; the ice crystals can act as contact nuclei and freeze the supercooled droplets below. If heterogeneous nucleation was the cause of the cirrus formation, then it is possible for the ice to evaporate leaving the aerosol which originally acted as an IN to once again become an IN at this lower altitude. The former method of cloud seeding can lead to increased precipitation since crystals are continuing to grow, as in Figure 1.10, but it can also result in evaporation. If the seeded cloud becomes glaciated then there will not be a sufficient amount of droplets to maintain the ice

crystal's growth and the small ice crystals will be unable to precipitate downwards. These crystals will evaporate, leaving a hole in the cloud, which will affect its radiative properties: less SW radiation will be reflected, and less LW radiation will be absorbed.

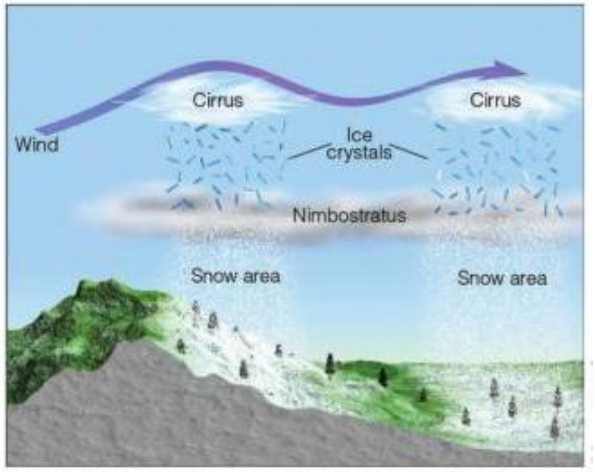

Figure 1.10: Cirrus ice crystals precipitating out of the cirrus cloud and causing natural seeding of a lower altitude cloud. The precipitating crystals continue to grow and fall out of the lower cloud, reaching the ground as snow due to low temperatures (Ahrens, 2012).

Not all precipitating ice crystals will form rain or snow, or result in the formation of a lower altitude cloud. If the crystals precipitate into drier air then they will usually sublimate, i.e. they will go straight from solid to vapour. These falling crystals are known as fallstreaks. These often give cirrus its streaked appearance, Figure 1.11, either due to changes in wind velocity with altitude, and/or changes in the crystals rate of fall at terminal velocity as a consequence of their reduction in mass due to evaporation.

Figure 1.11: High cirrus (castellanus) trailing fallstreaks from the base (Hamblyn, 2008).

1.4.3 Observations of ice cloud

Cirrus clouds represent about 25% of all high clouds (Guignard, et al., 2012) and their coverage at any given time can be 30% in the mid-latitudes (Stubenrauch, et al., 2006), and around 70% in the tropics (Nazaryan, et al., 2008). How they form *in situ* is still an area of uncertainty due to difficulties in observing the evolution of ice particles, i.e. it cannot be known exactly how long ago a particle was nucleated and what atmospheric conditions it has been subject to prior to detection from *in situ* measurements. It is possible to compare *in situ* observations to model outputs to help to determine the likely methods of nucleation. Spichtinger and Gierens (2009) used a model to determine the effect of ice nuclei on the nucleation method. They found that the transition between predominantly homogeneous and heterogeneous ice formation occurs when the heterogenous IN concentration is around $10 litre^{-1}$ ($0.01 cm^{-3}$). Heterogeneously nucleated ice particles tended to be on average larger than homogeneously nucleated crystals, due to fewer crystals competing for water vapour. This was also reported by DeMott et al (1998) who compared model simulations of both homogeneous and heterogeneous nucleation in orographic wave cloud to their observations made during the SUCCESS (Subsonic aircraft Contrails and Cloud Effects Special Study) campaign. They demonstrated that the simulations with heterogeneous nucleation resulted in a large size tail to the ice crystal spectrum and so heterogeneously nucleated crystals are the first to precipitate from clouds. The large crystal sizes observed in the presence of heterogeneous nucleation are a consequence of fewer crystals actually nucleating.

Cirrus formation based on *in situ* observations was modelled by Haag and Kärcher (2004) who found that increasing the number of IN promotes heterogeneous nucleation and suppresses homogenous nucleation which leads to a decrease in number density of ice crystals. Kärcher and Lohmann (2003) also determined that ice nucleation was suppressed when more IN were involved in computations of cirrus formation. The suppression of homogeneous nucleation due to heterogeneous nucleation is suspected to be the cause of high supersaturations in the presence of low ice crystal concentrations which have been observed *in situ* (Krämer, et al., 2009; Immler, et al., 2008; Popp, et al., 2007). Barahona's (2010) model simulations were consistent with *in situ* observations of low crystal concentrations and high supersaturations only when competition between heterogeneous and homogeneous nucleation was a dominant feature.

Whereas cloud formed by heterogeneous nucleation is characterised by low concentrations, homogenous nucleation results in higher concentrations. Hoyle et al (2005) replicated the high number densities measured in cirrus during SUCCESS by assuming that ice nucleation occurred

homogeneously. Barahona et al (2010) also ran simulations of cirrus formation with different IN concentrations. They observed that the ice crystal number density was sensitive to the IN concentrations; it was highest when the IN numbers were low, and at its lowest when there was sufficient IN for heterogeneous nucleation to dominate over homogeneous.

Both observations and model simulations suggest that the type of nucleation may influence the occurrence and life times of clouds; heterogeneous nucleation can reduce the annual mean ice crystal concentration in cirrus by up to 10% at mid-latitudes (Hendricks, et al., 2011) due to efficient sedimentation and precipitation. It is important to understand the nucleation mechanisms and their occurrence since changes in cloud presence can modify their contribution to both the greenhouse effect and the net albedo, therefore affecting their overall contribution to radiative forcing.

Potential heterogeneous nucleation modes have been investigated by comparing model simulations to *in situ* observations (Field, et al., 2012; Cotton & Field, 2002; Eidhammer, et al., 2010), and by laboratory experiments using cloud chambers (Field, et al., 2006; Möhler, et al., 2006; Connolly, et al., 2009). The *in situ* data were all collected during flights in which wave clouds were penetrated. The airflow is, theoretically, laminar in wave clouds so there is little mixing or sedimentation, therefore they can provide a reliable insight into ice nucleation. Simulations of condensation/immersion freezing nucleation were in good agreement with the observations (Eidhammer, et al., 2010; Field, et al., 2012). Eidhammer suspected this mode of nucleation because the high supersaturations led to activation of aerosols to droplets, only after which ice crystals were detected. However, they did not completely rule out deposition as a form of nucleation at the cloud edge. Condensation-immersion freezing nucleation was also dominant in the cloud chamber experiments using Asian, Saharan and Arizonan dust as IN, at temperatures warmer than -33°C (Connolly, et al., 2009) and warmer than -40°C (Field, et al., 2006). At temperatures colder than -40°C, however, deposition nucleation on dust became an increasingly important process (Field, et al., 2006; Möhler, et al., 2006). At colder temperatures still, -49°C to -76°C, deposition nucleation was the dominant mode observed by Möhler et al (2006) on Asian and Saharan desert dust. Reducing the temperature resulted in the activation of more IN (Field, et al., 2012); less than 0.01% of dust activated as IN at temperatures warmer than -12°C (Connolly, et al., 2009).

Since heterogeneous nucleation typically produces larger crystals which sediment efficiently, and homogenously nucleated particles tend to be smaller, the nucleation mode and growth processes can influence the particle size distributions (PSDs) in ice cloud. Cirrus has often been observed to have bimodal ice particle size spectra with a minimum around 150µm (Arnott, et al., 1994; McFarquhar & Heymsfield, 1996; Cotton, et al., 2013). When vapour diffusion is the dominant

growth process, the mean size in the small mode is relatively low and constant and tends to dominate at the cloud-top. The larger mode dominates near the cloud-base suggesting that the bimodal distribution is a consequence of a balance between the nucleation of ice particles and the removal of ice particles by aggregation and diffusional growth (Mitchell, et al., 1996). However, small aggregates have been observed at the cloud-top in deeply convective cirrus (Connolly, et al., 2005; Gayet, et al., 2012).The aggregates which had maximum chain lengths of around 300µm to 600µm and a chain-like appearance, were seen in the highly-electrified continental regions, but were not present in the maritime regions which are typically less-electrified. It was, therefore, proposed that the intense electric fields generated in deeply convective clouds were responsible for aggregation (Connolly, et al., 2005; Gayet, et al., 2012). Several researchers have observed these small chain-like aggregates at temperature below -37°C, and are suggested to be a result of large updrafts (Connolly, et al., 2005; Gayet, et al., 2012; Stith, et al., 2002). The updrafts would lift supercooled droplets which then freeze homogeneously when they reach a temperature of around -37°C, resulting in the high concentrations of small particles that were observed.

In the absence of intense electric fields, ice particle habit would more typically be a consequence of temperature and ice supersaturation (Keller & Hallett, 1982; Hallett, 1987; Bailey & Hallett, 2002; 2004; 2009). The latter study compared data collected *in situ* during the second Alliance Icing Research Study (AIRS II) to previous observations and laboratory experiments to create their most current ice crystal habit diagram. Images of ice crystals in mixed phase cloud and cirrus were taken using a CPI (Cloud Particle Imager) over the south-east of Canada. Cloud temperature ranged from 0°C down to -50°C. They observed that crystals which nucleated at temperatures below -40°C had columnar features, whereas crystals nucleating between -40°C and -20°C tended to have plate-like features. However, crystals which had nucleated in the columnar regime, but had precipitated to warmer regions such that they were then in the plate-like regime, maintained columnar features, but would become capped or skirted with plate-like structures. A crystal growth experiment was set up in laboratory conditions to assess the effect on crystals moving into the plate-like regime from the columnar regime. They found that crystals, which were originally nucleated in conditions intermediate to water and ice saturation, would become solid or grow plate-like caps on their ends as they underwent an increase in temperature to the plate-like regime. Crystals which were originally nucleated nearer to water saturation would later become hollow and would sometimes grow plate-like skirts around the open ends. Baker and Lawson (2006) observed bullet rosettes which had become complex with features such as side plane growth at temperatures warmer than -40°C in a wave cloud. At temperatures below -40°C they observed budding rosettes, pristine bullet rosettes, and short columns, as predicted by Hallet and Bailey (2009). Changes in ice crystal shape

around -40°C were also observed by Van Diedenhoven (2012) from satellite measurements of polarized reflectance relating to a change in the freezing mechanism.

Using a Laboratory Cloudscope instrument, Bailey and Hallett (2009) found that crystals which were once poorly resolved and therefore assumed to be approximately spherical, were actually compact polyhedra with many small facets and irregular structures on their surfaces. These crystals are generally smaller than 50µm and are present at low temperatures and low supersaturations. Baker and Lawson (2006) mirrored the findings of Hallet and Bailey as they observed polyhedral crystals of sizes less than 50µm at temperatures lower than -40°C. They hypothesised that this was due to supercooled droplets freezing quickly at -40°C so that they did not reach an equilibrium state for the development of hexagonal and rectangular facets. It is important to note, however, that the morphologies of particles smaller than about 50µm have previously been difficult to observe *in situ* due to limitations of cloud probes such as the Cloud Particle Imager (CPI). Diffraction, optical aberrations, constrained depth of field (Kaye, et al., 2008; Connolly, et al., 2007), and shattering of ice particles on probe housings (Korolev, et al., 2011) make the assessment of small ice crystal characteristics not fully reliable. The Small Ice Detector 3, described fully in chapter 2, is able to combat some of these issues by imaging scattering patterns of particles from which particle size can be determined down to a few microns.

1.4.4 Contribution of ice clouds to Radiative Forcing

Ice crystals with different morphologies can have contrasting effects on the magnitude of radiative forcing (defined in Section 1.3.3): whereas cirrus consisting of relatively large crystals exhibits positive cloud radiative forcing, contrail-induced cirrus with very large numbers of small ice particles can have a negative forcing (Zhang, et al., 1999). Zhang et al (1999) found that cirrus with single-modal PSD tended to exhibit a greater forcing than if the size spectra were bimodal. PSDs were used as a proxy for sedimentation rates to model how they affect the cloud forcing by Mitchell et al (2008). It was shown that less sedimentation, and higher concentrations of small crystals with diameters less than 60µm, could increase cloud ice by 12% and global cirrus cloud cover by 5.5%. This resulted in an increase in cloud albedo and, subsequently, reflected SW radiation, however, the more extensive cloud cover also acted to enhance the greenhouse effect. Similar results were found by Sanderson et al (2008) and Jakob (2002) whilst altering ice crystal fall speeds in global model simulations. Both found that reducing crystal fall speeds lead to globally increased cloud cover,

reducing the degree of LW radiation emitted to space, but increasing the amount of SW radiation reflected back out.

The IN concentration can have a significant effect on cirrus cloud forcing by encouraging heterogenous nucleation and resulting in fewer but larger ice crystals which reduce the cloud albedo. Haag and Kärcher (2004) found that this reduction in cloud albedo could modify the net cloud forcing by several Wm^{-2} and perhaps lead to a sign change. Jensen et al (2001) found IN concentrations greater than $0.1cm^{-3}$ would result in an increase in cloud forcing and in the presence of relatively few IN the net radiative flux would actually reduce by several Wm^{-2}. This is a result of an increase in frequency of thin and subvisible cirrus when few IN are present; when IN are increased the occurrence of these optically thin clouds drops. The impact of IN becomes particularly prevalent if nucleation occurs near ice saturation, at low temperature, and/or in weak updraughts (Haag & Kärcher, 2004). Under these conditions the heterogeneous nucleation is likely to dominate cloud formation leading to fewer and larger crystals.

By modelling different crystal morphologies, Zhang et al (1999) and Liou and Takano (1994) found that cirrus consisting of polycrystals had a less warming effect than cirrus made up of hexagonal columns, and an even lower warming effect than cirrus consisting of spherical particles. Mitchell et al (1996) found that different crystal habits can affect the radiative forcing by encouraging aggregation, which reduces the cloud optical depth and, consequently, the cloud albedo. A model was used, based on observations in cirrus, to determine the optical depth when aggregation occurred on crystals of different habits. Aggregation on planar polycrystals were shown to attenuate cloud optical depth by 10%; compact polycrystals by 23%; and hexagonal plates by 18%. Due to the abundance of planar polycrystals (side-planes, crossed plates) in the observations, during which many aggregates were also detected, Mitchell suggests that planar polycrystals are a precursor for aggregation due to their three-dimensional irregular shapes. In another study by Mitchell et al (1996b), the radiative properties of cirrus consisting of certain habits were modelled; hexagonal plates and columns showed similar reflectances, while planar polycrystals and bullet rosettes exhibited reflectances which were significantly higher.

Crystal habits, crystal size, growth processes, and nucleation modes are all important factors in shaping the radiative forcing of clouds. Due to limitations in measuring small ice crystals (previously mentioned in section 1.4.3), particularly those smaller than 50μm, there are still large uncertainties in cirrus microphysics and hence their net radiative forcing. Further research is required to identify

and quantify the occurrence of small ice particles in cirrus. As well as size, particle roughness can also have a significant effect on cloud forcing. Ulanowski et al (2006) made measurements of scattering patterns of laboratory grown ice analogue crystals and revealed that rough surfaces could reflect almost twice as much incident solar SW radiation as smooth surfaces. This highlights the importance of current and future research into ice particle roughness in cirrus.

1.5 Ice Particle Roughness

1.5.1 Definition of Roughness

When the surface of an ice crystal is illuminated by a laser beam, if each point on the illuminated surface of the particle acts a source of a secondary spherical wave (Huygens–Fresnel principle) then if the surface was rough enough the scattering pattern would consist of random variations in intensity. This consequence of the random path-lengths between the illuminated surface and the observation plane is an effect termed ‘speckle’, i.e. more roughness equates to more speckle. This can be seen in Figure 1.12; the amplitude at Q is the result of a set of vectors of random phase which when added together give a random resultant amplitude. Since this occurs at all other points surrounding Q, a speckled appearance is created. This is discussed in further detail in section 2.2.3.

In this project roughness is defined as both small-scale surface roughness, and large-scale complexity which produces a speckled two-dimensional scattering pattern when illuminated by light. This is a consequence of the two currently being indistinguishable by their scattering patterns. They do, however, have similar scattering properties, and will scatter incoming SW radiation similarly to each other, but differently to smooth particles.

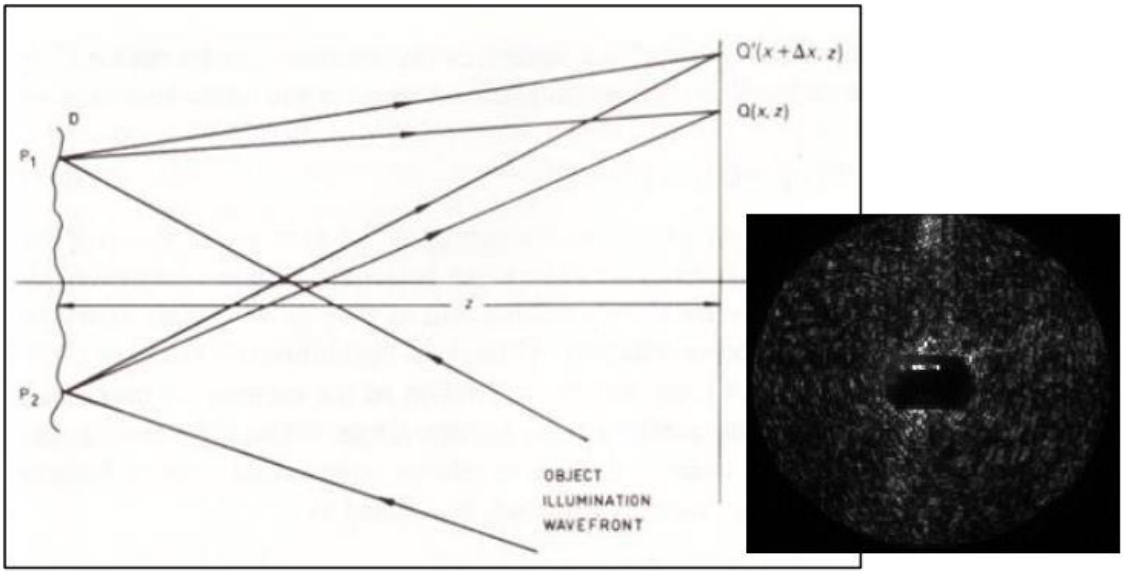

Figure 1.12: The scattering of light by a rough surface (Jones & Wykes, 1989). A rough surface (left) is illuminated by radiation. The scattered light reaches an image plane (right) where the resultant contributions of rays at each point are of random intensities due to the random path lengths between the plane and the rough surface. Shown in the lower right corner is a scattering pattern of a rough particle which exhibits a speckly appearance due to small-scale surface roughness and/or large-scale complexity.

Since rough particles scatter light differently to their smooth counterparts (Ulanowski et al (2006)) the value of the asymmetry parameter, *g*, can be affected by this morphological characteristic. The asymmetry parameter is estimated from the phase function which describes the angular distribution of the scattered light (Bohren & Huffman, 1998). The phase function is described by *p*, is a function of scattering angle, Θ, and has been normalized in equation 1.6;

$$\int_{4\pi} p \, d\Theta d\phi = 1 \qquad [1.6]$$

Under the assumption of a spherical particle the azimuthal dependence, ϕ, of *p* can be removed.

Whereas the phase function is described as a function of scattering angle, the asymmetry parameter takes a value between -1 and 1. It is described, in terms of phase function, in equation 1.7.

$$g = \int_{4\pi} p \cos\theta \, d\Theta \qquad [1.7]$$

Positive values correspond to the majority of the radiation being scattered in the forward direction (Θ<90°), and negative values correspond to back-scattering (Θ>90°). If all the scattering was in the forward direction then *g* would equal 1, if all the light was scattered backwards then *g* would equal -

1. Therefore the closer the asymmetry parameter is to -1, the higher the proportion of reflected light from the object.

1.5.2 Observations of roughness in ice cloud

Observations of cirrus clouds suggest that ice crystals stray from pristine habits which exhibit smooth surface features. Field et al (2003) found that phase functions which lack a pronounced 22° halo best fitted observations of ice crystals detected *in situ*. Garrett (2008) similarly found that measurements of cirrus produced phase functions which were inconsistent with idealized geometries. He noted a discrepancy between measured values of the asymmetry parameter, *g*, and calculated values, which he suggested could be a result of crystal complexity. Complexity provides more surfaces off which light will reflect and interfere constructively therefore enhancing backscatter (Videen, et al., 1998).

In an earlier study Garrett (2001) measured the asymmetry parameter of ice cloud in the Arctic and found it to be considerably lower than typical values used in climate models in which regular hexagonal crystals are assumed. The lower value of *g* was found to be consistent with model results in which crystal complexity, surface roughness and inclusions were taken into account. This enhanced backscatter was present during interaction with incoming SW radiation, but negligible with LW radiation, during model simulations of cirrus radiative properties where rough particles were assumed (Yi, et al., 2013). The simulations showed a globally averaged difference of 1-2 Wm^{-2}, which suggests that severely roughened ice particles could affect the net radiative forcing with the same magnitude as greenhouse gases (Figure 1.1).

The degree of roughness of ice particles in cirrus have been inferred from radiometer/polarimeter data from the PARASOL satellite by Cole et al., (2013). They estimated that the mean roughness corresponds to a degree between moderate and severe, with the highest number of roughened particles occurring in the tropics. It is suggested that the roughness observed here is due to formation in deep convective clouds which have been seen to contain many chain-like aggregates (Connolly, et al., 2005; Gayet, et al., 2012; Stith, et al., 2002). The presence of rough crystals was substantial in both midlatitude cirrus and polar cirrus; only 20-40% of crystals were classed as smooth in the midlatitude cirrus, and 45% of crystals were smooth in the polar cirrus. Rough ice particles were detected in Arctic cloud by Lampert et al (2009) using a CPI and Polar Nephelometer. A mixture of small spherical ice (<5μm) and deeply roughened hexagonal crystals provided the best fit to the phase function determined from the Nephelometer. The Polar Nephelometer and CPI were also used by Jourdan et al (2010) to probe mixed phase cloud in the Arctic. They found that when

the ice phase prevailed the scattering properties of the cloud were best described by either a mixture of droplets (35%) and roughened plates (65%) or by a mixture of droplets (15%) and roughened columns (85%). Deeply roughened crystals were detected over the Antarctic (Shcherbakov, et al., 2006). Shcherbakov and colleagues compared data from the Polar Nephelometer to results from a ray-tracing model to discover that the best fit was obtained when deeply rough crystals with a high proportion of internal inclusions were used.

Roughness was seen *in situ* from CPI images which showed plates with imperfect internal structures (Gayet, et al., 2011). The same cirrus cloud displayed featureless phase functions, whilst another cirrus case from the same campaign had pronounced 22° halo peaks and CPI images showed pristine plates. Gayet et al (2011) ran model simulations and found that the 22° halo was present when pristine crystals were assumed. Since the 22° peak was only observed 3% of the total time in-cloud, they concluded that imperfect and complex particles are more common than pristine particles in mid-latitude cirrus. Neshyba et al (2013) also found that the 22° halo peak is less likely to be exhibited by rough or complex crystals. In their SW scattering calculations they used hexagonal polyhedra with roughened surfaces, which were estimated to have asymmetry parameters up to 6% lower than their smooth counterparts, indicating that rough crystals will reflect more incoming SW radiation. Crystals which were severely roughened gave the best fit between model simulations and data from CALIOP (Cloud-Aerosol Lidar with Orthogonal Polarization) (Baum, et al., 2011), whereas assuming smooth particles led to large differences between the model results and observations indicating that roughened particles can be common in ice cloud.

Rough ice particles have been identified *in situ* based on their light scattering properties by Baumgardner et al (2005). The forward-to-backward light scattered ratios of ice particles in cirrus were measured using the Cloud and Aerosol Spectrometer (CAS), and were compared to model simulations. Of the observed ratios, 90% were in agreement with the model output when bullet rosettes, plates and hollow columns, all with rough surfaces, were assumed. Ulanowski et al (2014) also used forward scattering of light by ice particles to estimate the degree of roughness of ice in cirrus and mixed phase clouds. Several measures of pattern texture were used to calculate a value to represent the roughness of each crystal from two-dimensional scattering patterns. These values were then compared to those estimated from laboratory test particles in the same way. The ice crystals detected *in situ* had roughness values which corresponded to the rougher subset of test particles. This high degree of roughness was observed in sublimation zones and growth zones, both of which saw similar roughness. Other studies appear to have contradicting conclusions regarding changes in roughness between sublimation and growth regions. For example Kobayashi and Ohtake

(1974) found that the facets of crystals which had nucleated in air at temperatures between -26°C and -42°C became grooved during sublimation, but became smooth during re-growth. Pfalzgraff et al., (2010) observed similar behaviour on the facets of hexagonal ice crystals grown in a Scanning Electron Microscope (SEM): roughness in the form of trans-prismatic strands appeared 5-10µm apart during sublimation, but disappeared during re-growth resulting in smooth facets. Some studies, however, present evidence to the contrary by demonstrating that sublimation leads to smoother particles. Nelson (1998) found that ice crystals which sublimated in an isothermal chamber at subsaturations between 0.05% and 5% became completely rounded. Garrett (2001) inferred that sublimating crystals become rounded from Nephelometer measurements of Arctic cloud; the Nephelometer observed high asymmetry parameters which are associated with smooth and non-complex particles. Since these high values were detected in sublimation zones it follows that sublimation can lead to smooth and/or rounded crystals.

Particle roughness in cirrus is still poorly understood, in terms of the extent to which it occurs, and the mechanisms behind it. Since the rough and/or complex ice crystals can have a significant effect on the radiative properties of cirrus (Ulanowski, et al., 2006; Garrett, et al., 2001; Yi, et al., 2013; Neshyba, et al., 2013) it is of importance to quantify both the degree of roughness found *in situ* and the atmospheric conditions under which it occurs. The present thesis will do this by taking advantage of the ability of the Small Ice Detector 3 (SID-3) to record the 2-D scattering patterns of small ice crystals (1µm-150µm) *in situ*, from which particle size and roughness can be retrieved. The roughness values will then be compared to meteorological measurements taken simultaneously to determine the possible causes of different degrees of roughness.

1.6 Thesis Objectives

- From the 2D scattering patterns of ice particles captured *in situ* by SID-3, quantify the degrees of ice particle roughness observed during multiple ice cloud research flights.
- Execute and use laboratory measurements using ice analogues and SID-3 to refine pre-existing data-processing techniques and assess the reliability of existing data, i.e. whether particle characteristics can be accurately estimated from dark scattering pattern images.
- Investigate potential influences of meteorological conditions on particle roughness by:

1. Comparing instantaneous measurements of relative humidity, temperature, and estimated time since nucleation to the observed particle roughness values.
2. Comparing the degree of roughness observed in both supersaturated and subsaturated environments.
3. Investigating whether the general degree of particle roughness is affected by the particles undergoing multiple cycles between supersaturation and subsaturation.
4. Comparing the air-mass origin to the roughness of particles observed.

2 Instrumentation

2.1 Overview of Current Instrumentation for Ice Cloud Observation

Due to uncertainties in how high altitude cloud is represented in global climate models, the microphysics of ice clouds is an important and relevant area of research. Specialist instruments have been developed to measure individual properties of ice (size, roughness, and shape), and also bulk properties of ice cloud, such as the cloud optical depth and the mean asymmetry parameter. In this section the focus will be on existing and upcoming instruments which make measurements *in situ* only.

2.1.1 Particle Size

In situ measurements of single ice particles from which size information can be inferred have been made by multiple instruments. The instruments can make measurements using light scattering, impaction, or imaging techniques. Figure 2.1 gives measurement size ranges, and the measuring techniques of individual probes.

The 2-Dimensional Cloud (2D-C) probe, Cloud Imaging Probe (CIP), 2-Dimensional Stereo (2D-S) probe, and the Cloud Particle Imager (CPI), are all examples of instruments which provide images of single particles *in situ* from which size information can be retrieved. The 2D-C, 2D-S and CIP probes each contain an array of photodiodes which record the shadow of a particle as it passes through a laser beam (Brenguier, et al., 2013). This produces an image from which it is possible to identify the general shape and the size of the particle. The images taken using the CPI are more sophisticated than the other probes: two lasers are used for detection, and another laser is pulsed which triggers the recording of an image on a CCD camera. Since the CPI requires the laser to be pulsed, the images taken are discontinuous 'snap-shots' of the sequence of particles passing through the sample area, and therefore the relationship of neighbouring droplets and/or crystals is not necessarily recorded (Baumgardner, et al., 2011). The CIPs, 2D-S and 2D-C imaging probes provide a continuous recording as the photodiode array records information at a rate which is proportional to the sample velocity, resulting in multiple image slices which form an image of the entire particle. As a consequence the images are sensitive to the airspeed: if the sample rate is set too fast relative to sample speed then

the image will become elongated; if the sample rate is too slow then the image will become truncated (Brenguier, et al., 2013). This is not an issue with the CPI.

The imaging probes provide valuable particle measurements at diameters greater than 25µm, but they are susceptible to diffraction, depth of field and aberration issues which can result in poor quality images and unreliable morphology information at smaller diameters (Kaye, et al., 2008). As the size of a particle becomes more comparable to the wavelength of the illuminating light, diffraction effects are more substantial leading to blurry images in which facets are poorly defined. Similarly, depth of field issues are more likely to affect the images of small crystals since the depth of field is proportional to particle diameter. This can lead to a negative skew in size distributions (Brenguier, et al., 2013). The imaging probes do however have the advantage of being insensitive to particle composition whereas probes that use light-scattering techniques are affected by refractive index and orientation. The imaging probes have larger sample areas than the light-scattering probes and are therefore able to take measurements of particles with greater diameters.

The Cloud Droplet Probe (CDP), Forward Scattering Spectrometer Probe (FSSP), Cloud and Aerosol Spectrometer (CAS), Cloud and Aerosol Spectrometer with Depolarization (CAS-DPOL), and the Small Ice Detector (SID) range are all examples of cloud probes which use light scattering techniques to determine properties of single ice crystals. When a particle enters the path of the instrument laser, the scattered light is directed to a photodetector which converts the photons to an electrical signal. The intensity of the scattered light is proportional to the size of the particle. Light scattered in the near-forward direction is measured by each of the probes since most of the light scattered by a particle whose diameter is greater than the wavelength of the illuminating light is scattered in this direction. As a consequence of only collecting light scattered in the near-forward direction, the CDP and the FSSP cannot discriminate between spherical and non-spherical particles, i.e. spherical droplets and non-spherical ice. The CAS and CAS-DPOL both collect the scattered light over part of the back-scattered angles and the near-forward angles. The forward to backward scattering ratios estimated directly from the scattered light can be compared to the forward to backward ratios computed from the size distributions when the particles are assumed to be spherical to determine if there is a deviation from sphericity (Brenguier, et al., 2013). Asphericity can be detected by SID-2, although it does not collect back-scattered light, the azimuthally arranged photodiode elements, which cover the forward scattering angles 9-20°, allow spatially non-uniform scattering to be observed (Cotton, et al., 2010). SID-3 records images of the scattering pattern from which water droplets can be clearly identified as patterns with concentric circles, and differentiated from ice. If the scattering probe is unable to discriminate between spherical and non-spherical particles then

mis-sizing can occur: spherical particles tend to be assumed and therefore when calculating the diameter using the scattering cross sections aspherical particles tend to be undersized. Not only are particles assumed to be spherical, but they are also assigned the same refractive index, which can also result in miss-sizing. Furthermore the relationship between particle size and the scattering cross section, which describes relative intensity of scattered light within the solid angle, and is a function of particle size, shape, and refractive index, is nonlinear (Brenguier, et al., 2013). Therefore particles of different sizes can have the same scattering cross section. On average the estimated error in size is ±20% for these cases (DMT, 2009). This error can be avoided with SID-3 data because the method of size retrieval from the scattering patterns does not require assumptions of crystal habit or refractive index and the scattering cross section is not used for size retrieval.

Mis-sizing of particles by the scattering probes is also possible due to coincidence of particles in the laser path. If two particles enter the detection area at the same time they will be assumed to be one particle and will therefore be oversized. The occurrence of this is rare, particularly in ice cloud where particle concentrations are relatively low.

The greatest source of uncertainty when using light-scattering probes is in defining the sample area (Brenguier, et al., 2013). The instrument laser beam light intensity is not uniform, and the sample area is smaller for small particles which are likely to be measured in a limited fraction of the beam where the intensity is at maximum. It is also an issue at sizes approaching the upper size limit because the probability of particles crossing the beam edges increases. If most particles have diameters within the mid-region of the probes detection range then the uncertainty can be reduced to about 20% (Brenguier, et al., 2013).

Both the light-scattering probes and the imaging probes are susceptible to ice crystal shattering effects, which can result in misrepresentation of small particle concentrations (Korolev, et al., 2011). The arms and inlets of the probes present an obstruction to the airflow causing ice crystals to shatter into smaller crystals on impact. The shattered pieces can then enter the laser path of the instrument and will result in an unrealistic number of small ice crystals being observed. Korolev tips, which can be attached to an existing probe, have been created to mitigate this problem. They reduce the likelihood of shattered particles entering the laser path by effectively directing the pieces of a shattered crystal away from the detection area if it shatters on the probe arms. This is achieved by arranging the surfaces of the tips which are closest to the sample area so that they are parallel to the airflow; and the opposite surface so that it is tilted with respect to the airflow. This causes the

shattered particles to be deflected away from the sample area. Korolev tips are currently available for most cloud probes. Another way in which the probability of measuring shattered ice has been reduced is by creating probes with open paths so that the number of large particles shattering on the probe housing is reduced (Ulanowski, et al., 2014).

Two probes that use impaction techniques, the Video Ice Particle Sampler (VIPS) and the Cloudscope, record the images of particles which have impacted on an exposed surface. They have the advantage of possessing much larger sample areas than the scattering probes, and the imaging probes if the particles are smaller than 50µm (Baumgardner, et al., 2011). They also have better resolution and so provide a more accurate method of habit identification. Although they can provide better resolved images of small particles than the imaging probes, their lower boundary is around 10µm, which is greater than that of some of the light-scattering probes, SID-2 and SID-3 for example can measure down to a 2µm and 1µm, respectively. The VIPS instrument collects particles *in situ* on a film 8mm wide which has been coated with silicone oil. Images are then taken of the particles with video microscopes at two magnifications. The Cloudscope collects particles on a sapphire window and images them using an optical microscope with a CCD video camera. The particle size, shape, and concentrations can be derived from the images. The sapphire window is heated so that the ice crystals will sublimate and the rate of sublimation is used to determine their mass. The instruments carry uncertainties, however, due to the collection efficiency as a function of size and shape. They both have inlets to measure the airflow, and since the trajectory of particles along streamlines is dependent on particle mass, area, and shape, size sorting can occur. This leads to distorted PSDs, most often a broadening effect (Baumgardner, et al., 2011). Both of these impaction probes were created at research institutes and are not commercially available.

An emerging method for the measurement of particles *in situ* is in-line holography. A hologram, which is an interference pattern caused by the superposition of an incident plane wave and the light scattered by the illuminated particles, provides the three-dimensional position of particles in a sample volume from which size information can be derived. The HOLOgraphic DEtector for Clouds (HOLODEC), developed at Michigan Technological University, is a cloud probe which uses this method. It has the advantage over other probes of being able to sample relatively large volumes of cloud instantaneously and in sequence. This large volume means that multiple ice crystals and/or water droplets can be imaged at the same time and their relative spatial locations can be determined. This makes it a useful technique for studying particle clustering and crystal shattering. HOLODEC is able to image a wide range of particle sizes, from 15µm up to 2000µm (Baumgardner, et

al., 2011).This lower size limit is at least 13µm greater than the lower limits of the before mentioned scattering probes, however, HALOHolo, a more recently developed probe, is able to use holography to image particles down to a few microns in diameter. HALOHolo was created at the University of Mainz and is similar to HOLODEC in function. The instrument has been flown on multiple campaigns, but published results are not currently available.

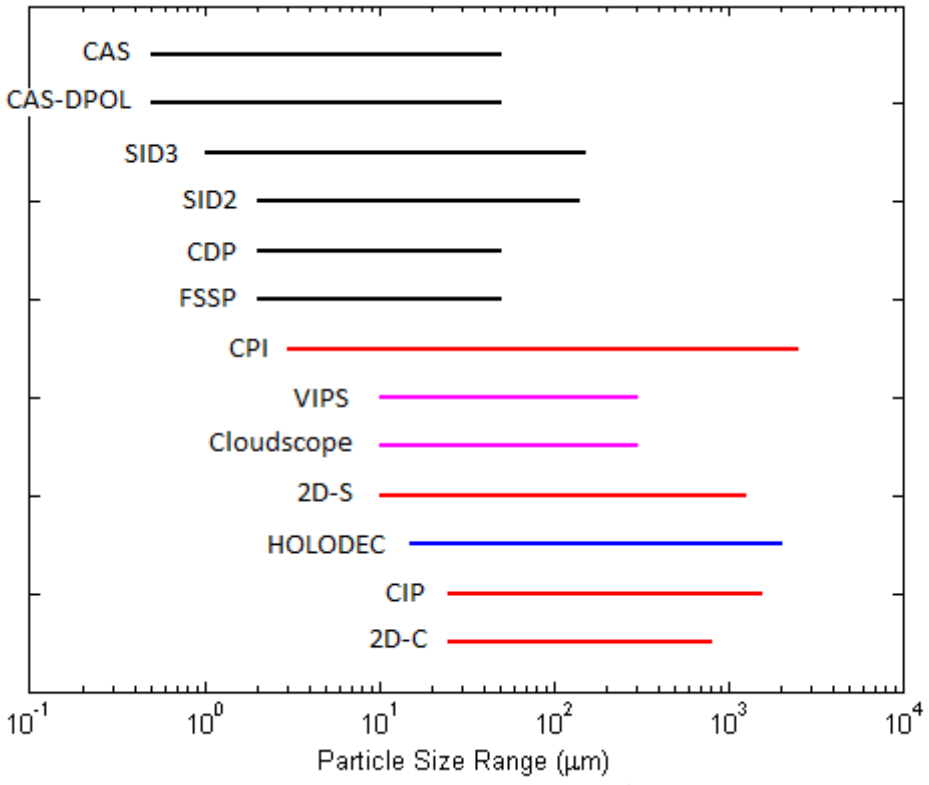

Figure 2.1: Particle measurement size ranges for different cloud probes. The black lines reperesent scattering probes; red lines are imaging probes; magenta lines are impaction probes; and the blue line is a probe which uses holographic techniques to probe clouds. The CAS, CAS-DPOL, CDP, and CIP were all made by Droplet Measurement Technologies (DMT); the SID-2 and SID-3 were created at the University of Hertfordshire; the FSSP and 2D-C were made by Particle Measuring Systems (PMS); the CPI and 2D-S were created Stratton Park Engineering Company; the VIPS was created at the National Centre for Atmospheric Research (NCAR); the Cloudscope was created by the Desert Research Institue (DRI); and HOLODEC was developed at Michigan Technological University.

2.1.2 Particle Roughness

Particle roughness can be inferred from measurements taken of individual ice crystals and from bulk properties of ice cloud. The latter can be measured *in situ* by nephelometers, which determine the scattering phase function of clouds. The Polar Nephelometer (PN) and the Cloud Integrating Nephelometer (CIN) both measure the scattering by ice crystals in the forward and backward directions, and so the asymmetry parameter can be determined. Since rough and/or complex particles exhibit lower value asymmetry parameters (Ulanowski, et al., 2006), i.e. they reflect more incoming SW radiation, the degree of roughness/complexity of an ice cloud can be estimated. The PN and CIN are able to measure the scattering of both ice and water with diameters from 5µm to 500µm, and 4µm to 2500µm, respectively (Brenguier, et al., 2013). Furthermore they are able to discriminate between ice and water based on the shape of the scattering phase function. When droplets and/or ice crystals pass through the laser beam path of the PN the light is scattered and reflected off a paraboloidal mirror onto a circular array of 41 photodiodes. As a consequence of holes which have been drilled into the mirror, light can be diffracted by the edges of the holes and cause contamination in the near forward (<15°) and the near backward (>162°) directions rendering them unreliable (Brenguier, et al., 2013). The CIN does not use a mirror; when particles pass through its laser beam path the scattered light is collected by a set of four Lambertian sensors, sensors whose response is unaffected by the direction from which the incident light is travelling. The signals received by this sensor are then used to infer the light-scattering properties of the clouds. To compute the asymmetry parameter the light-scattered between the angles 0° and 180° is required. Since the near-forward and near-backward scattering measurements are either not captured or are not reliable, these must be inferred from theory, which may result in inaccuracies. The uncertainty in the calculation of the asymmetry parameter for both nephelometers is ±0.01 (Baumgardner, et al., 2011). The Nephelometers have an advantage over single-particle probes in that particle coincidence, discussed in section 2.1.1, is not an issue.

The CPI can be used to determine particle size, and has therefore been introduced in the previous section, but it is also possible to observe the complexity of the ice crystals from the images. Details such as riming and aggregation, which make a particle more complex, can be seen provided that the crystals are large enough. It is difficult to determine particle properties that have diameters less than 50µm. This is due to diffraction, depth of field and aberration issues which lead to poorly resolved images as particle size becomes more comparable to the wavelength of the illuminating light (Kaye, et al., 2008).

The Cloud and Aerosol Spectrometer (CAS), mentioned in the previous section, is also a single-particle probe which can be used to estimate the degree of roughness and complexity in ice cloud. The light scattered in the near forward and near backward direction by particles which intercept the laser beam is measured by two detectors. A ratio of forward to backward scattered light can then be calculated and compared to model simulations to estimate how rough and/or complex the observed ice crystals are (Baumgardner, et al., 2005). This is a more indirect approach since the ratios derived from the CAS data do not necessarily provide roughness values on their own, however, they may provide a fair indication should general forward to backward scattered ratios from model simulations be categorized in terms of roughness and complexity.

The Small Ice Detector 3 (SID-3) has the advantage of providing direct roughness values of *in situ* particles relative to each other. The SID-3 probe images the forward-scattering patterns resulting from particles passing through a laser beam. The images allow for the retrieval of roughness/complexity based on the idea that a more random image, with regards to bright spots and dark spots due to constructive and destructive interference, equates to a more rough/complex particle, as explained in the following section. The roughness values may also be compared to scattering patterns from a mixture of ice analogues, particles with the same refractive index as ice but that are stable at room temperature, in order to provide a visual representation of the relevant degree of roughness/complexity measured *in situ*. The SID-3 probe can measure particles from 1µm up to around 150µm, and since it is a scattering probe as opposed to an imaging probe, inaccuracies do not arise at the smaller diameters due to optical effects such as diffraction and aberration. The probe is susceptible to particle coincidence, although this is almost negligible in ice clouds due to the low particle concentrations. SID-3 is described in further detail in the following section.

2.2 The Small Ice Detector 3

2.2.1 Introduction

The Small Ice Detector 3 (SID-3) is the third in the line of a range of cloud probes specifically designed to measure and size small ice crystals *in situ*. It is able to measure particles as small as 1µm using light-scattering techniques (Kaye, et al., 2008). Since light-scattering probes are not susceptible to optical issues such as diffraction, depth of field and aberration they can be more reliable than imaging probes at studying particles smaller than around 25µm. The microphysics of small ice

crystals requires further investigation since they can have a large effect on cloud radiative properties and frequency (Zhang, et al., 1999; Mitchell, et al., 2008; Jakob, 2002), the former of which still remains a poorly represented parameter in climate models. In addition to particle size, particle roughness and complexity can also have a significant effect on cloud radiative properties with rougher particles reflecting twice as much incoming solar SW radiation than smooth particles (Ulanowski, et al., 2006). SID-3 is unique in that the degree of particle roughness can be inferred from the measurements. Similarly to other scattering probes, SID-3 estimates individual particle size from the intensity of the light scattered as the particle passes through a laser beam, however, images of the scattered-light are also taken. The two-dimensional scattering patterns allow an alternate way of retrieving particle size, in addition to the particle roughness and/or complexity.

2.2.2 Instrument Setup

SID-3 was designed so that it is suitable for both laboratory and *in situ* use; it can be attached to a pylon under the wing of an aircraft in a standard instrument canister, as seen in Figure 2.2. The probe has flown on five campaigns four of which were based in Prestwick, Scotland, and one in Cape Verde. The data presented in this thesis are from two of the campaigns: PIK&MIX (a mixture of Met Office research flights in January/February 2012), and CIRCCREX (CIRrus Cloud Coupled Radiation Experiment in March 2015).

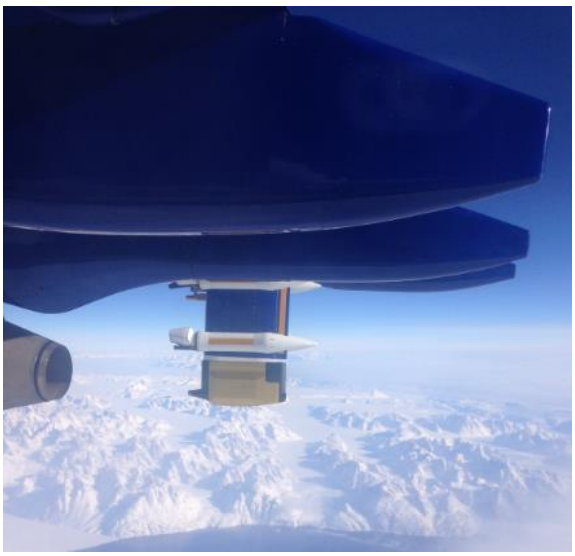

Figure 2.2: SID3 and SID2 probe collecting data over Greenland whilst attached to the wing of the FAAM aircraft. Both probes are placed in white canisters with a strip of yellow reflective tape; the gold and black probe below the SIDs is the 3V-CPI, a single-particle imager.

The instrument is able to measure particles with diameters from 1µm up to 150µm. It has a smaller sample volume, from which scattered light is detected, than its predecessor in order to reduce the possibility of particle coincidence, i.e. the chance of multiple particles being measured at the same time. When a particle enters the path of the 532nm wavelength laser the scattered light must be detected in two areas within the laser beam by two photomultiplier tubes (PMT) before data is collected. The smaller area, probed by the "small volume PMT", is within the larger area, which is probed by the "large volume PMT". When both PMTs have detected a particle the scattered light is directed to a PMT which converts the light into electrical signals from which the size can be estimated. Like many scattering-probes, spherical particles/droplets are assumed when size is calculated from the intensity of the scattered light, which can result in mis-sizing of any non-spherical particles. Size retrieval from the two-dimensional scattering patterns does not require assumptions to be made regarding particle shape. The 2-D scattering patterns are created when the larger portion of the split light is directed onto an intensified charge-coupled device (ICCD). This is triggered when the smaller portion enters the PMT (Kaye, et al., 2008). A schematic of the detection area and the optical components can be seen in Figure 2.3. The camera is able to image up to 30 scattering patterns per second, meaning that not all particles which are detected will be imaged unless the particle concentrations are low. The PMT does record the intensity of light scattered by every particle that enters the sample area, and therefore may be used as a supplement to the scattering patterns in order to calculate more representative particle concentrations.

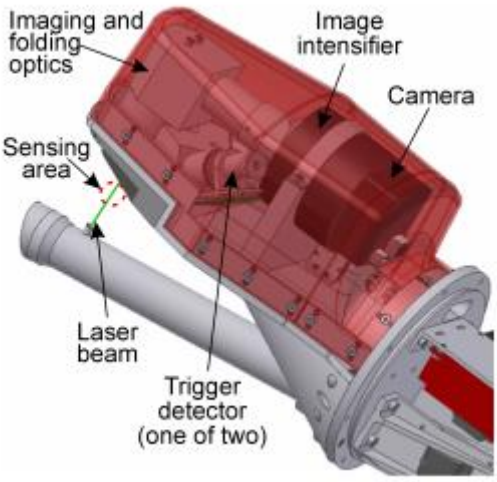

Figure 2.3: A schematic of the sensing area and optical components of the Small Ice Detector 3 (SID-3) probe (Ulanowski, et al., 2014).

SID-3 measures the light scattered by particles over the angles 6° to 25°, which is sufficient to include the 22° halo scattering (Ulanowski, et al., 2014). The peak intensity of light scattered at an angle of 22° is of interest since it is indicative of smooth, pristine ice crystals; a dampening or

disappearance of this peak suggests the ice particles are rough and/or complex (Ulanowski, et al., 2006; Ulanowski, et al., 2014; Yang, et al., 2013). The degree of roughness can also be estimated from the 2-D scattering patterns; whereas the patterns of smooth surfaces have well-defined bright arcs and spots, those of rough particles have a much more random and 'speckly' appearance.

2.2.3 Data Processing

2.2.3.1 Roughness Retrieval

If a particle has rough surfaces or is particularly complex then the image of its scattering pattern in the near-forward direction will reveal spots of varying intensity that can be randomly distributed. The light can be considered to be absorbed and then re-emitted by each point on the particle, and the amplitude of the scattered light at any point is the sum of the contributions from each point on the surface. The phase difference of the contributions is dependent on their path difference, Equation 2.1. If the surface of the particle is optically rough, i.e. the height variation is of the order or greater than the wavelength, λ, of the illuminating light, then since the surface height is randomly varied by multiples of λ, the phase will also randomly vary by multiples of λ. The sum of the set of vectors with random phase will give rise to random resultant amplitude, Figure 2.4. Therefore the resulting scattering pattern will be an image consisting of spots of varying brightness with random spatial distributions. Figure 2.5 shows examples of 2-D scattering patterns of a smooth non-complex particle, a rough particle, a complex particle, and an aggregate. The more pronounced the speckle is, the rougher or more complex the particle is. Therefore the degree of roughness and/or complexity occurring in ice clouds can be estimated directly from images of the 2-D scattering patterns of particles detected *in situ* by the SID-3 probe.

$$\Delta\phi = \frac{2\pi\,\Delta x}{\lambda} \qquad [2.1]$$

Where Δϕ is the phase difference (in radians),Δx is the path difference, and λ is the wavelength of the incident light.

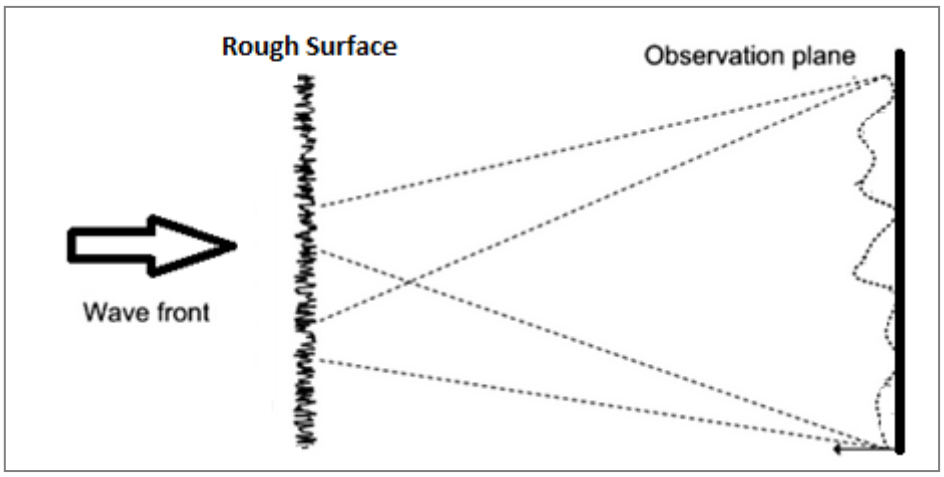

Figure 2.4: Forward scattering by an object with a rough surface. The contribution from each scattered ray will be random due to the variations in the object surface height resulting in random path lengths between the surface and the observation plane. Therefore the 2-D scattering pattern will be spots of differing intensity distributed randomly.

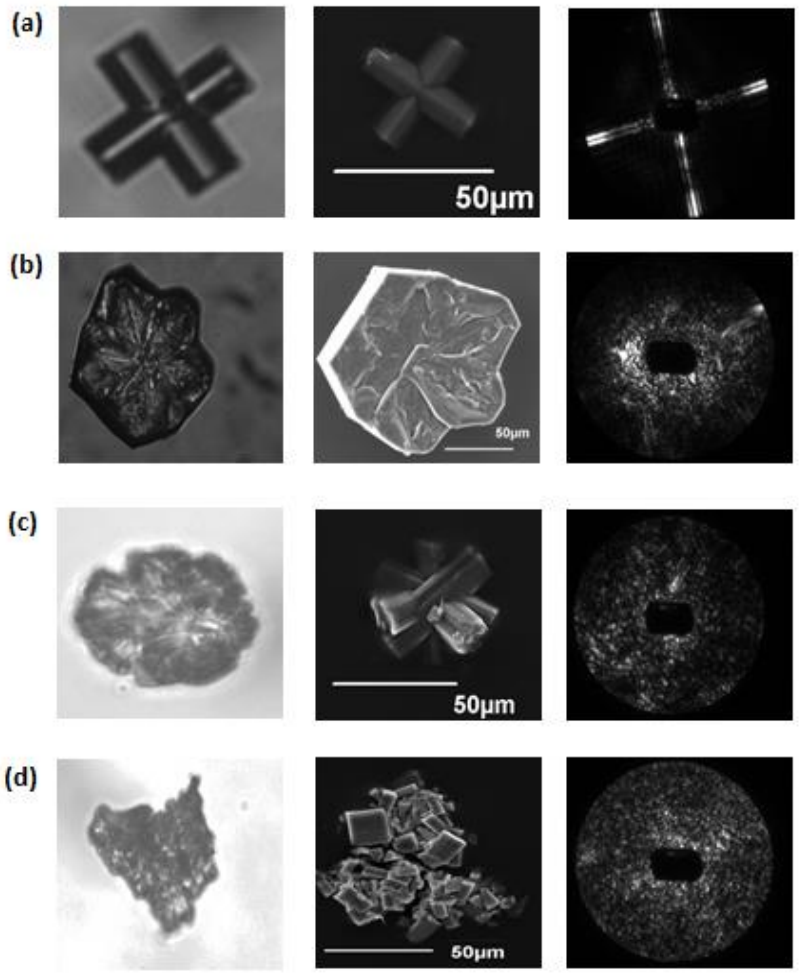

Figure 2.5: Columns left to right; image of the ice analogue under an optical microscope; image in a scanning electron microscope (SEM); image of the two-dimensional scattering pattern recorded by SID-3 when the particle was placed in the path of the laser. The scattering pattern of a particle with smooth facets and low complexity (a) exhibits bright arcs; the scattering patterns are speckly for particles with rough surfaces (b), complex shapes (c) and very complex structures due to the aggregation of multiple particles (d). NB, the orientation of the particles in both microscope images do not necessarily correspond to the orientation of the particle when it entered the path of the laser beam.

Speckle techniques have been used for many years in industry to improve the performance of engineering components, systems, and materials in a wide range of areas. For example they can provide a non-destructive way of determining faults in components by locating surface displacements when small loads are applied. The SID-3 probe is the first to provide scattering patterns of individual particles for which speckle techniques have been employed to retrieve atmospheric ice-particle properties (Ulanowski, et al., 2014).

The roughness of a particle can be retrieved from the 2-D scattering patterns using image texture analysis and by considering the brightness distribution over the image. When something is rough to touch there are differences between low and high points; image texture works in a similar way,

except the highs and lows are brightness values (also called grey levels) instead of elevation changes. The Grey-Level Co-occurrence Matrix (GLCM) can be used to assess the variations in brightness by comparing neighbouring pixels. Each pixel in the 2-D scattering pattern is assigned a number based on its grey-level, as in Figure 2.6. In the example shown in Figure 2.6 there are three different levels of brightness shown in the image; these levels are assigned values from 0 to 2 with 0 representing the darkest shade, and 2 representing the brightest shade, as illustrated by the number array below the image.

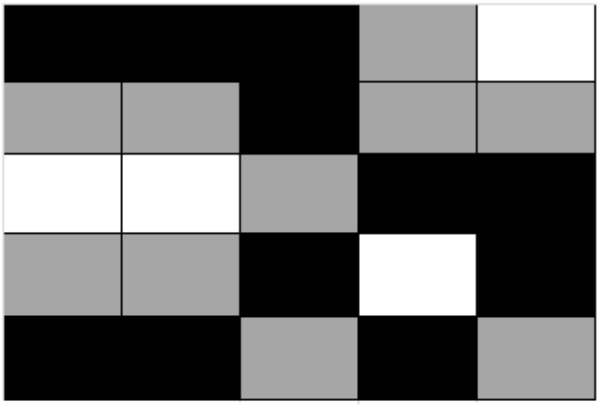

0	0	0	1	2
1	1	0	1	1
2	2	1	0	0
1	1	0	2	0
0	0	1	0	1

Figure 2.6: An array of 'pixels' with three different brightness levels (white, grey, and black). The numbers below correspond to the level of brightness, otherwise known as the grey-level; a white pixel will have a value of 2, a grey pixel of 1, and a black pixel of 0.

A matrix is created based on the similarity in brightness of neighbouring pixels. Each pixel will be compared to that on its right hand side and its left hand side. The occurrence of each different combination of two neighbouring pixels are tallied, i.e. the number of times a pixel with brightness level 0 neighbours a pixel with brightness level 0 will be added up and used to create the value in row 1 column 1 of the GLCM. Using the pixels and corresponding brightness levels shown in Figure 2.6 the number that would be placed in row 1 column 1 of the GLCM would be:

The total number of 0 values to the left of a 0 value + the total number of 0 values to the right of a 0 value = 4 + 4 = 8.

This is repeated for all possible combinations of neighbouring pixels (to the left and right). The resulting matrix will be an n x n matrix where n is the number of brightness levels. A 3x3 matrix will result from the pixels shown in Figure 2.6 because there are three different brightness levels; 0, 1, and 2.

The counts in the matrix are then replaced by the probability of each combination occurring. This is achieved simply by dividing the number of times a pixel combination occurs by the total number of counts for all combinations. The resulting GLCM matrix is shown in Figure 2.7.

$$\frac{1}{40}\begin{pmatrix} 8 & 8 & 2 \\ 8 & 6 & 2 \\ 2 & 2 & 2 \end{pmatrix}$$

Figure 2.7: The grey-level co-occurrence matrix corresponding to the pixel array in Figure 2.6, where the east and west matrices are added and the values are given in terms of probability.

The probabilities can then be used to determine energy, also referred to as the uniformity, using equation 2.2. High values of energy (uniformity) occur when there is more similarity in grey-level between pixels. The energy measure has previously been seen to provide the most representative values when correlated against subjective roughness of test particles than any other property derived using the GLCM (Ulanowski, et al., 2012).

$$Energy = \sqrt{\sum_{i,j=0}^{N-1} P_{i,j}^2} \qquad [2.2]$$

Where P is the probability; N is the number of grey levels; i is the row number of the GLCM; and j is the column number of the GLCM.

Calculation of the co-occurrence matrix is not limited to 3 grey-level values and two directions in which pixels are compared, as used in the above example. The more directions and grey-levels that are included in analysis, however, the larger the matrices, the more computing power is required. The 2-D scattering patterns from SID-3 are 12-bit TIFFs stored in 16-bit files and so the number of grey-level values is set to 16. TIFF images are favoured over 8-bit jpegs to prevent any loss of information that would occur if the images were compressed. This does, however, mean that the

processing can take hours to complete if it is run on a regular 64-bit operating system, when the dataset consists of thousands of images, which is common during research flights in ice cloud.

The energy value from the image texture analysis is used in conjunction with three statistical measures of the overall image brightness distribution to calculate a roughness value from each scattering pattern. The most robust combination occurs when the energy is combined with the kurtosis, and the root-mean-square over the standard deviation of the overall brightness (Ulanowski, et al., 2012). If a distribution x descirbes the brightness of individual pixels in an image, and there are N pixels in total then the mean, root-mean-square, standard deviation and kurtosis of the distribution can then be estimated using equations 2.3, 2.4, 2.5, and 2.6, respectively. For consistency the equations presented have been derived from Matlab functions since the code to retrieve particle properties from the scattering patterns was written in Matlab.

$$\mu = \frac{1}{N}\sum_{i=1}^{N} x_i \qquad [2.3]$$

$$RMS = \sqrt{\frac{1}{N}\sum_{i=1}^{N} x_i^2} \qquad [2.4]$$

$$\sigma = \sqrt{\frac{1}{N}\sum_{i=1}^{N} |x_i - \mu|^2} \qquad [2.5]$$

$$\kappa = \frac{\frac{1}{N}\sum_{i=1}^{N}(x_i-\mu)^4}{\left(\frac{1}{N}\sum_{i=1}^{N}(x_i-\mu)^2\right)^2} \qquad [2.6]$$

The kurtosis is a measure of uniformity across the entire image. If the brightness distribution over the image is normal, or has a well-defined peak with long tails, then the kurtosis will take a high value. If the distribution is uniform then the kurtosis will be low. When the mean intensity over the entire image is high a bright image is expected. A high-contrast image is implied when a high standard deviation is estimated. The kurtosis, mean, and standard deviation were combined with the energy calculated from the GLCM to create a roughness measure, equation 2.7. The combined

roughness was defined by Ulanowski (2012; 2014) based on how the statistical measures best compared to the subjective roughness of a range of particles which were observed in detail in a SEM. The terms have been weighted such that each contributes to the combined roughness equally, and so that the output lies between 0 and 1.

$$Combined\ Roughness = 0.9 - energy(GLCM) - \frac{\log(kurtosis)}{5} + \frac{RMS/SD}{5000} \quad [2.7]$$

2.2.3.2 Size Retrieval

The size of a particle can be estimated from the image of its scattering pattern by calculating the size of the speckle spots. It has previously been shown that increasing particle size causes the number of speckle spots within a defined area to increase therefore reducing the average area of individual spots, such that particle diameter is inversely proportional to spot size (Holler, et al., 1998; Holler, et al., 2004; Ulanowski, et al., 2012b). The latter study included a comparison of speckle spot size, calculated directly from 2-D scattering patterns imaged by SID-3, and particle diameter. A mixture of particles were used including mineral dust, pollen and ice analogues whose circle equivalent diameters were estimated from microscope images, and plotted against the inverse median area of the speckle spots. A least squares fit was used to determine the relationship between median speckle area, A_s, and the particle diameter, D, equation 2.8.

$$D = {5.3 \times 10^3}/{A_s} \quad [2.8]$$

The area of the speckle spots are calculated from binary versions of the scattering patterns, and the spots are located by finding regional maxima, i.e. groups of pixels with the same intensity value, where the boundaries are located at the point where neighbouring pixels all have lower intensity values. Locating the speckle spots also enables the removal of those which are close to or at the image edge and may have been truncated. The median area has been chosen over the mean in order to reduce the influence of outliers due to misidentification of spots, which may occur as a consequence of pixel saturation, dark images, or the merging of adjoining spots.

Two particles of different diameters are shown in Figure 2.8 alongside their scattering patterns which were imaged by SID-3. The scattering pattern created by the interaction of the laser beam with the smaller particle exhibits speckle spots which are generally larger than those seen in the

scattering pattern created by the larger particle, i.e. the size of the speckle spots are inversely proportional to the diameter of the particle. The particles are examples of ice analogues that were created at the University of Hertfordshire.

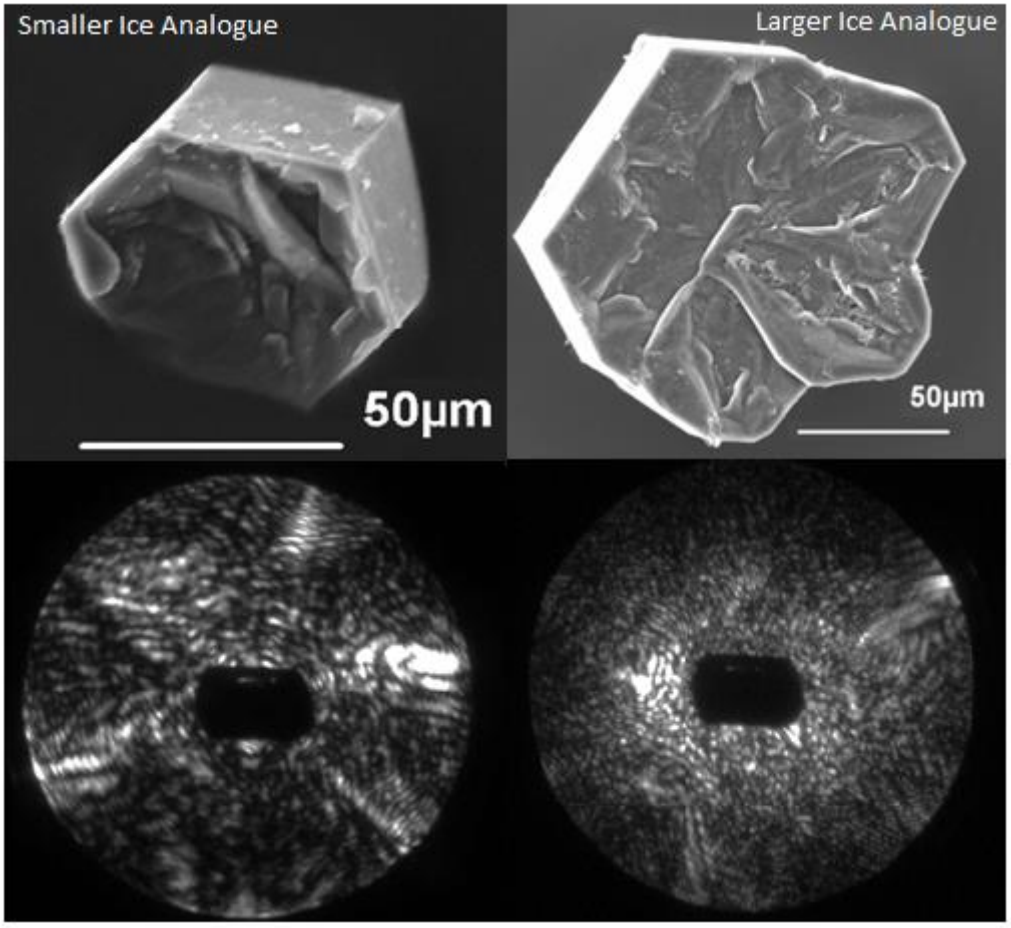

Figure 2.8: Ice analogues imaged in a SEM and their corresponding 2-D scattering patterns recorded by SID-3. The circle equivalent diameters were calculated using the binary form of the particle image when under an optical microscope, and from the scattering patterns by using the median speckle spot size. The smaller particle had a diameter of 69.2µm from the optical microscope image, and 68.4µm from the scattering pattern. The larger particle had a diameter of 107.8µm from the optical microscope image, and 117.8µm from the scattering pattern.

2.2.4 Ice Analogues

Ice analogues were created at the University of Hertfordshire to act as a surrogate for both simple and complex ice crystals in scattering experiments. Sodium hexafluorosilicate, Na_2SiF_6, was chosen due its refractive index which is very similar to that of ice, and that it remains stable at room temperature. Analogues in a range of morphologies were created: hexagonal columns, plates,

rosettes, aggregates, and irregular habits are available in sizes from less than 1µm up to hundreds of microns, examples can be seen in Figure 2.9. The analogues have been used to test the validity of retrieving both size and roughness values from 2-D scattering patterns (Ulanowski, et al., 2012b; Ulanowski, et al., 2012). The roughness values determined from the scattering patterns of the ice analogues whose images have been taken under the optical microscope and in the SEM are used to contextualise the roughness observed *in situ*.

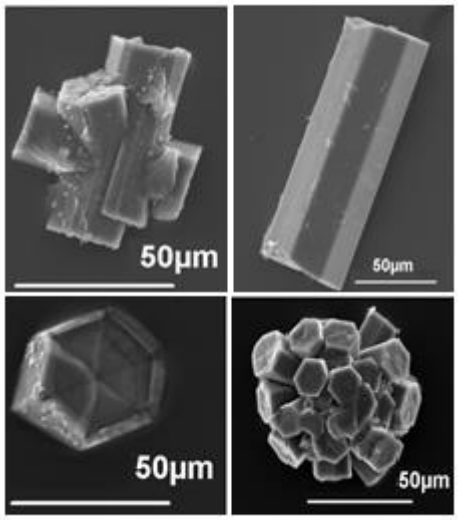

Figure 2.9: A selection of ice analogues of different habits that have been imaged in a SEM.

2.2.5 Calculating Particle Size Distributions

In-cloud particle size distributions (PSDs) can be calculated using the size information retrieved from the 2D scattering patterns recorded *in situ*. The PSDs describe the particle concentrations at specific diameters, 1µm to 150µm for particles detected by SID-3, for defined time periods.

The circle equivalent diameters of ice crystals are estimated from the 2D scattering patterns using the method set out in the previous section, 2.2.3.2. The time at which each particle was measured is also retrieved from the images. The particle concentrations at each diameter are first calculated for each second of data; they may later be averaged over longer periods. Prior to the concentration calculation, the particles are binned according to their estimated diameters; the fifteen size bins range from 0µm to 150µm in steps of 10µm. The number of particles that are assigned to a size bin are summed to give the count frequency in that bin per second. The count frequencies are determined for each size bin, each second. The particle number concentrations can then be

calculated using the count frequencies, f, the airspeed, v, the surface area of the triggering zone, A, and the time interval, t, as in equation 2.9. Imaging probes will have dead time which can occur between consecutive camera triggering whilst the previous image is being digitised and stored, which can result in a loss of information since data is not constantly being recorded. The dead time can be subtracted from the total time to give the time during which measurements were actually being made for use in further analysis, i.e. the time interval in the PSD calculation. The airspeed comes from the FAAM CORE turbulence probe, and the surface are of the triggering zone had previously been measured as A=0.88mm^2, and is assumed to be constant.

$$N = \frac{f}{Avt} \quad [2.9]$$

Where N is the number concentration, f is the number of counts, A is the sampling area, v is the airspeed, and t is the time interval.

2.3 Relative Humidity Calculation

The Water Vapor Sensing Systems Version 2 (WVSS2) has been used to estimate the relative humidity with respect to ice throughout this thesis. The WVSS2 was designed as an aviation product to provide information on atmospheric water vapour. There are two versions which are generally flown simultaneously on the FAAM BAe 146 research aircraft; they differ in terms of their inlets through which air samples are received. The flush inlet (WVSS-2F) is within the aircraft's boundary layer, whereas the Rosemount inlet (WVSS-2R) is mounted 12cm from the aircraft and is believed to lie outside of the aircraft boundary layer (Vance, et al., 2014; Vance, et al., 2011). The inlets of both instruments have been positioned such that they are angled down to match local airflow, and so that they are at a sufficient distance from the cabin doors to minimise the possibility of sampling air which has leaked from the cabin. Both versions of the WVSS-2 use a laser which has a wavelength corresponding to the absorption wavelength of water, to sample incoming air. The absorption of the light is therefore proportional to the amount of water in the air, and the mixing ratio of water vapor is estimated. If the true air temperature, T, and atmospheric pressure, p, are known then the volume mixing ratio, vmr, can be used to calculate the relative humidity with respect to water, RH_{liq}, and with respect to ice, RH_{ice} using equations 2.10 to 2.14 (Murphy & Koop, 2005; Cactus, 2015).

$$p_{ice} = \exp(9.550426 - \frac{5723.265}{T} + 3.53068\ln(T) - 0.00728332T) \quad [2.10]$$

$$\ln(p_{liq}) \approx 54.842763 - \frac{6763.22}{T} - 4.210\ln(T) + 0.000367T + \tanh\{0.0415(T - 218.8)\}(53.878 - \frac{1331.22}{T} - 9.44523\ln(T) + 0.014025T) \quad [2.11]$$

$$p_w = vmr.p \quad [2.12]$$

$$RH_{liq} = \frac{p_w}{p_{liq}} \quad [2.13]$$

$$RH_{ice} = \frac{p_w}{p_{ice}} \quad [2.14]$$

Where p_{ice}, p_{liq} are the equilibrium vapor pressures of ice, and liquid water, respectively; p_w is the partial pressure of water.

The WVSS-2F is faster to respond to changes in humidity, and measures reliably in liquid cloud, but tends to over-read in dry conditions. The WVSS-2R is slower to respond to humidity changes and does not perform as well in liquid cloud due to the evaporation of some liquid cloud droplets in the probe; however, it provides more accurate readings in ice cloud than the WVSS-2F (Vance, et al., 2011; Vance, et al., 2014).

3 Laboratory Experiments to Refine Processing Techniques

The reliability of particle property retrieval when using existing software developed by Ulanowski (2012b) and described in section 2.2.3 was tested. The results were then used to refine the processing such that images with characteristics that were found to produce inaccuracies in size and roughness estimation were rejected. The image issues investigated were:

1. The maximum number of saturated pixels allowed before images were unrepresentative of the corresponding particle (section 3.2).
2. The amount of speckle required for accurate size estimation (3.3).
3. The minimum mean brightness required over the entire image for accurate particle property retrieval (3.4).
4. Whether images recorded under different camera settings could be reliably compared (3.5).

As mentioned the laboratory work was used to refine the processing method; it was also used to address the origin of some of the image issues specifically the presence of dark images which are discussed in the image brightness section (3.4).

The general setup is described in section 3.1 with accompanying figures 3.1 and 3.2. Addressing different image issues introduced subtle differences in the setup which are mentioned in the corresponding sections.

3.1 Laboratory Method

Ice analogues in a range of sizes and habits were chosen and imaged under an optical microscope. Binary versions of the images were created, in which the particle was represented by black pixels, and the background by white. The sum of the number of pixels contained within the black area was calculated and converted into microns; the number of microns represented by each pixel was given in the microscope manufacturer's specifications. The circle equivalent diameter of the particle was then determined by assuming a circle and relating the area of the circle to its diameter. The images were taken after the chosen ice analogues were moved onto an anti-reflection glass window, such that the projected area was known when the particles were later measured by SID-3.

The glass windows have a MgF_2 coating which reduces reflection to less than 0.5%. This low reflectance makes them a good choice for these scattering experiments since they can support the particle in the path of the laser beam without influencing the intensity and/or direction of the scattered light. The anti-reflection windows can be seen in Figure 3.1 next to a metal holder; the

glass windows slot into the hole of the metal holder which can be seen in the top right of the image. The metal holder is then attached to a clamp which can be moved in the x, y, and z plane at distances of the order of a micron at a time. This means that multiple ice analogues could be lined up on the same window simultaneously and the window could be moved so that each analogue is in the path of the beam separately and consecutively. The windows themselves are 10mm in diameter and 2mm thick. Generally around 20 ice analogues with diameters ranging from a few microns to 150µm would be placed on the window during an experiment; an example of some ice analogues lined up on a window can be seen in Figure 3.2. Columns were used as markers by being placed, in known orientations, between particles which were irregular, complex, or possibly rough, to help identify the ice analogue from its 2D scattering pattern: scattering patterns of smooth columns are easily identified as bright arcs, whereas rough and complex particles produce random and speckly scattering patterns which are often difficult to classify with regards to habit.

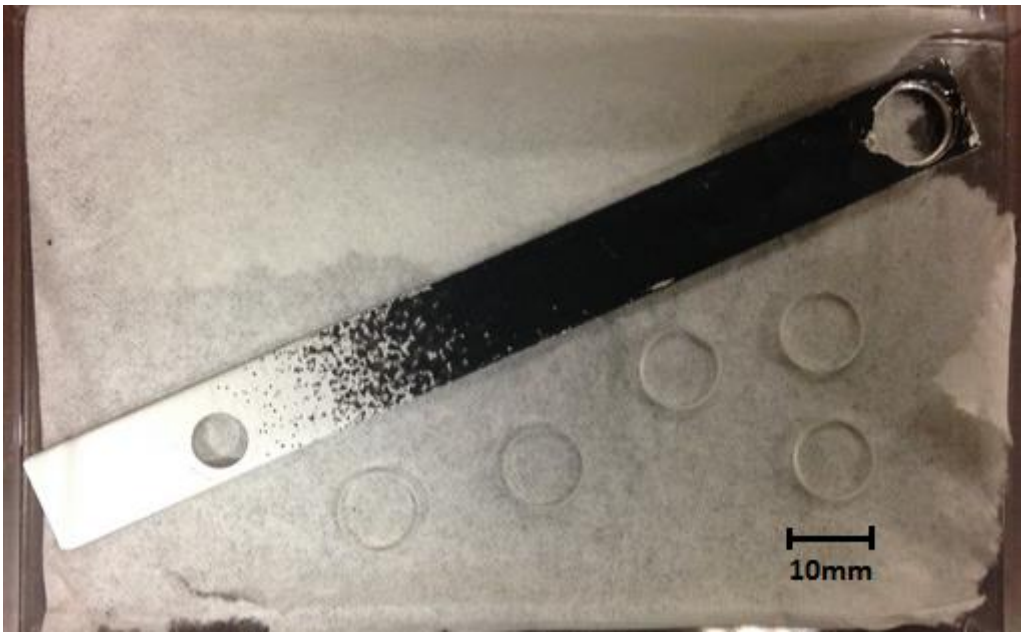

Figure 3.1: Five anti-reflection glass windows which reduce reflectance to less than 0.5%. The long piece of metal is used as a holder to position the glass windows in the path of the SID3 laser beam: the glass windows slot into the hole in the holder to the upper right of the image, and the hole to the lower left is used to attach the holder to a clamp such that it may be suspended in the path of the laser beam.

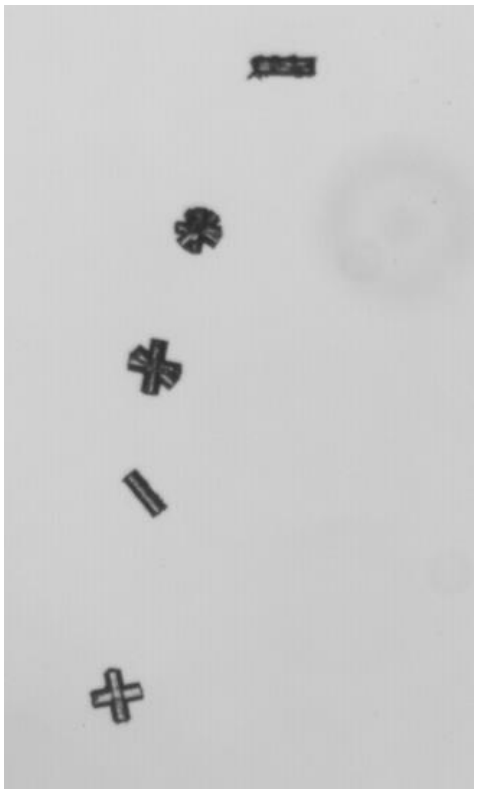

Figure 3.2: Five ice analogues lined up on an anti-reflection glass window and imaged under an optical microscope. The columns (upper analogue, and fourth analogue down) were regularly used as markers since their scattering patterns are easily identifiable. The other analogues are rosettes (second and third down), and a cross shape. The ice analogues used in the experiments varied from a few microns up to around 150µm.

3.2 The Effect of Saturated Pixels on Size Retrieval

It was suspected that having a high number of saturated pixels in an image could influence the size retrieval in a way that was not representative of the particle's actual size. Too many saturated pixels can cause the apparent merging of speckle spots, which would increase the median spot area, and therefore cause the imaged particle to be undersized. Figure 3.3 shows how a concentrated area of saturated pixels can result in an unrealistically large speckle spot.

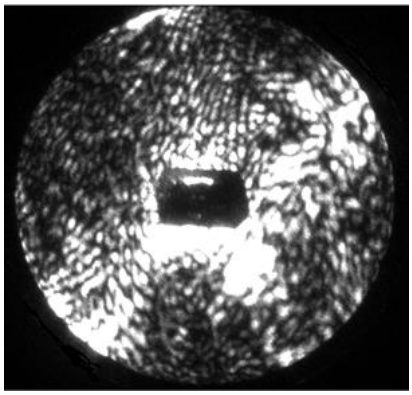

Figure 3.3: Two-dimesional scattering pattern captured by SID-3 of an ice crystal *in situ*. Many saturated pixels (bright areas) can be seen particularly towards the centre. The large areas of saturated pixels 'join up' to create an oversized speckle spot

For each ice analogue around 10 scattering pattern images were taken using SID-3, for each different camera intensity gain. The camera gain was changed to provide images which were fairly dark, images which were heavily saturated, and images in between the two extremes. Generally, around four different settings were used for each particle. The size and the roughness of the particles were estimated from each of the scattering images using the method described in section 2.2.3, and a median value was calculated for each particle at each gain, i.e. around 4 sizes and 4 roughness values per particle. This method was used for a second time, but any images containing more than 1087 saturated pixels, i.e. 0.33% of pixels, were rejected. This number was based on that used in a previous study (Ulanowski, et al., 2014).The linear regression of the measured size (from the optical microscope images) to the estimated size (from the scattering patterns) was plotted for both levels of saturation; no limit on the number of saturated pixels, and a limit of 1087 saturated pixels. The regression plots for both cases can be seen in Figure 3.4. Only ice analogues with roughness values of 0.4 and greater were included in the regression analysis. This criterion was set in order that only moderately to highly speckly images were used so that the issue of combined speckle spots due to saturated pixels could be assessed.

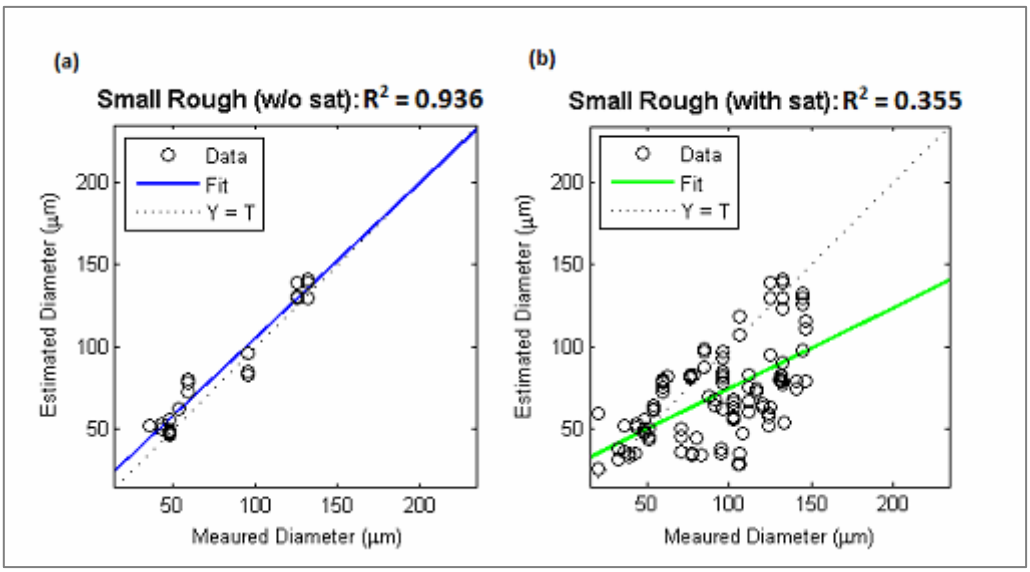

Figure 3.4: The linear regression of the measured diameter (from the images taken under the optical microscope) to the estimated diameter (from the scattering images taken by SID-3) of ice analogues. (a) Images of scattering patterns were rejected if more than 1087 pixels were saturated. (b) Images of scattering patterns were not rejected on the basis of saturated pixels. The size information in the plots came from particles which were sufficiently rough and/or complex to provide speckly scattering patterns.

The regression plot between measured and estimated particle diameter shows a very good fit where particles are only included if their scattering patterns are sufficiently speckly and contain low counts of saturated pixels. The coefficient of determination, R^2, which indicates how well the regression line fits the data, i.e. 'Fit' compared to 'Y=T' in Figure 3.4, at 0.936 it is very close to 1, i.e. a perfect fit. Therefore if images are rejected when 0.33% of pixels or more are saturated, then the retrieval of particle diameter from the scattering patterns is very reliable. This does not hold when moderate to high levels of saturated pixels are introduced; R^2 value in this case reduces significantly to 0.355. As suspected the particles with scattering images which contain more than 1087 saturated pixels tend to be undersized. As previously mentioned the particle size is calculated from the inverse of the median area of speckle spots, therefore generally larger speckle spots correspond to a smaller particle. This is consistent with the suspicion that images which include higher numbers of saturated pixels will produce unrealistically larger speckle spots and cause a particle to be undersized.

The relative error (%) was calculated for each particle used in the experiment by subtracting the estimated size from the measured size, then using the absolute value of this (i.e. the absolute error), dividing it by the estimated size, and finally multiplying by 100 such that the error was a percentage, as demonstrated below:

$$\frac{|measured\ diameter - estimated\ diameter|}{estimated\ diameter} \times 100\%$$

The particles were then put into bins depending on the number of saturated pixels in their corresponding scattering pattern; each bin consisted of around 20 particles. The root-mean-square errors (%) were then calculated for each bin, and are shown in Table 3.1. The errors were considerably lower when only images with fewer than 1087 saturated pixels were used in analysis; above this threshold the errors became substantially more significant.

Number of Saturated Pixels	RMS error (%)
<1087	15
1087 to 7000	98
7000 to 14000	96
14000 to 23000	97
23000 to 40000	97

Table 3.1: The root-mean-square error associated with sizing images from SID-3 scattering patterns which include various numbers of saturated pixels.

From the regression plots in Figure 3.4 and the RMS errors in Table 3.1, it is clear that images which contain more than 1087 saturated pixels do not allow for accurate particle size retrieval: particles tend to be oversized. For this reason images which are collected *in situ* will be rejected from further analysis if they contain more than 1087 saturated pixels. Although limiting the number of saturated pixels allowed in an image before it is rejected will lead to a reduction in data volume, it is thought that it will provide more reliable results regarding small particles (<50μm) since the number of particles which are incorrectly identified as small will be significantly reduced. The microphysics of small particles is less well understood than larger particles since they have previously been much more difficult to measure; therefore they take priority in this study.

3.3 The Degree of Speckle Required for Accurate Size Retrieval

Since the particle sizing techniques used in this thesis require measurements of the speckle spots in 2-D scattering patterns (Ulanowski, et al., 2014, and section 2.2.3.2) the minimum degree of speckle

required for the technique to produce accurate results was tested. In this section the degree of speckle is defined by the retrieved particle roughness; the higher the roughness value the more speckle is present in the scattering pattern. An optimal value was required to provide accurate sizing of particles, but simultaneously reject as few images as possible. The latter is particularly important since many images have already been discarded because they are too saturated (section 3.2) to provide a high certainty of reliability. Both laboratory data from ice analogues and *in situ* data of ice crystals were assessed to determine the best setting for the minimum degree of speckle, i.e. particle roughness.

3.3.1 Using Ice Analogues to Determine the Required Degree of Speckle

The scattering patterns and microscopic images of ice analogues were recorded using the same method as in section 3.1. The degree of speckle, i.e. roughness value, is tested to see how low it can be set to still allow for reliable results. The benefit of setting the roughness value lower than 0.4, the value used in the previous experiment (section 3.2, investigating saturated pixels), is that fewer images will be rejected and therefore more data will contribute to the analysis of ice crystals imaged *in situ*.

Any images which were considered too saturated as determined by the previous experiment (section 3.2) were rejected. The roughness values of the particles were also retrieved from the scattering patterns, using the method described in section 2.2.3. The regression of the estimated diameter from the measured diameter was then plotted six times, once for each roughness criterion: roughness greater or equal to (a) 0.1, (b) 0.15, (c) 0.2, (d) 0.3, (e) 0.4, and (f) no roughness criterion. The regression plots can be seen in Figure 3.5.

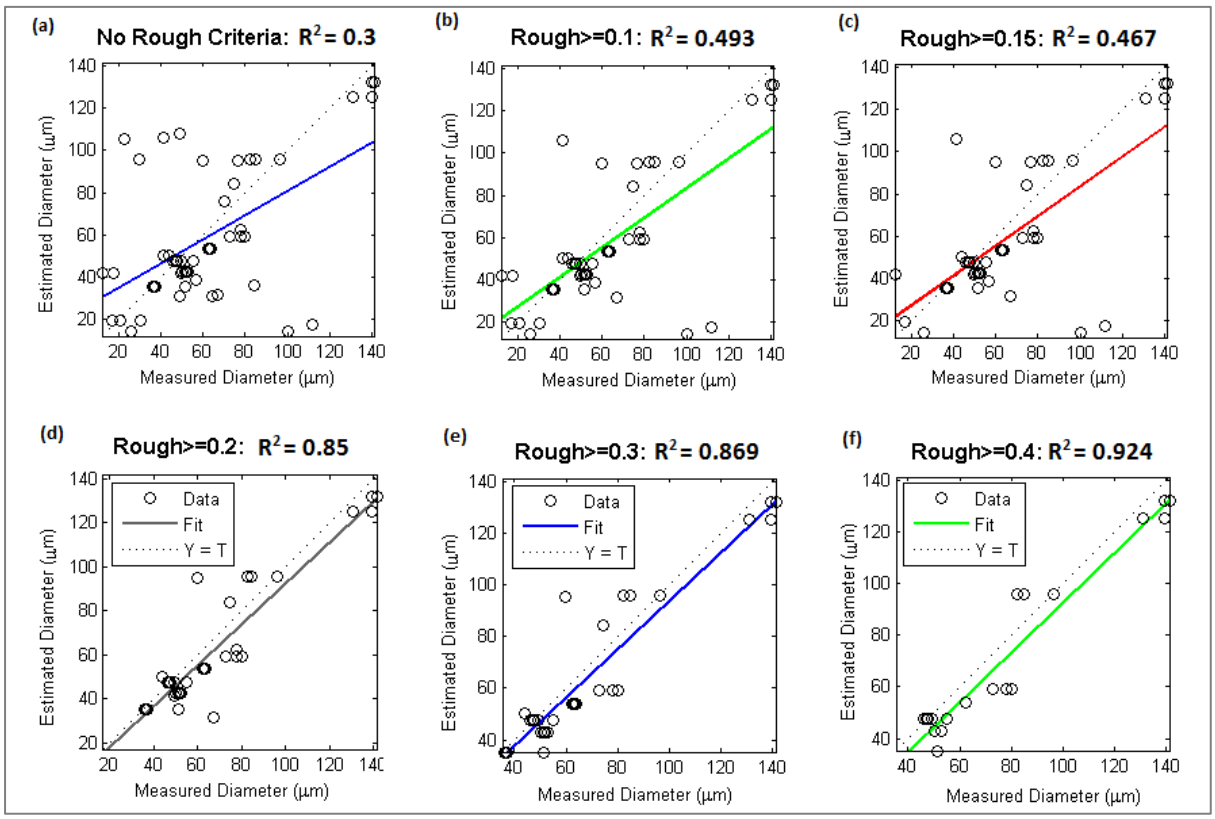

Figure 3.5: The regression between the measured diameter and the estimated diameter of ice analogues. Dark and saturated scattering pattern images were rejected from analysis for all plots. Each plot (a to f) were created when certain different roughness criteria were applied to the data. The criterion for the plots were: roughness was greater than (b) 0.1, (c) 0.15, (d) 0.2, (e) 0.3, and (f) 0.4. No roughness criterion was set in (a).

The best fit between measured and estimated diameter occurs when only particles with roughness values of 0.4 or greater are used; the R^2 value is closest to 1 (0.924). The fit for when 0.3 and 0.2 are used as the minimum values also provide good results, the R^2values are 0.869 and 0.85, respectively. The accuracy of the estimated size becomes significantly worse as the minimum roughness is reduced to 0.15 and then 0.1, and becomes worst when a minimum roughness value is not set. When the roughness is 0.15 or lower outliers begin to get introduced which heavily influence the fit between measured and estimated diameter. These outliers represent significantly missized particles, which were both undersized and oversized. Therefore to minimise inaccuracy associated with the *in situ* data particle size information is disregarded if the particles have roughness values lower than 0.2.

There still remains an element of error in the estimated diameter values since there as can be seen by the presence of a couple of outliers in Figure 3.5(d). Since setting a minimum roughness of 0.2 results in a generally good fit between measured and estimated diameters, however, and it allows

13% and 75% more data to be included in analysis than if a minimum roughness of 0.3 or 0.4 were used, respectively, it has been deemed the best choice for reliably sizing particles whose scattering patterns were recorded by SID-3 *in situ*.

3.3.2 Using *In Situ* Measurements to Determine the Required Degree of Speckle

The decision to set the minimum roughness required for an image to provide accurate particle size information to 0.2 was further tested using *in situ* data. Particle size distributions (PSDs) observed at six altitudes across three different flights were plotted from SID-3 data using the speckle techniques. The six flight sections cover a range of altitudes (9.2km to 4.6km) and temperatures (-10°C to -51°C) to accommodate for a potential range of particle sizes and roughness values. PSDs were created three times for each altitude from images which provided minimum roughness values of (i) 0.4, (ii) 0.2, and (iii) 0. The PSDs are shown in Figure 3.6.

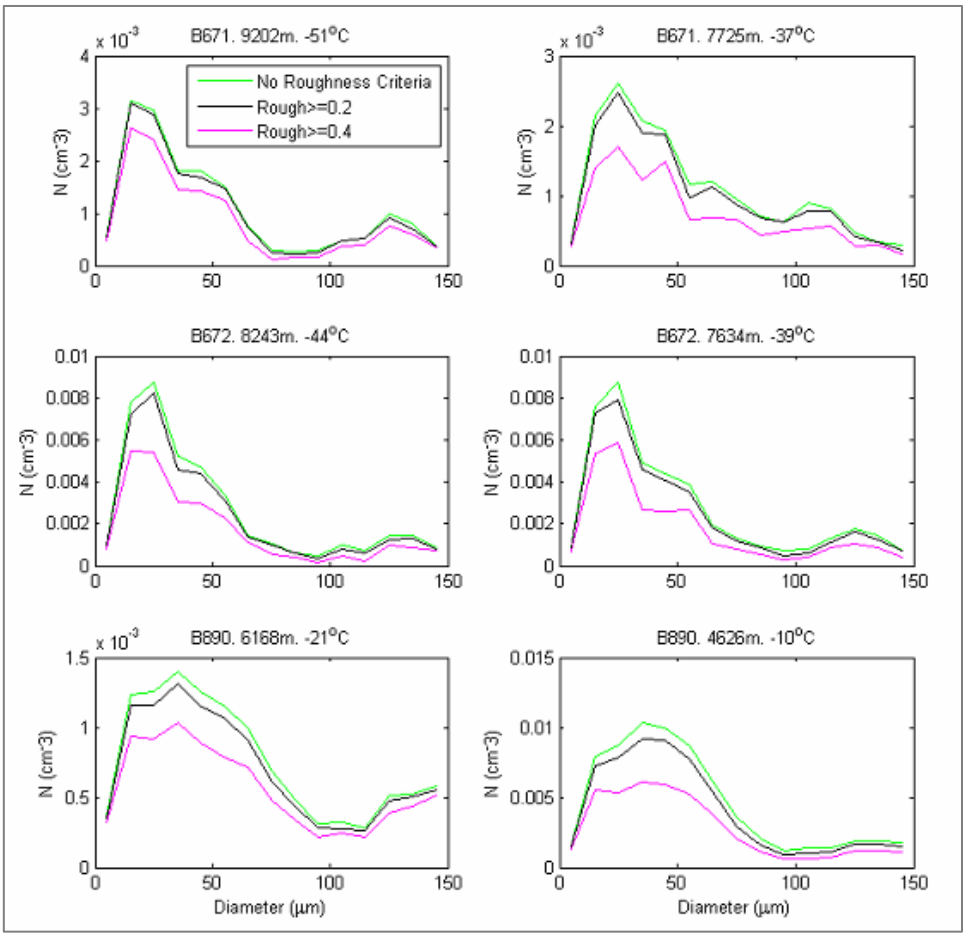

Figure 3.6: PSDs estimated from SID-3 scattering patterns collected over three flights (B671, B672, and B890). The black line represents the PSD when particles with roughness values of 0.2 and over are included. The magenta line includes particles which have roughness values of 0.4 and above. The green line represents the PSD when no roughness criterion is set.

For each PSD, over all three flights, the general shape is fairly unchanged when the minimum particle roughness is lowered from 0.4 to 0.2. As expected, however, the concentrations do increase across all diameters as a consequence of an increase in data volume when 0.2 is used as the minimum roughness. Similarly the PSDs are generally the same shape when no roughness criteria are set to when only particles with a roughness value of 0.2 or greater are used. Although the concentrations can be slightly higher when no roughness criteria is set due to fewer images being rejected they are still of the same order as the other two criteria, and almost identical to the 0.2 minimum roughness criterion at points along the PSDs. Therefore, the concentrations which have been calculated from only particles with a minimum roughness of 0.2 are expected to be representative of the actual particle concentrations that were present during *in situ* sampling.

Due to the poor fit between measured and estimated diameters when no roughness criteria is set (Figure 3.5a, R^2 equals 0.3) compared to when 0.2 is set as the minimum (Figure 3.5d, R^2 equals 0.85) it is expected that the latter is the more reliable. Therefore a minimum particle roughness of 0.2 is required for accurate size retrieval from the 2D scattering patterns imaged *in situ* by SID-3.

3.4 Minimum Mean Brightness Required for Accurate Size Estimation

During at least one flight particle size distributions (PSDs) observed in cirrus, and plotted from SID-3 data, took shapes that were not typical of PSDs often seen from cirrus measurements. It was suspected that these unexpected results were a consequence of images of scattering patterns that were too dark to provide accurate particle size information. Therefore the reliability of dark images, their origin, and the minimum mean brightness required for reliable results were investigated.

The unexpected particle size distributions (PSDs) are illustrated in Figure 3.7; they were calculated using the 2D scattering patterns at four different altitudes within cirrus cloud during flight B895.

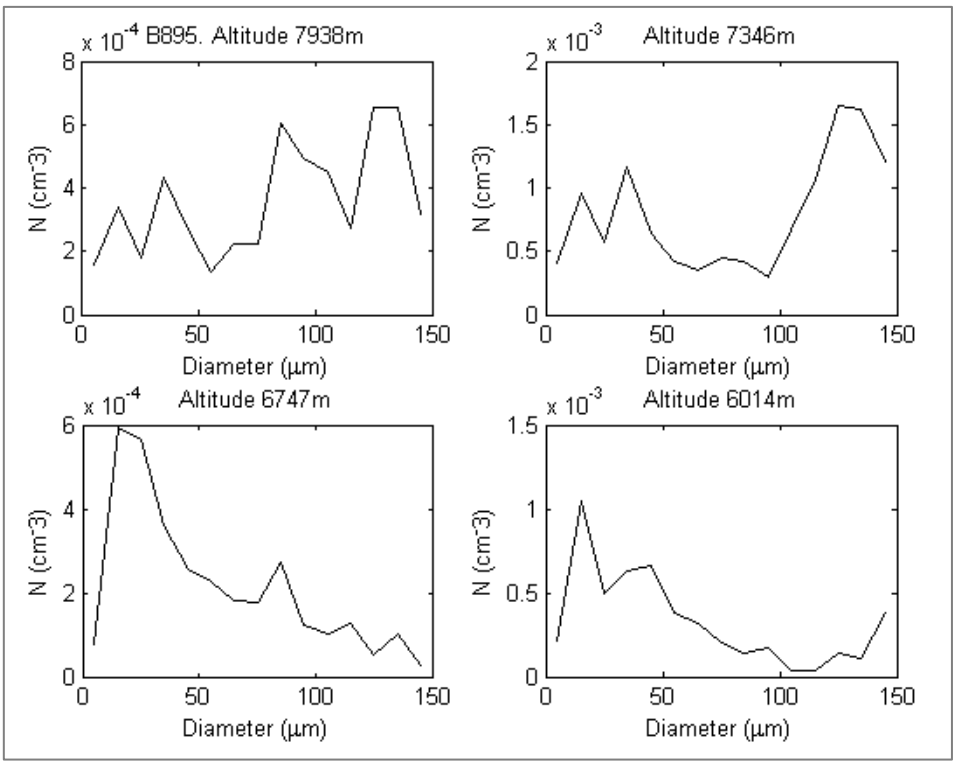

Figure 3.7: PSDs calculated using SID-3 2-D scattering patterns collected in situ during flight B895. Each plot shows the PSD at a different constant altitude. The PSDs were averaged over the period of the run at that altitude.

In the PSDs at the two higher altitudes, 7938m and 7346m, the number concentrations of particles with diameters around 100µm and larger are much higher relative to the concentrations of smaller particles than was expected. The plotted PSDs were expected to take the shape of those seen in the lower altitudes, 6747m and 6014m, especially at the very low temperatures observed; -42°C was the mean true air temperature during the highest of the four altitudes runs. At these low temperatures ice crystals would be expected to nucleate homogeneously which tends to result in the simultaneous formation of many crystals, therefore forcing competition for water vapour during growth. Due to this competition the homogeneously nucleated ice generally does not grow rapidly and high concentrations of small crystals, less than 100µm, are observed. During this flight particle size was only calculated from the scattering patterns which contained less than 1087 saturated pixels; hence image saturation was not expected to be the cause of possible mis-sizing of particles. Rather, it was suspected to be a consequence of the incorrect calculation of speckle spot areas from dark images. Figure 3.8 shows images of two scattering patterns which were recorded by SID-3 during flight B895 and the binary version of the image. The scattering patterns look very dark and it is difficult to identify any speckle spots visually. The binary images, however, show a high degree of speckle and small speckle spots. The smaller the median area of the speckle spots, the larger the diameter to

which the particle is assigned (median speckle spot area is inversely proportional to particle diameter). Therefore, these dark scattering patterns would have given rise to larger estimated particle diameters, and are suspected to be the cause of unexpectedly high concentrations at these diameters.

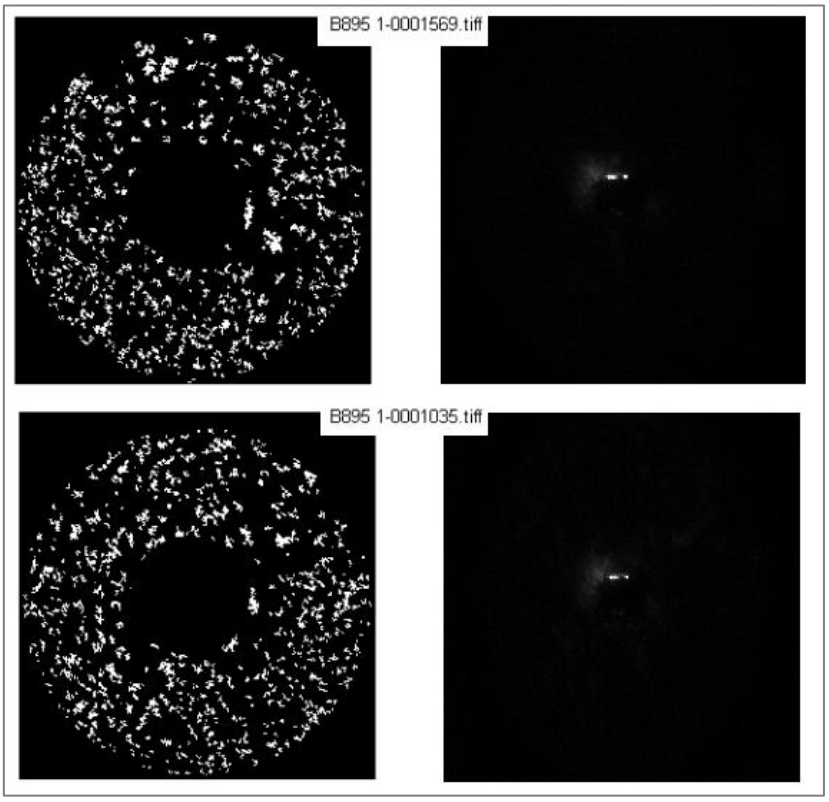

Figure 3.8: Binary images of scattering patterns of ice crystals imaged in situ during flight B895 by SID3. The scattering patterns, second column, appear very dark and so it is difficult to infer the number and size of speckle spots by eye. The binary images suggest that the scattering patterns have many small speckle spots and therefore the particles are assumed to be large. The scattering pattern on the top row has been estimated to be that of a particle of diameter 160µm, and that on the bottom line from a particle of diameter 147µm.

3.4.1 The Effect of Dark Images on PSDs of Cirrus

The PSDs at the altitudes plotted in Figure 3.7 were recalculated without the particle sizes from images which had a minimum mean brightness of less than 64 (on a 0 to 4096 scale). The resulting PSDs were plotted with the PSDs which included the darker images in Figure 3.9. Only particles with roughness values of 0.2 or greater were used and images with fewer than 1087 saturated pixels (based on results from sections 3.1 and 3.2).

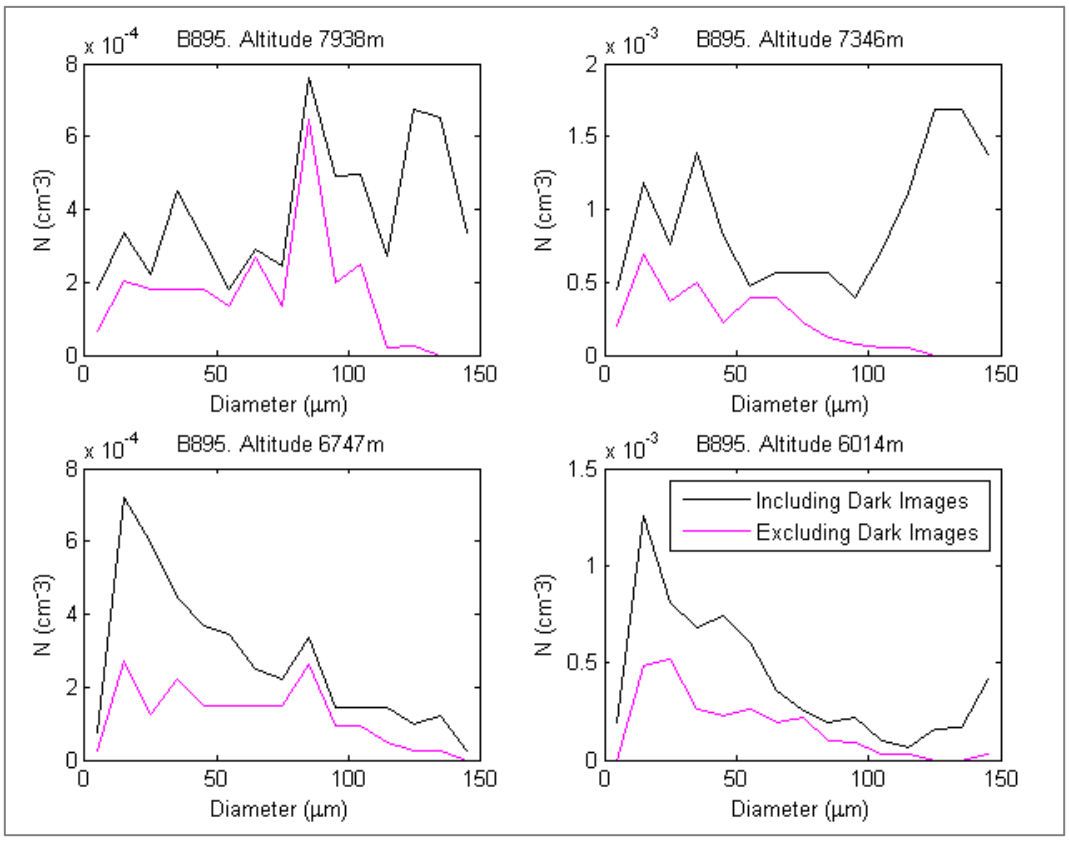

Figure 3.9: PSDs calculated from SID-3 data which was collected *in situ* during cirrus flight B895. Each plot represents the PSD at a constant altitude in the cirrus. The black line represents the PSD when dark images were included in the size retrieval. The magenta line represents the PSDs when dark images were excluded.

The shape of the PSDs estimated from the scattering patterns recorded during flight B895 appear to be heavily influenced by the presence of dark images, particularly in the larger diameter region (>100µm): the concentrations of larger particles provided the peak value in concentration for the PSDs at the two highest altitudes, but when the darker images are removed the concentrations at these diameters drop significantly.

In situ data from the ICE-D (Ice in Clouds Experiment – Dust) campaign carried out in August 2015 showed that when small particles produced dark scattering patterns the particles were significantly oversized. The PSD from SID-3 data during a straight level run (SLR) was plotted with PSDs from the CDP (3-50µm) and PCASP (0.1-3µm) probes. The SLR (run 13 B930) was chosen because it was executed over a relatively long time (40 minutes) in the presence of small to large aerosol, but no cloud; it was therefore expected that any images taken by SID-3 would be the scattering patterns of aerosol no larger than around 10µm. SID-3 gains, however, were set low so as to allow optimum characterization of much larger cloud particles. The PSDs from PCASP and CDP data in Figure 3.10 show relatively high concentrations of aerosol with diameters less than 1µm, which decreases

consistently with increasing diameter up to around 30µm. The PSD from the SID-3 data is inconsistent with the other two probes: particles with diameters greater than 30µm are well represented in the SID-3 PSD as well as an increase in concentration for those greater than 100µm. When the minimum mean brightness was set to 32 all images were rejected and no data was available, whereas when the minimum mean brightness was reduced to 16 the size information represented in the PSD in Figure 3.10 was retrieved from the images. The oversizing of the small particles is a consequence of dark images from the SID-3 probe. Therefore a laboratory experiment was set up to confirm the extent to which dark images can be missized.

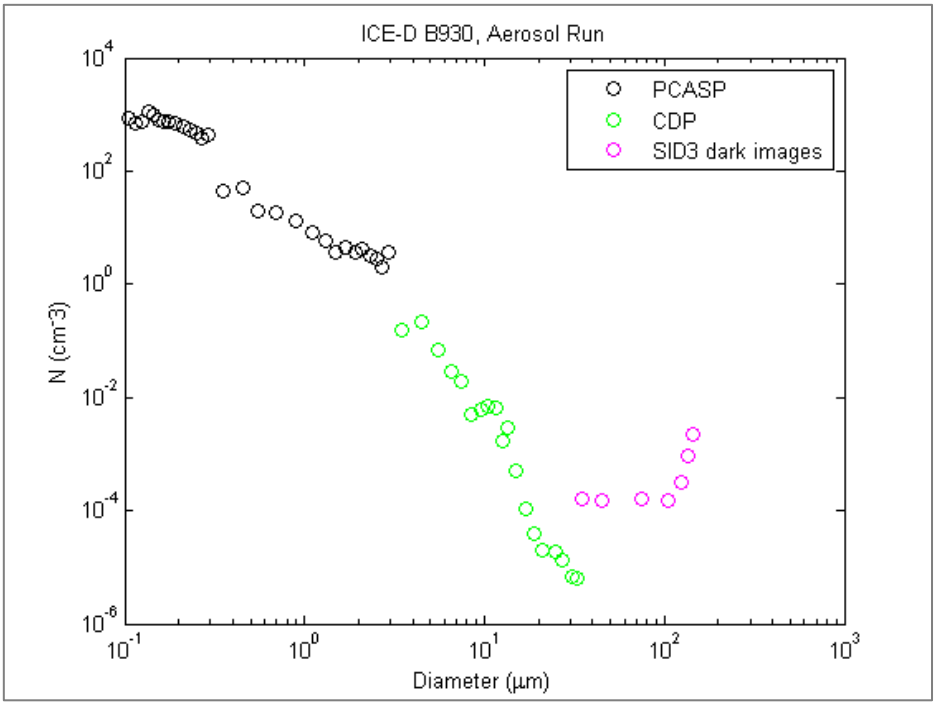

Figure 3.10: PSDs from PCASP (black), CDP (green), and SID-3 (magenta) data from a straight level run (SLR) during flight B930, which was executed out of Cape Verde. Each PSD has been averaged over the period of the SLR. The purpose of the run was to measure small dust and aerosol.

3.4.2 Using Ice Analogues to Determine the Required Minimum Mean Image Brightness

The small particles are the priority in this study since fewer probes can characterise these (<30µm) compared to those that can measure particles greater than 100µm. Furthermore, increasing the required minimum brightness will reduce the amount of SID-3 data for analysis (which is already limited to 30 data points per second because of the rate at which the camera is able to record images). It is expected that the darker images are those corresponding to smaller particles (<10µm)

because the magnitude of intensity of the scattered light becomes smaller as the particle size decreases. Therefore reducing the number of darker images will reduce the number of small particles which can be included in data analysis.

Ice analogues were used to assess whether particle size retrieval from dark images of scattering patterns created by small particles could indeed be significantly overestimated as suggested by the *in situ* data from B895 (Figure 3.9) and B930 (Figure 3.10). A similar setup was used as described in section 3.1; ice analogues were imaged under the optical microscope and their scattering patterns were recorded by SID-3. The former provided the measured circle equivalent diameters and the latter were analysed following the procedure laid out in section 2.2.3 to retrieve an estimated circle equivalent diameter. The ice analogues used had diameters between 4μm and 27μm, and had roughness values of between 0.25 and 0.75. The scattering pattern of each particle was imaged multiple times at different camera intensifier gain settings such that images with various degrees of mean brightness were taken of each particle. The estimated diameter of each particle was retrieved from the images three times: when the images had a brightness value of (i) 16 to 31.9; (ii) 32 to 63.9; and (iii) ≥64.

Similarly to the *in situ* data from flight B930, particles with measured (true) diameters less than 10μm are significantly oversized when their scattering patterns are very dark (16 to 31.9). For small particles (<10μm) the estimated diameters are all greater than 100μm (Figure 3.11) with the exception of relatively few correctly sized particles. For particles with measured diameters between 10μm and 30μm the estimated diameters also don't show high accuracy when retrieved from dark images.

It is important to note that for *in situ* cases the camera intensifier gain will be set at a constant value throughout the duration of a flight, and therefore as the particle size increases the likelihood of its scattering pattern being dark will decrease. In the laboratory experiment described here the gain was set to 180 for a dark image to be taken of the scattering pattern of a 5μm size particle, but the gain had to be reduced to 160 in order that a dark image could be taken of a 11μm size particle. It is for this reason that only particles with diameters less than 30μm have been investigated with regards to incorrect size retrieval from dark images.

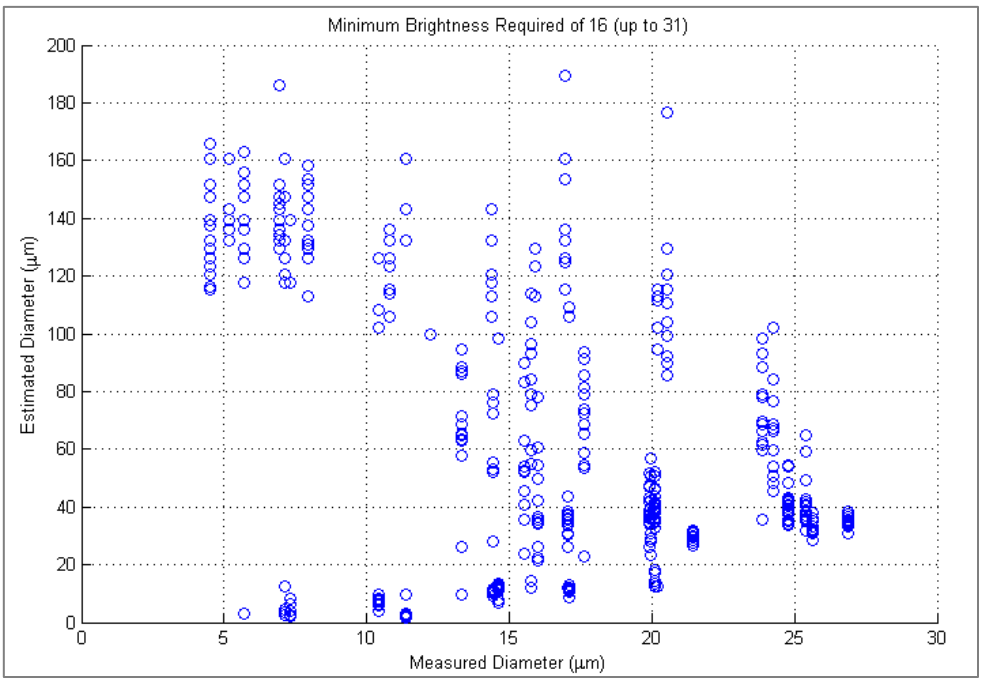

Figure 3.11: The measured diameter derived from microscope images of ice analogues plotted against the estimated diameter of the analogues estimated from their scattering patterns which were recorded by SID-3. The images were used in analysis if they had a mean brightness of between 16 and 31.

If a particle had a measured diameter greater than 10µm and the image of its scattering pattern had a low mean brightness (16 to 31.9) then it was probable (from Figure 3.11) that the particle was mis-sized severalfold. Therefore, in order to reduce the possibility of inaccurate size retrieval, the minimum mean brightness required of an image for it to be used in analysis was increased to a value of 32 (i.e. above the upper limit of the mean image brightness for data presented in Figure 3.11).

When the mean brightness is between 32 to 63.9 (i.e. $32 \leq x < 64$), or 64 and greater, particles which have been significantly missized are generally only particles with diameters close to and less than 10µm. Furthermore the estimated sizes of these particles are all greater than 100µm if they have been missized; however over half of the particles (54%) with measured diameters less than 10µm have been sized accurately. The measured and estimated particle diameters are shown in Figure 3.12 when the mean brightness was between 32 and 63.9 (blue circles), and when it was 64 or greater (red crosses). The median size for each particle in both minimum brightness cases are shown in Figure 3.13.

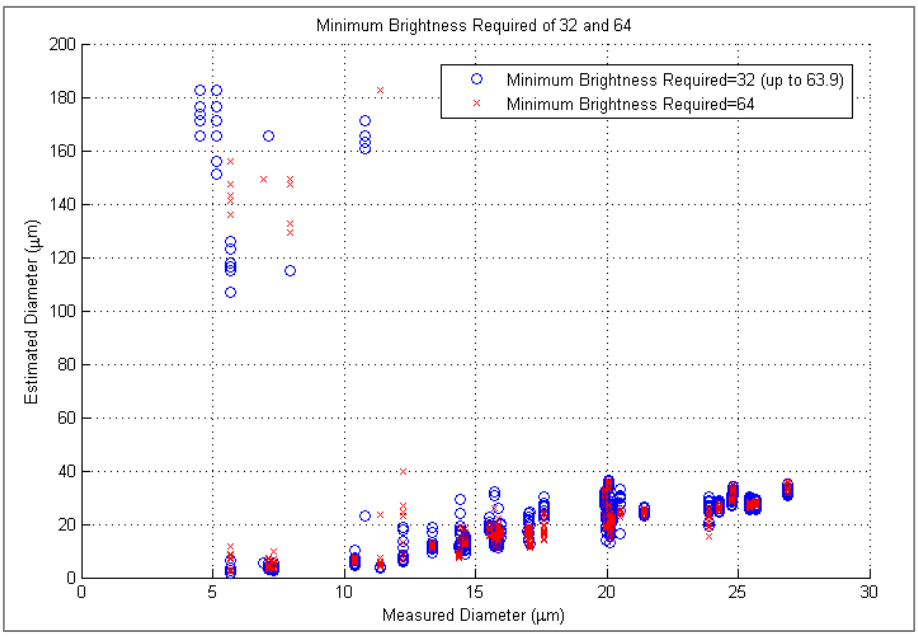

Figure 3.12: The measured diameter derived from microscope images of ice analogues plotted against the estimated diameter of the analogues estimated from their scattering patterns which were recorded by SID-3. The images were used in analysis if they had a mean brightness of (i) between 32 and 63 (blue circles); and (ii) 64 or higher (red crosses).

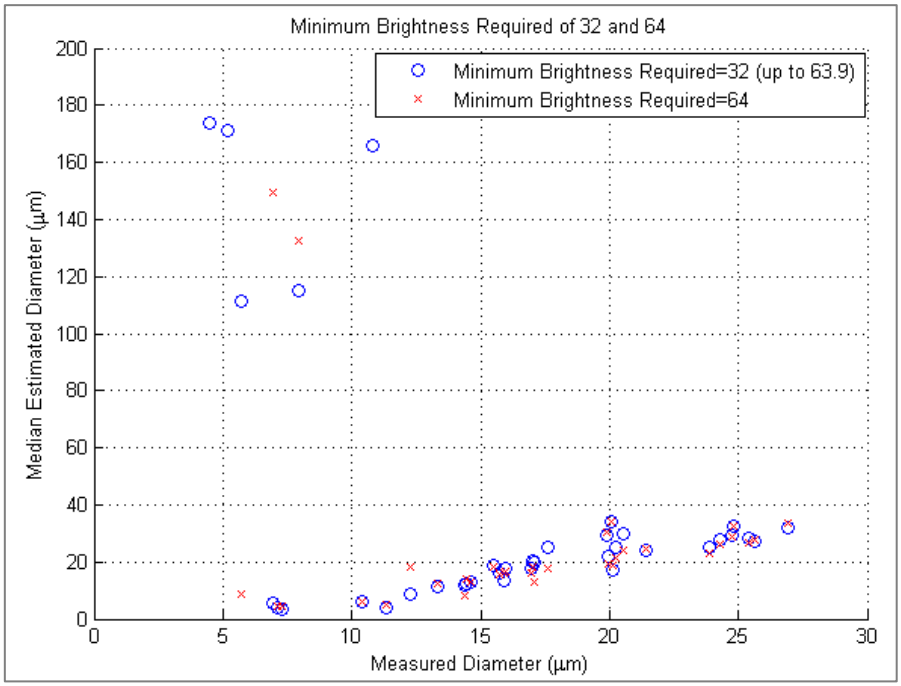

Figure 3.13: The measured diameter derived from microscope images of ice analogues plotted against the estimated diameter of the analogues estimated from their scattering patterns which were recorded by SID-3. The images were used in analysis if they had a mean brightness of (i) between 32 and 63 (blue); and (ii) 64 or higher (red).

Some particles (54%) with diameters less than 10µm have been shown to be sized correctly when the minimum mean brightness is between 32 and 63.9. Importantly, any mis-sizing only exhibits itself as particles with sizes in excess of 100µm. Smaller particles are the priority in this study and so setting the minimum mean brightness as low as possible is desirable as it will exclude fewer small particles from further analysis. For these reasons a minimum mean brightness setting of 32 has been chosen over a setting of 64 and particles with estimated sizes over 100µm should be rejected since many of them may be incorrectly retrieved from the darker images.

An exception to this would be if small particles were not present, which could be confirmed by other probes; then estimated particle sizes larger than 100µm are likely to be realistic. In this case it would not be necessary to truncate the PSDs at 100µm.

The mis-sizing does not appear to be influenced by the roughness of the particle for the roughness values represented here (0.25 to 0.75), as illustrated by Figure 3.14. Particles at the lower and upper roughness values, as well as between, have been both significantly oversized and also correctly sized. The roughness values from dark images do, however, differ from those estimated from brighter images for certain roughness measures, as illustrated in Figure 3.15.

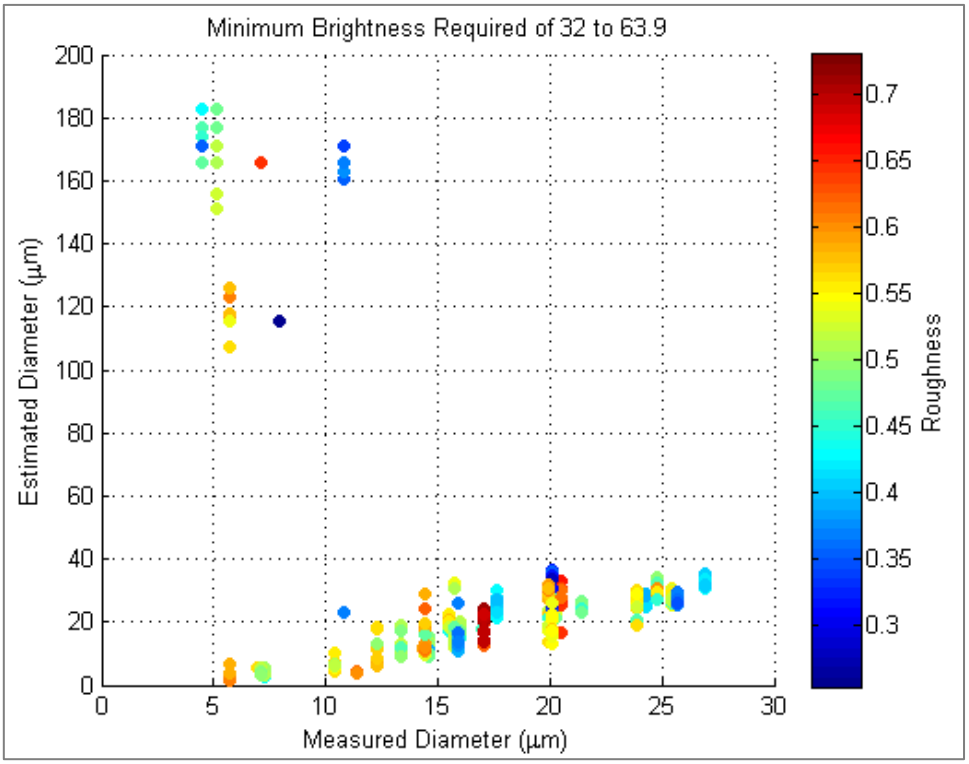

Figure 3.14: The measured diameter derived from microscope images of ice analogues plotted against the estimated diameter of the analogues estimated from their scattering patterns which were recorded by SID-3. The images were used in analysis if they had a mean brightness of between 32 and 63.9. The colour of the data points corresponds to the roughness of the particle.

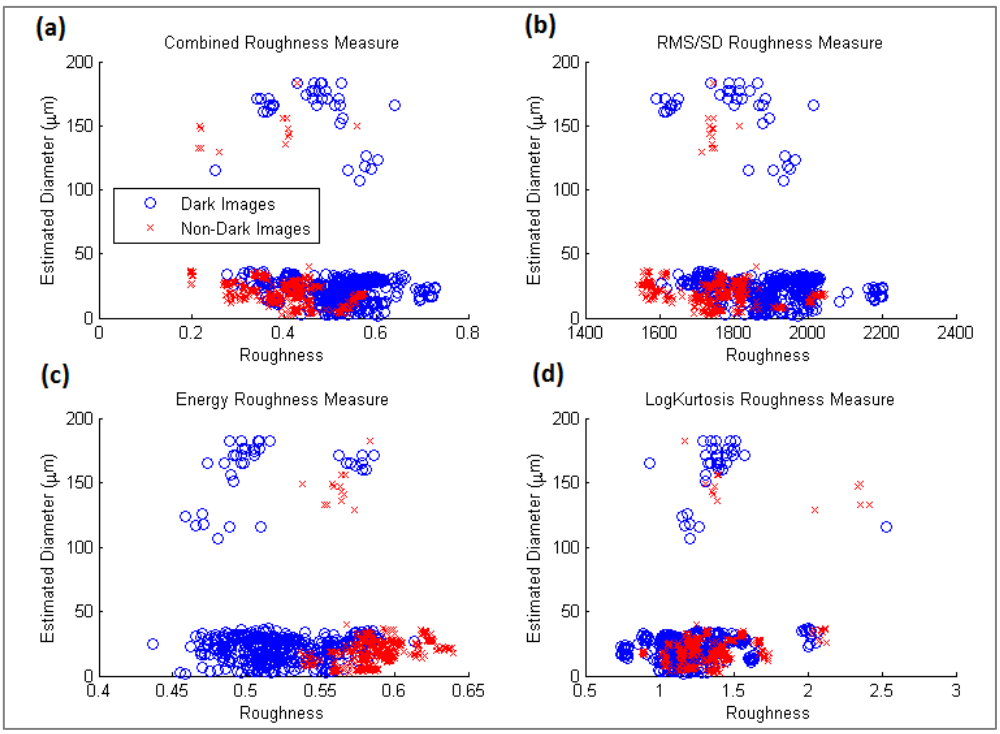

Figure 3.15: Four different roughness measures (a) combined, (b) RMS/SD, (c) Energy, and (d) Log Kurtosis estimated from dark images (blue) and non-dark images (red). The estimated diameter of a particle derived from its scattering pattern is plotted against the particle's roughness value also estimated from the scattering pattern.

As shown in Figure 3.8 by the two scattering patterns whose binary images, generated by MATLAB, show many more speckle spots than can be seen visually; and by the significant oversizing of some small particles (Figure 3.12); the actual amount of speckle can be misjudged when the image is dark. This has been shown to affect the estimated particle roughness value when three of the four roughness measures were used: (a) the combined roughness, (b) the RMS/SD roughness, and (c) the Energy roughness measure. In all of these cases the roughness was to some extent over-estimated when the images were dark compared to when they were relatively bright. This effect is likely due to a more significant influence of noise when the intensity of the scattered light is relatively low. This noise can manifest as a grainy effect on the image, which leads to misidentified speckle.

The roughness values were most consistent between dark and bright images when the log kurtosis roughness measure was used. Since dark scattering pattern images are more generally due to small particles (<30µm) the log kurtosis should be used as the roughness measure for these smaller particles if dark images are used in analysis. The most appropriate measure for particles larger than 30µm is discussed in section 4.1

3.4.3 Quantifying the Sizing Errors Introduced by Dark Images

To evaluate the extent of likely sizing errors during *in situ* measurements the number of particles with an estimated diameter larger than 100µm which were retrieved from images with a mean brightness value between 32 and 63.9 was compared to the number of particles retrieved from images with a minimum mean brightness of 64. Since larger particles scatter more light it is not expected that the scattering patterns from these particles would be dark, and therefore there should not be significantly more large particles (>100µm) retrieved from the darker images than the less dark if the sizing is accurate.

In situ data were used to estimate ratio of larger particles (100µm to 150µm) estimated from the darker images (brightness of 32 to 63.9) over those from the relatively bright (64) images. In the former case the sizes may have been retrieved from images which had a mean brightness value closer to 63.9 than 32, and so it is not necessarily expected that a significantly higher number of large particles are estimated from images when the minimum mean brightness required is set to 64. It is also possible that images with higher mean brightness values which fall into the latter case could be saturated, particularly if they are larger particles (>100µm), and will therefore be rejected from analysis. Both of these issues could result in larger particles being more common when the minimum mean brightness is set lower, even if all of the particles are being sized correctly. Therefore the data were normalized by dividing the sum of the number of large particles by the total number of data points that met the relevant brightness criteria. The method is illustrated in equation 3.1. Where images with a mean brightness between 32 and 63.9 are described as images A (darker images), and those with a minimum mean brightness of 64 are referred to as images B (brighter images).

$$Ratio = \frac{Number\ of\ large\ particles\ from\ images\ A / Number\ of\ images\ A}{Number\ of\ large\ particles\ from\ images\ B / Number\ of\ images\ B} \quad [3.1]$$

The ratio described in equation 3.1 was calculated for the four runs from B895 shown in Figure 3.7, of which two are suspected of having a high number of significantly oversized particles due to dark images (at altitudes 7938m and 7346m). It was also estimated for four SLRs which were executed as part of flight B672. This flight was chosen because the intensifier gain on the camera was set slightly higher so dark images were less common, and the influence of large particles on the PSDs was relatively low, as shown in Figure 3.16. It was expected therefore that relatively few particles were significantly oversized as a consequence of the images of the scattering patterns being dark. The four runs from B672 were chosen because they occurred at similar altitudes and temperatures to those from B895 (Figure 3.7).

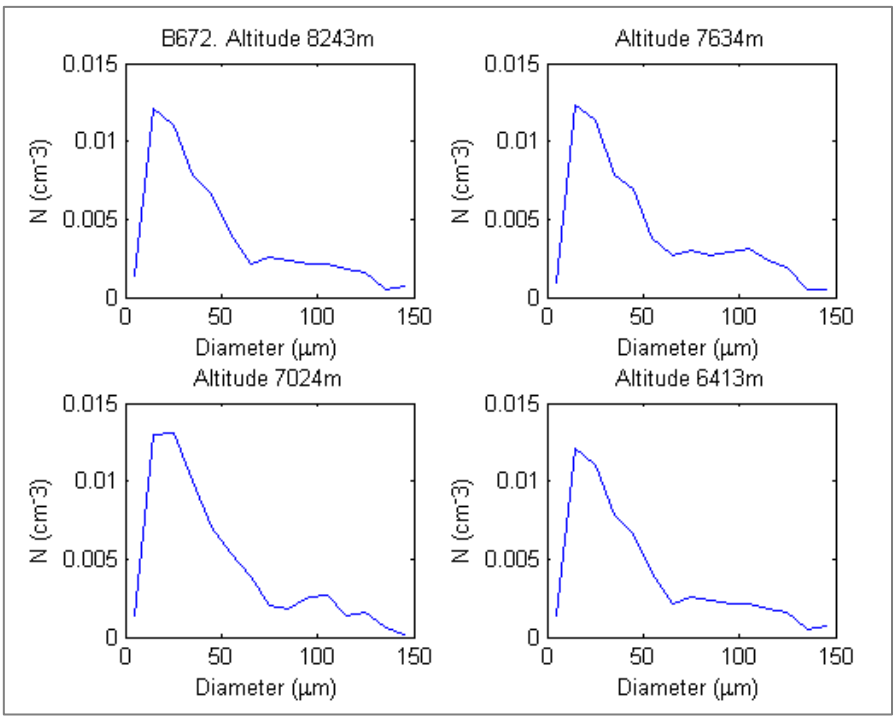

Figure 3.16: PSDs calculated using SID-3 2D scattering patterns collected *in situ* during flight B672. Each plot shows the PSD at a different constant altitude. The PSDs were averaged over the period of the run at constant altitude.

The ratios from these four runs were contrasted against those for the runs from flight B895. The ratios are shown in Table 3.2 along with the mean altitude and the mean temperature during each SLR and the flight in which it took place. Where a high degree of significant particle oversizing from dark images was expected (at 7938m and 7346m during B895) the ratio of the number of large particles from the darker images to the number of large particles from the brighter images is significantly higher than in the cases where oversizing wasn't expected to be as common. In the former case the ratios are 5.5 and 11.3; in the latter case all of the ratios are less than 2.

The ratio of 2, however, is suggestive of up to 50% of the estimated larger particles being incorrectly oversized as a consequence of dark images. Therefore, as stated previously, the PSDs should be truncated at 100µm if darker images (mean brightness>32) are used in analysis. This should act to include as many small particles with potentially dark scattering patterns as possible whilst reducing the amount of incorrectly sized particles.

Finally, we must note that any thresholds determined from the laboratory measurements are likely to be conservative (i.e. "worst case"). This is because the ice analogues were presented on supporting anti-reflection windows. Such supports necessarily introduce additional stray light, which can manifest itself as noise in the data, potentially leading to increased numbers of fine spots in the

image analysis. The spots, due to their small size, would then be interpreted as originating from large particles, leading to oversizing of smaller particles. This type of error can be expected to be reduced in *in situ* data.

Flight	Altitude (m)	Temperature (°C)	Ratio (d>100µm)
B895	7938	-42	5.5
	7346	-38	11.3
	6747	-33	1.8
	6014	-27	1.8
B672	8243	-44	1.5
	7634	-39	1.7
	7024	-34	1.65
	6413	-28	1.61

Table 3.2: The mean altitude and temperature for eight SLRs over two flights, and the ratio of the number of large particles (>100µm) when the minimum mean brightness is between 32 and 63 to the number of large particles when the minimum mean brightness is 64.

3.5 The Comparability of Images Recorded at Different Camera Settings

The degree of ice particle roughness observed *in situ* over multiple research flights has been investigated, and compared to atmospheric variables: RH_{ice}, temperature, aerosol concentration and air-mass origin. During the field campaigns, however, the camera intensifier gain of the SID-3 instrument has not always been set to the same value; the data presented in this thesis were collected when the gain was either set to 180 or 190, i.e. a maximum difference of 10 units. The intensifier gain can be changed to suit the general size of the particles that are being measured, i.e. if (large) aerosol or dust were expected then the gain would be set higher than if ice cloud were going to be observed since the particles in the former case are generally smaller and therefore the intensity of the scattered light is lower. If measurements were made in mixed-phase cloud then the ice will generally be fairly large and so a lower intensifier gain should be used to minimise saturation in the scattering pattern images.

Particle roughness has been estimated from the scattering patterns imaged by SID-3 *in situ* using the methods described in section 2.2.3.1. It was shown in section 3.3 that noise can affect the estimated size and roughness of a particle since the noise manifests as many small speckle spots in the scattering patterns. This is most pronounced in the dark images where the signal is weaker. The properties of particles with brighter images can also be miscalculated as shown in section 3.2. This is a consequence of multiple neighbouring saturated pixels giving the appearance of one larger speckle spot. When the camera intensifier gain is set higher then there is a higher possibility of both reducing mischaracterisation due to noise, and increasing mischaracterisation due to higher numbers of saturated pixels.

3.5.1 Using Ice Analogues to Assess the Comparability of Images Recorded by Different Camera Settings

In order to ensure that the roughness of particles estimated from the scattering patterns could be reliably compared over flights where the gains were not consistent, a laboratory experiment was set up. The experiment assessed how four different roughness measures were affected when the camera intensifier gain was changed. The four roughness measures were the combined roughness, which is generally the more robust measure, and the three measures of roughness which are used to create

The four roughness values, hereby referred to as Combined roughness, RMS/SD, Energy, and Log Kurtosis values, were retrieved from images taken by SID-3 of the scattering patterns of ice analogues. These were recorded at multiple camera intensifier gain settings per particle. The roughness values were retrieved from two images that were 10 gain settings apart, for each particle, i.e. a gain of 180 and of 190. The regression of each variable at the higher gain from the lower gain is plotted in Figure 3.17 for all four roughness measures.

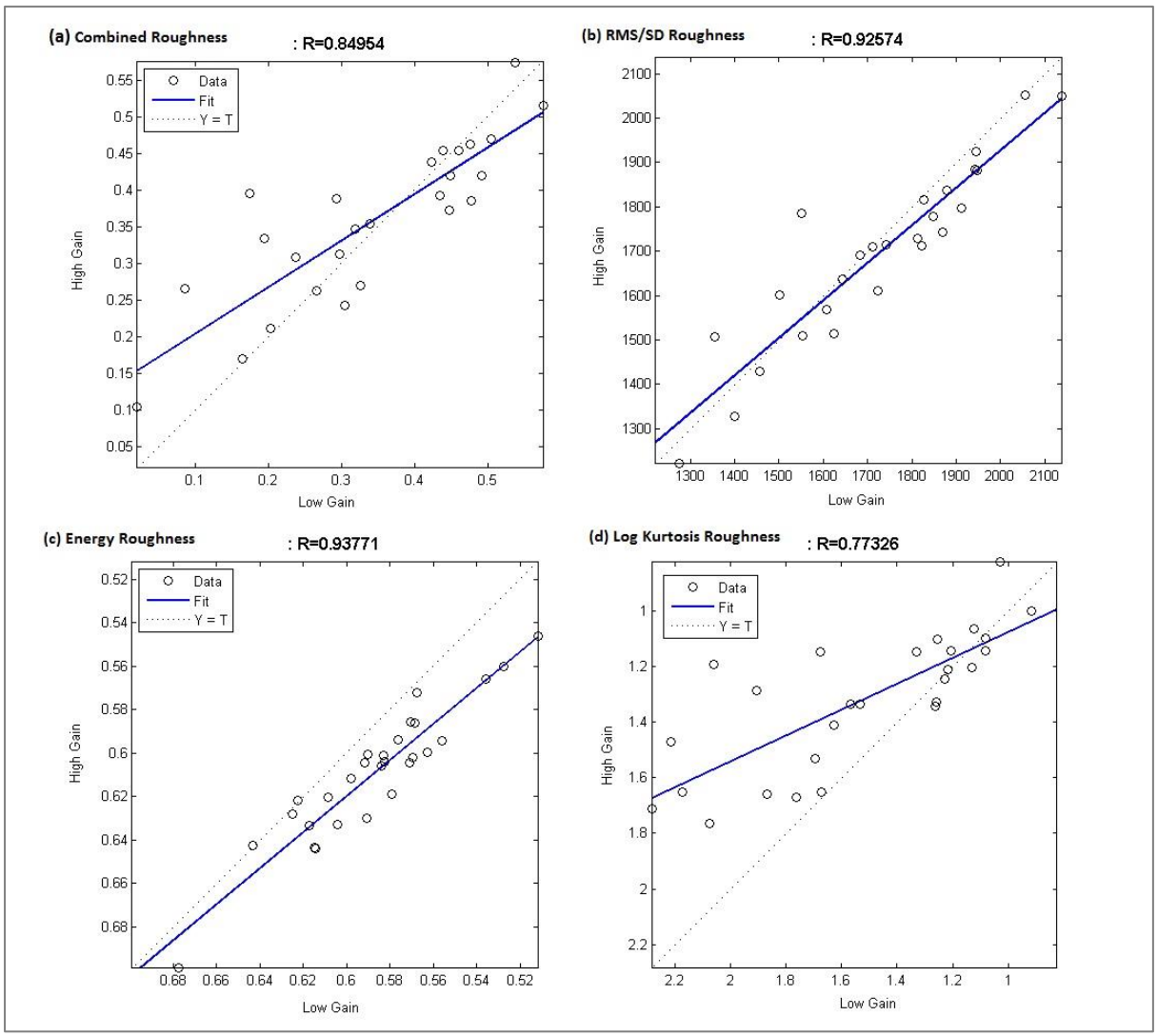

Figure 3.17: Regression plots of four measures of roughness estimated from the scattering patterns of ice analogues recorded at two different camera intensifier gains; the estimated roughness when the gain was higher is plotted against the retrieved roughness when the gain was lower. The four roughness measures are (a) the combined roughness, (b) RMS/SD [roughness], (c) Energy [roughness], (d) Log Kurtosis [roughness], all of which are described in Section 2.2.3.

As discussed in Section 3.3 Log Kurtosis was seen to be the most consistent roughness measure between images taken at different camera intensifier settings for particles smaller than 30µm. When the measure is used to estimate the roughness of larger particles, however, the fit between the Log Kurtosis values (d) at the two different gains is poor. The Log Kurtosis values are negatively correlated with the roughness; the larger particles which are rough have values which are consistent across the different gains, however the smoother (and larger) particles are inconsistent. It is clear that the Log Kurtosis roughness measure is sensitive to gain in these circumstances and should not

be used on its own to compare the roughness of particles greater than 30µm, over different flights where the setting was not consistent.

The fit between combined roughness values (a) at the two different gains is more reasonable than for the Log Kurtosis values (≥30µm), but it appears to be more prone to outliers than the RMS/SD values (b) and the Energy values (c). The Energy roughness values, similarly to the Log Kurtosis, are negatively correlated with roughness and the roughness is therefore mostly underestimated when the gain is set high compared to when it is low. This could be a consequence of saturation when the higher gain is set. The RMS/SD roughness values appear to be less sensitive to gain and provide a better fit between the two gain settings than any of the other roughness measures. The RMS/SD roughness measure has therefore been identified as a method which will provide a high degree of consistency over data collected at different gains. Therefore the values from this measure are used to compare roughness between different flights where the camera gain settings were not identical for particles larger than 30µm.

The RMS/SD values were scaled such that new values, between 0 and 1, were comparable to the scale of the combined roughness values. The scaling factor was determined using a least squares fit between the two roughness measures. Since the combined roughness could be more sensitive to gain, any outliers were rejected, this left only particles whose combined roughness values differed by less than 0.07 between the two intensity gains. The included and excluded particles can be seen in Figure 3.18 by the black and blue points, respectively.

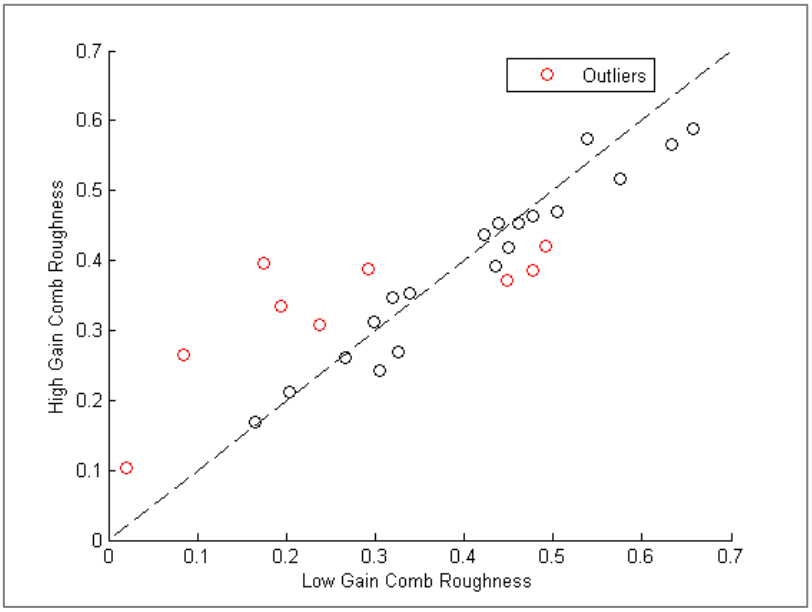

Figure 3.18: Particle roughness estimated from scattering patterns when the camera intensifier gain was high plotted against the roughness when the intensifier gain was low. The combined roughness measure was used. Outliers are

plotted in red and defined as data points which exhibited a difference of 0.07 or greater between the combined roughness value at higher gain and at lower gain.

A least squares fit was applied to the combined roughness and the RMS/SD roughness for the high gain and for the low gain separately. It was not expected that the least squares fit would be significantly affected by the change in gain since any data points which were heavily sensitive to gain had been removed previously. The fit produced the equations [3.1] and [3.2] for the high gain and the low gain respectively.

$$Combined\ Roughness\ Equivalent = -0.50176 + 0.00050678(RMS/SD\ Roughness) \quad [3.1]$$

$$Combined\ Roughness\ Equivalent = -0.58722 + 0.00054696(RMS/SD\ Roughness) \quad [3.2]$$

Since the equations [3.1] and [3.2] were not expected to differ as a consequence of change in gain, they were averaged to provide a scaling factor, equation [3.3]. The scaling factor was applied to the RMS/SD roughness values such that they took values between 0 and 1 which corresponded to the equivalent combined roughness value. The scaled values (RMS/SD combined-rough-equivalent) are plotted against the combined roughness values for both gains in Figure 3.19; the outliers have not been included.

$$Combined\ Roughness\ Equivalent = -0.54449 + 0.00052687(RMS/SD\ Roughness) \quad [3.3]$$

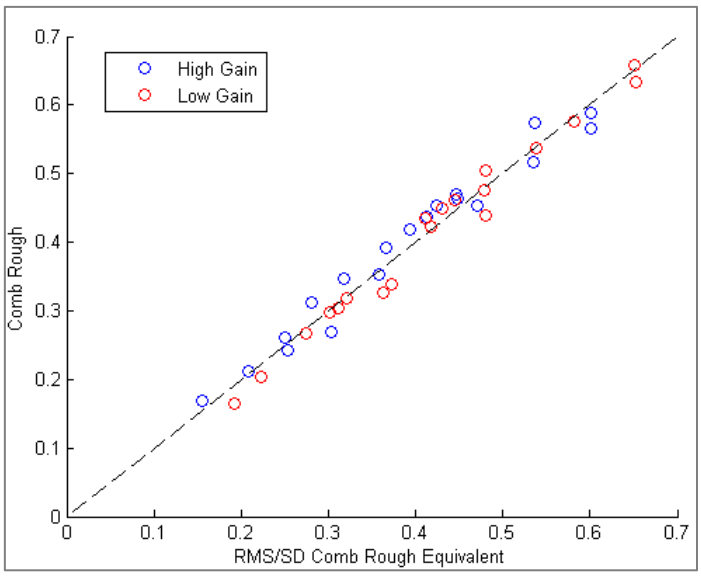

Figure 3.19: The combined roughness plotted against the scaled RMS/SD roughness values of ice analogues, derived from the scattering patterns when the camera intensifier gain was set to high gain (blue) and low gain (red). The equation used to scale the values was the average of equations [1] and [2].

The outliers that were excluded in order to estimate the equation to scale the RMS/SD roughness to values between 0 and 1 were re-introduced after the equation was determined. The same scaling equation was applied to these RMS/SD roughness values, and the regression between the high gain values and the low gain values was plotted in Figure 3.20. The plot is the same as the original regression plot of the RMS/SD roughness values at two different gains in Figure 3.17(b) with regards to the position of the data points, i.e. the fit is the same (R^2 is 0.899), but the RMS/SD values are now comparable to the combined roughness values (0 to 1), which are used in further chapters when data are not being compared between different flights since it is generally the more robust measure (assuming constant gain) (Ulanowski, et al., 2014).

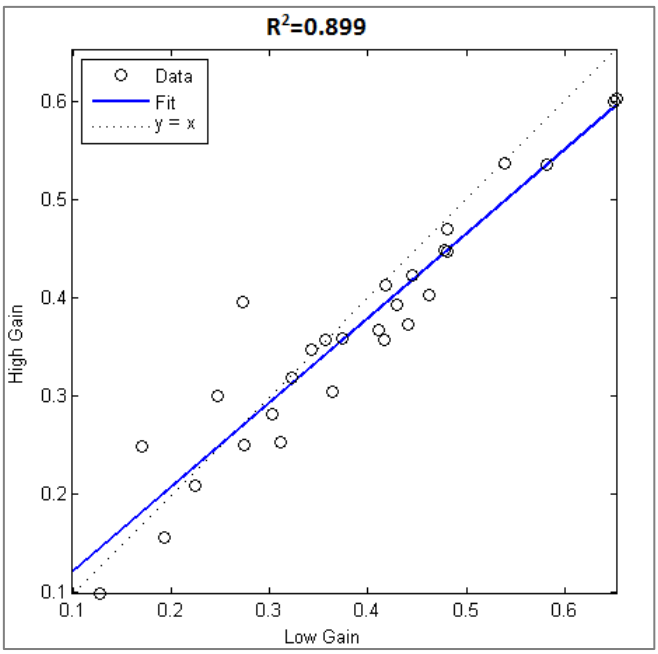

Figure 3.20: Particle roughness estimated from scattering patterns when the camera intensifier gain was high plotted against the roughness when the intensifier gain was low. The scaled RMS/SD roughness measure was used, and the intensifier gain values were 10 units apart.

Similarly to the RMS/SD values, an equation was established to convert the log kurtosis roughness values to a combined-roughness-equivalent using the same method as in the RMS/SD case; this measure can then be applied to particles smaller than 30µm. The data presented in Figure 3.17 (a) and (d) were used to find a least-squares-fit between the two roughness measures after any outliers from both roughness methods had been excluded. The resulting scaling equation is presented as equation [3.4].

$$Combined\ Roughness\ Equivalent = 0.853625 - 0.30231(Log\ Kurtosis\ Roughness) \qquad [3.4]$$

The log kurtosis roughness values have been shown to be consistent over different gain settings in section 3.2.2 (Figure 3.15d) for particles smaller than 30µm. For particles greater than 30µm the scaled RMS/SD values are plotted in Figure 3.21 as a histogram; the percentage of scaled RMS/SD values which fell into each bin from 0 to 1 with a bin width of 0.1 are plotted separately for the low gain (dark blue) and the high gain (teal) cases. The higher roughness values (0.5 to 0.7) agree perfectly for both cases, i.e. the percentage of particles with a RMS/SD value of 0.5 and greater is the same at both gain settings. Therefore, when only the roughest particles are compared between multiple flights then plotting the scaled RMS/SD values as histograms with bin widths of 0.1 would be appropriate. If particles exhibiting a wide variety of roughness values are required during an investigation over multiple flights, however, it could be less reliable to use a bin width of 0.1 to

group roughness values. This is highlighted by Figure 3.21 in which there are obvious differences between the two gain settings with regards to the percentage of particles observed with lower roughness values (0 to 0.5).

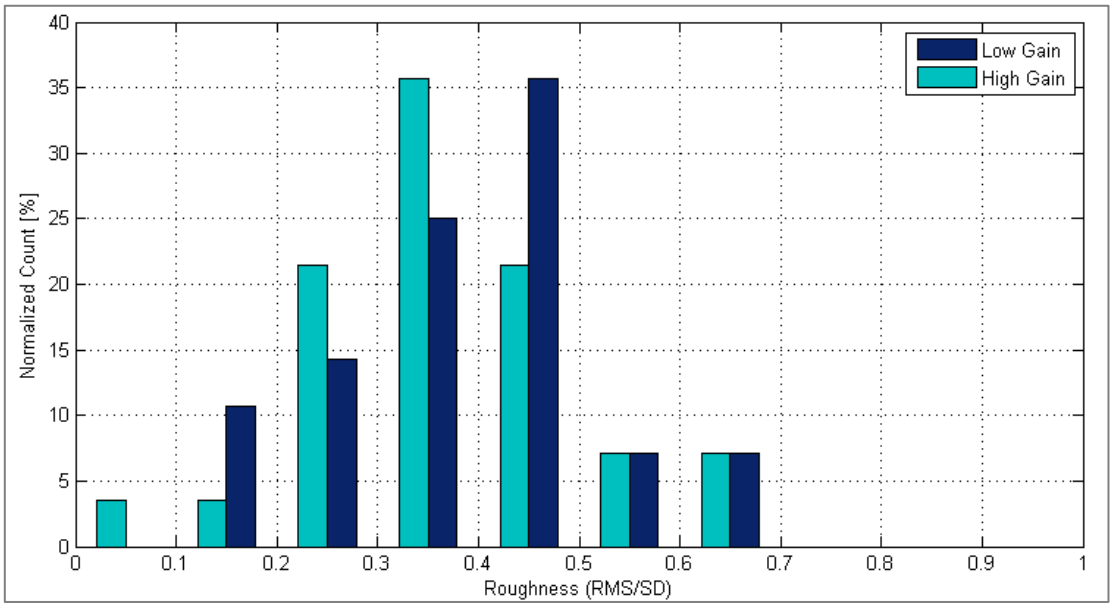

Figure 3.21: Histogram showing the percentage of test particles with specific roughness estimated from the scattering patterns which were recorded when the camera intensifier gain was set low (dark blue) and when the gain was set high (teal). The RMS/SD roughness measure has been used as the particle roughness values. There are 10 bins with width 0.1.

Where two or more flights are investigated and the roughness of the particles are compared over a range of values, and if the camera intensifier was not set to the same gain over all of the flights, then the scaled RMS/SD values may be used if the data are organised into roughness bins with a larger width, as illustrated in Figure 3.22. In Figure 3.22 four bins have been used, each with a width of 0.25. In this case the percentage of particles falling into each roughness bin shows good agreement between the different gain settings. The four bins may be referred to as particles which are: (1) smooth, (2) lightly rough, (3) moderately rough, and (4) severely rough. This categorization sufficed for comparisons between flights. Where individual flights were investigated in more depth (where the gain is constant) then smaller bin widths were used; the combined roughness was also used because it has been tested and is trusted to give roughness values which are correct at least relative to each other when the gain is not changed (Ulanowski, et al., 2014).

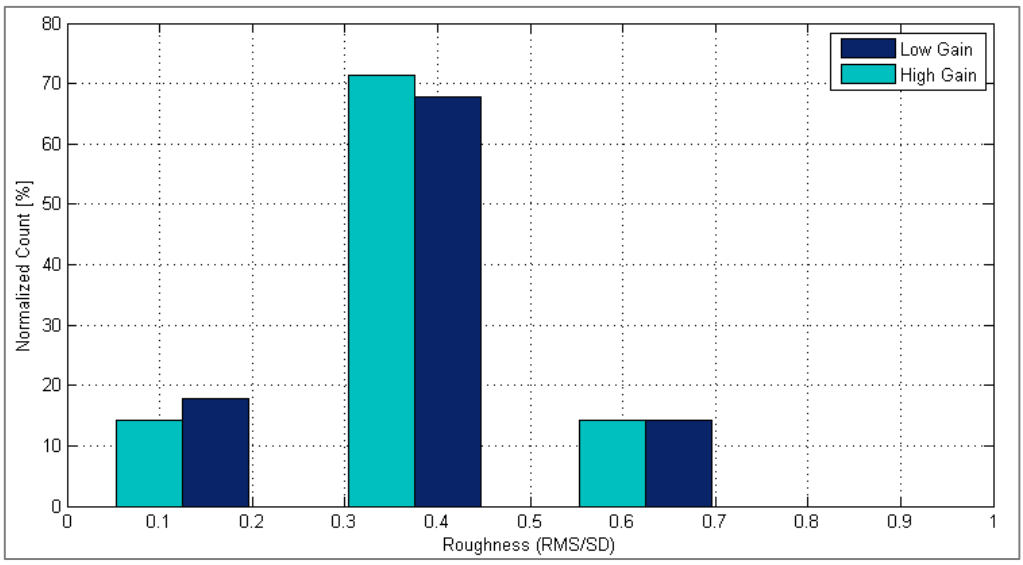

Figure 3.22: Histogram showing the percentage of test particles with specific roughness estimated from the scattering patterns which were recorded when the camera intensifier gain was set low (dark blue) and when the gain was set high (teal). The RMS/SD roughness measure has been used as the particle roughness values. There are 4 bins with width 0.25.

An uncertainty on the normalized count value was calculated for both of the binning systems; the counts at high gain and at low gain were subtracted from each other for each of the bins, and the root-mean-square of the values were determined. In the case where ten bins were used the uncertainty was ±6.6%, and in the case where only four bins were used the uncertainty was ±2.5%. The uncertainties were calculated a second time, this time assuming that the number of bins were 7 and 3 since there were zero particles in the final 3 bins and the final 1 bin for the 10 bin case and the 4 bin case respectively. This yielded uncertainties of ±7.9% when 10 bins were used and ±2.9% when only 4 bins were used.

4 Occurrence of Ice Particle Roughness *in Situ*

4.1 *In situ* measurements of roughness

Sections of five flights were chosen for particle roughness analysis and comparison. Two of the flights were executed during the PIKNMIX campaign in January 2012 (B671, B672), and the other three during the CIRCCREX campaign in March 2015 (B890, B894, B895). All five flights were conducted out of Prestwick airport and measurements were taken in the surrounding area. The flights were chosen based on the presence of ice cloud. A one hour section was selected from most flights during which ice cloud was detected; ice cloud was more elusive during flight B895 than the other flights and so a half hour section of this flight was used. Although measurements were fairly consistently made in-cloud during flight B890, only a 30 minute section was used here based on the criteria discussed below.

The altitude, temperature, RH_{ice}, and particle concentrations from SID-3 were examined to determine the start and end time of the one hour sections: the concentrations were taken into account primarily to locate periods during which the aircraft was in cloud. The altitude from GIN, temperature from the Rosemount de-iced sensor, and RH_{ice} calculated using WVSS2 data, were then used to confirm that the cloud was ice and unlikely to contain liquid water. Each flight was considered uniquely, and the before mentioned atmospheric variables are shown during the selected sections in Figures 4.1 to 4.5.

Each section occurs at an altitude of over 6km, above which ice clouds are expected to form (Hamblyn, 2008). Where the temperature was 233K (-39°C) or less, and the RH_{ice} was 100% or greater the cloud is expected to consist of entirely ice (Irvine, et al., 2012), and these sections were chosen. In order to extend the amount of data and the number of different ice cloud cases, however, sections were included which may have fallen short of these requirements. In these cases the SID-3 scattering patterns were inspected visually to ensure that only ice was present and no liquid water droplets were detected, i.e. there were no scattering patterns which resembled concentric rings.

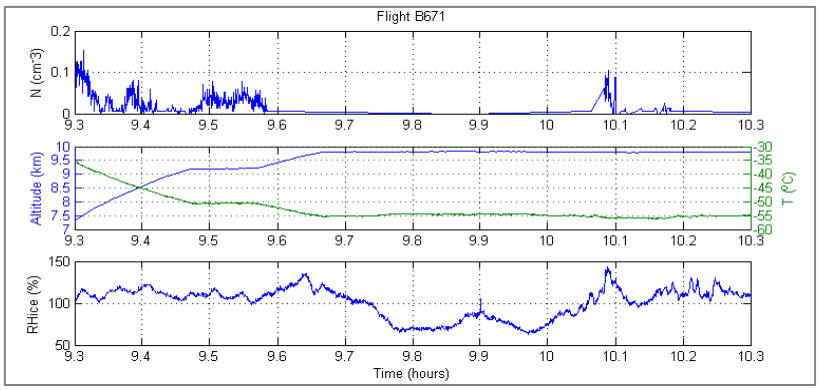

Figure 4.1: Particle concentrations derived from SID-3 data (top plot); altitude (blue) and temperature (green) (middle plot); RH_{ice} (bottom plot) all against time during a period of flight B671 in which ice cloud was measured.

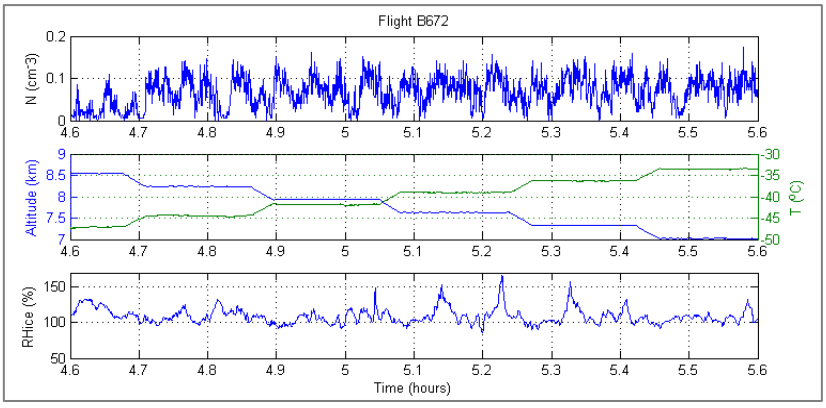

Figure 4.2: Particle concentrations derived from SID-3 data (top plot); altitude (blue) and temperature (green) (middle plot); RH_{ice} (bottom plot) all against time during a period of flight B672 in which ice cloud was measured.

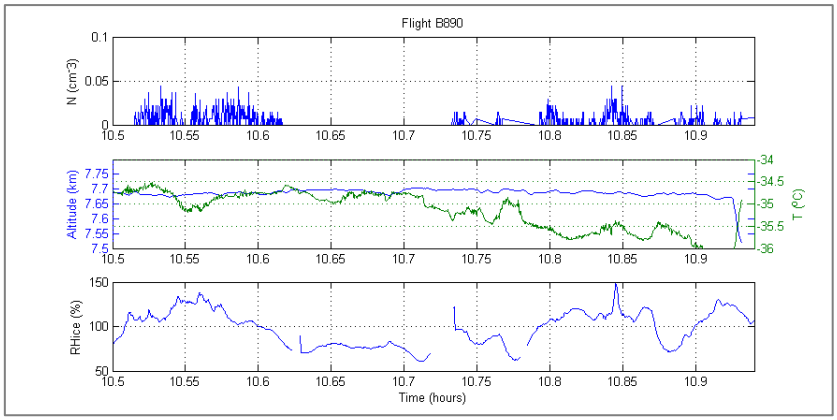

Figure 4.3: Particle concentrations derived from SID-3 data (top plot); altitude (blue) and temperature (green) (middle plot); RH_{ice} (bottom plot) all against time during a period of flight B890 in which ice cloud was measured.

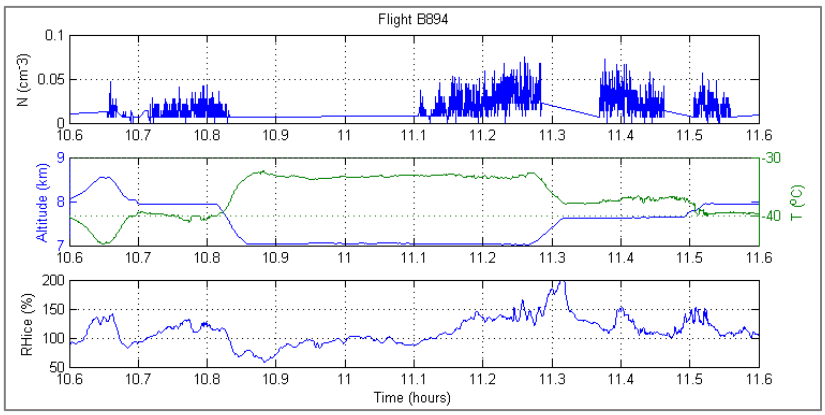

Figure 4.4: Particle concentrations derived from SID-3 data (top plot); altitude (blue) and temperature (green) (middle plot); RH_{ice} (bottom plot) all against time during a period of flight B890 in which ice cloud was measured.

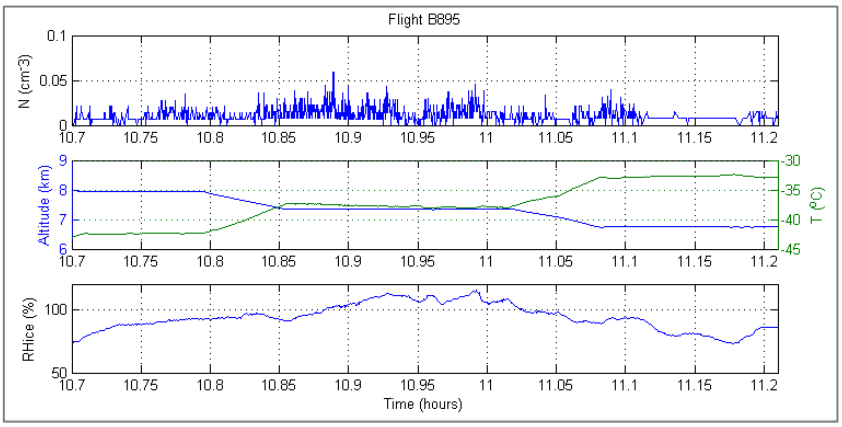

Figure 4.5: Particle concentrations derived from SID-3 data (top plot); altitude (blue) and temperature (green) (middle plot); RH_{ice} (bottom plot) all against time during a period of flight B895 in which ice cloud was measured.

The RMS/SD and log kurtosis roughness values were calculated from the scattering patterns recorded by SID-3 for the five periods of *in situ* measurement illustrated in Figures 4.1 to 4.5. The scaling equations (Equation 4.3 and 4.4) were used to convert the values to between 0 and 1 such that they were comparable to the combined roughness scale. Following the image criteria determined in chapter 3 only particles with estimated diameters of less than 100µm were used in this analysis. Furthermore the size and roughness of particles were only retrieved from images of scattering patterns which had a minimum mean brightness of 32 and a maximum of 1087 saturated pixels. The scaled RMS/SD roughness values (particles ≥30µm) and scaled log kurtosis roughness values (particles<30µm) for each flight section were arranged into four bins corresponding to different degrees of roughness: smooth, lightly rough, moderately rough, and severely rough, as shown in Figure 4.6.

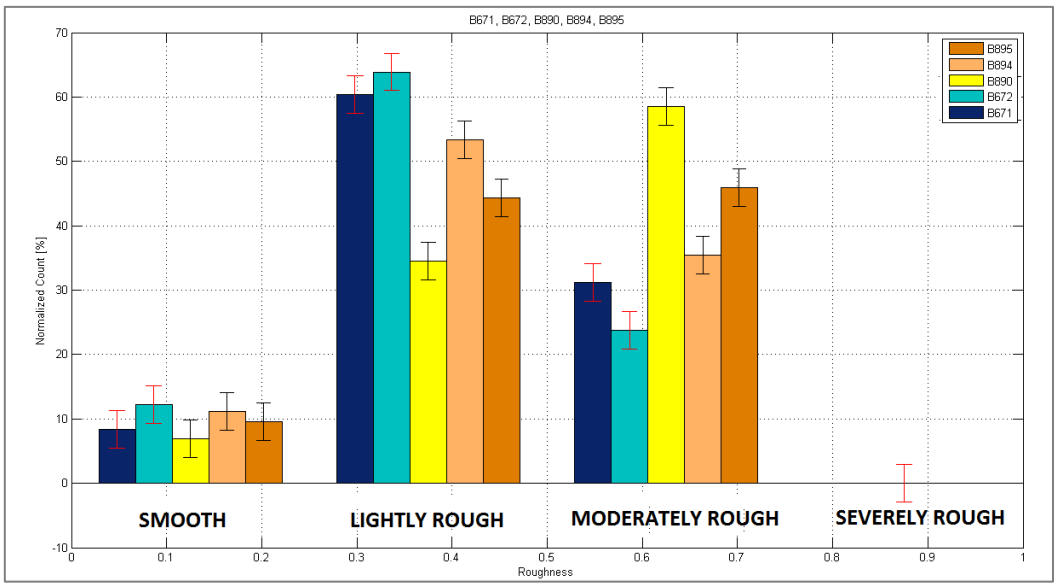

Figure 4.6: The percentage of particles which were classed as smooth, lightly rough, moderately rough, and severely rough over 30 to 60 minute periods during the five different flights (B671, B672, B890, B894, B895). The roughness values were estimated from the SID-3 recorded scattering patterns. The errorbars represent the uncertainty in the measurement when data which were not recorded using the same camera intensifier gain were compared (as discussed in Section 3.5)

The mean of the normalized counts over all five flight sections for each roughness bin were calculated and have been plotted in Figure 4.7. The means are also shown in Table 1 along with the counts for individual flights; the highest count value has been highlighted for each flight and for the mean of all the values.

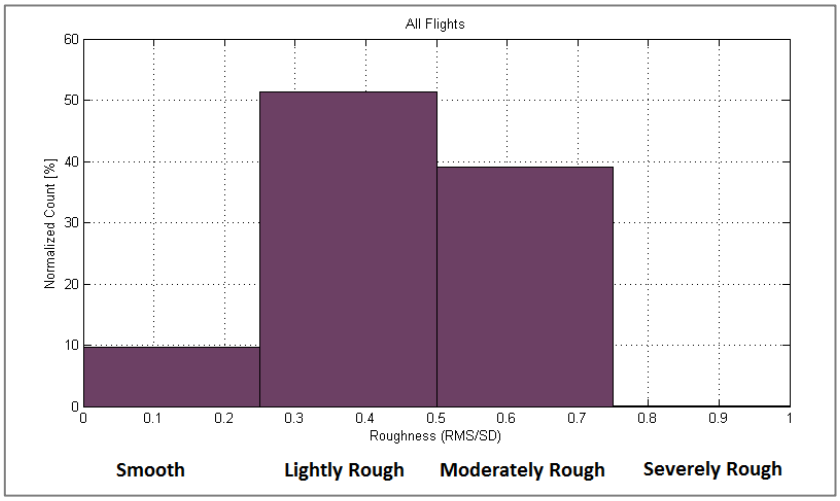

Figure 4.7: The mean percentage of particles which are smooth, lightly rough, moderately rough, and severely rough over all five sections of the multiple flights combined (B671, B672, B890, B894, B895). The percentage of particles at given roughness values were normalized for each flight section and then the mean value was taken, and plotted against the corresponding roughness value.

The majority of particles (51%) over the five flight sections were categorised as lightly rough; the second most common roughness type was moderately rough (39%). Smooth particles made up 10% of the total particles, and <0.02% were classed as severely rough. During flight sections from B671, B672, and B894 lightly rough particles were the most common (61%, 64%, 53% respectively); the most common degree of roughness during B890 and B895 were moderately rough, which made up 59% and 46% of the total particles, respectively. Over all five flights the percentages of smooth particles were fairly consistent (8% to 11%), and the same applies to severely rough particles (≈0%). There were more lightly rough particles than moderately rough particles during flights B671 and B672 (ratios of 2.0 and 2.7 respectively) compared to flights B890, B894, and B895 (ratios of 0.6, 1.5, and 0.9 respectively).

The roughness values estimated during the five flight sections have been compared to the relative humidity with respect to ice (RH_{ice}), the temperature, the aerosol concentration, and the air-mass origin to determine whether there is any obvious link between ice roughness and the atmospheric environment, as well as investigating the cause of the different ratios of lightly rough particles to moderately rough particles between different flights.

	Normalized Percentage of Particles with Specific Roughness			
Flight	**Smooth**	**Lightly Rough**	**Moderately Rough**	**Severely Rough**
B671	**8**	**61**	**31**	**0**
B672	**12**	**64**	**24**	**0**
B890	**7**	**34**	**59**	**0**
B894	**11**	**53**	**36**	**0**
B895	**10**	**44**	**46**	**0.0786**
Mean	**10**	**51**	**39**	**0.0157**

Table 4.1: The percentage of particles per flight section, and the overall mean, which are smooth, lightly rough, moderately rough. The highest percentage per section, and for the mean, is highlighted.

4.2 Correlation with Air Mass Origin

The NOAA HYPSPLIT model was used to compute 5 day back trajectories of the air-mass probed during the five flight sections investigated here. Three altitudes were chosen per flight, as well as the

latitude, longitude, and the end time. Cloud was present at the three altitudes chosen. The outputted back-trajectories are shown in Figure 4.8.

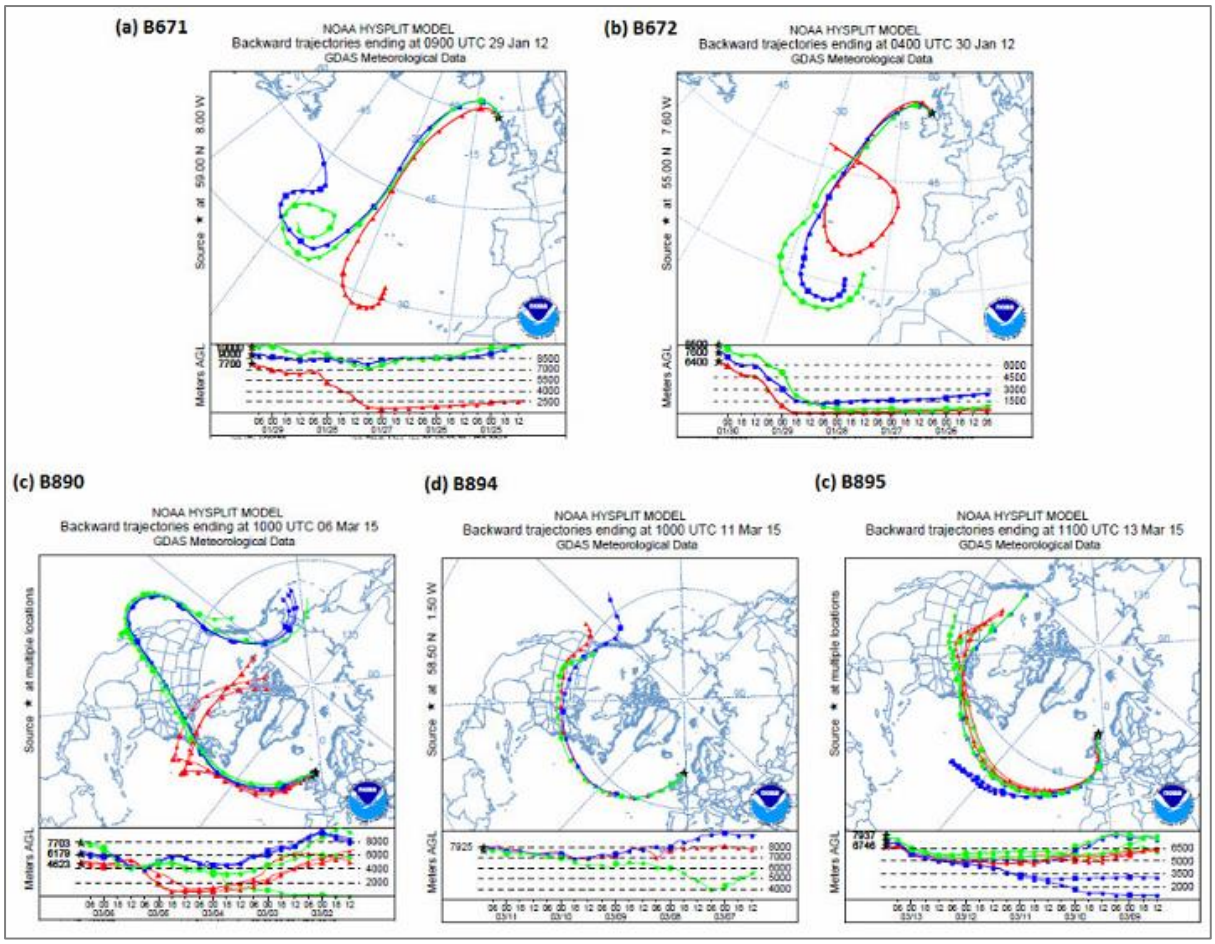

Figure 4.8: Five-day back trajectories of the air-mass probed during each of the five flight sections (B671, B672, B890, B894, B895). The red, blue, and green lines correspond to the air mass at different altitudes. Back trajectories were computed by the NOAA HYSPLIT model.

The 5-day back-trajectories show that the origins of the air mass which were measured during each flight section were similar for flights (i) B671(a) and B672(b), and for (ii) B890(c), B894(d), and B895(e). The origin was different between the two cases (i) and (ii). Whereas (i) had its origin over the North Atlantic, and travelled to where it was measured without passing over land, (ii) travelled over Canada and/or North America before passing over the North Atlantic and later being measured. Case (i) and (ii) also differed with regards to the ratio of lightly rough particles to moderately rough particles; there were many more lightly rough particles than moderately rough particles for case (i) (B671 and B672) than for case (ii) where the number of lightly rough particles were more similar to, or fewer than, the number of moderately rough particles (B890, B894, B895).

The origin of the air-mass may influence the concentrations of aerosol measured during the flight sections. This in turn can affect the ice nucleation: Ice formation that takes place heterogeneously on ice nuclei (IN) such as soot and mineral dust can generally do so at higher temperatures and lower relative humidity than if it were to form homogeneously (Krämer, et al., 2009). During homogeneous nucleation supercooled water will spontaneously freeze at colder temperatures. The type of nucleation can have a significant effect on the ice cloud: ice particles that form homogeneously do so in relatively high numbers, therefore there is more competition for water vapour to enable crystal growth, and the ice crystals may not grow as large or as rapidly as in the case of heterogeneous nucleation where fewer crystals tend to form (Spichtinger & Gierens (2009); DeMott & al., (1998); Haag & Kärcher (2004); Barahona, et al., (2010); Hoyle, et al., (2005)).

The Passive Cavity Aerosol Spectrometer Probe (PCASP) was mounted to the aircraft wing and used during all flights investigated here to determine aersol concentrations. Since a condition was set whereby only ice cloud measured at altitudes greater than 6km were analysed, the sample air flow rates were too slow for the PCASP to provide reliable measurements. Therefore aerosol measurements were unavailable for these flight sections.

As an alternative to aerosol measurements the particle size distributions (PSDs) averaged over each flight section were used to indicate potential homogeneous or heterogeneous nucleation as an alternative to IN measurements. The particle concentrations for each size bin were calculated from the SID-3 scattering patterns and then divided by the total time spent in-cloud during the flight section, in order to normalize the data since (a) not all flight sections were conducted entirely in-cloud, and (b) two of the flight sections had a shorter duration. The PSDs in Figure 4.9 and Figure 4.10 represent in-cloud sections only.

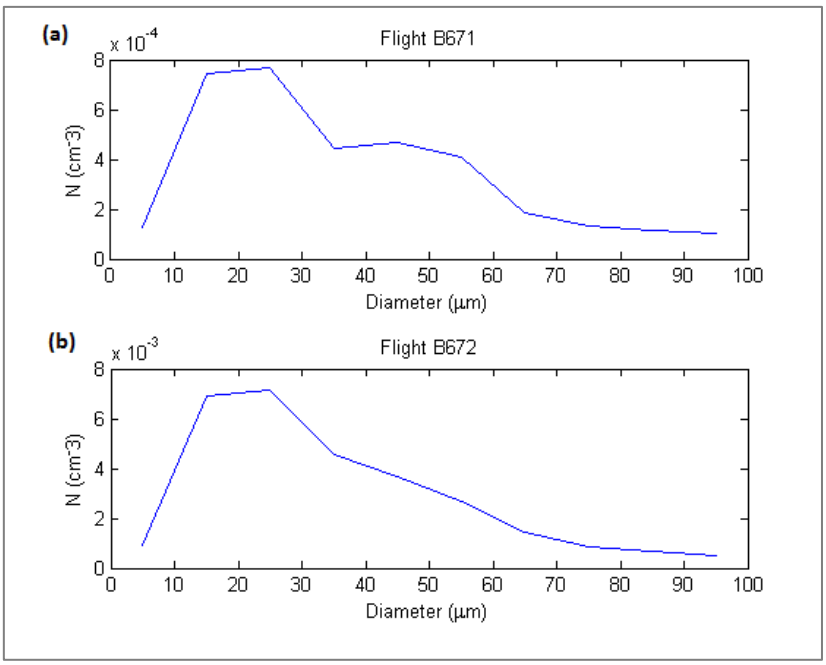

Figure 4.9: Particle size distributions averaged over the in-cloud sections defined in Section 4.1 from flights (a) B671, and (b) B672. The PSDs were calculated using the size measurements which were estimated from the SID-3 recorded scattering patterns.

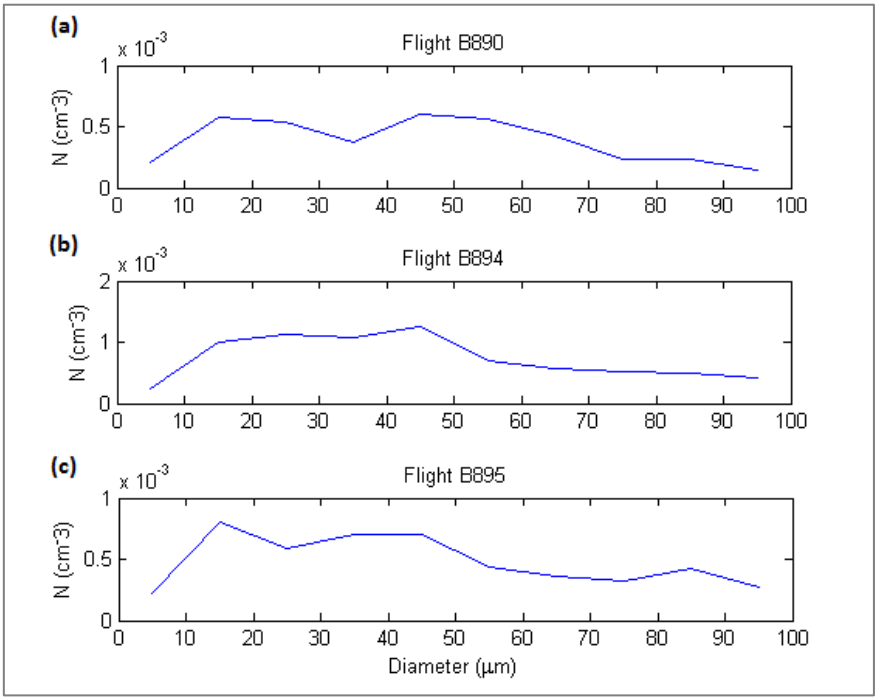

Figure 4.10: Particle size distributions averaged over the in-cloud sections defined in Section 4.1 from flights (a) B890, (b) B894, and (c) B895. The PSDs were calculated using the size measurements which were estimated from the SID-3 recorded scattering patterns.

The two flight sections with the oceanic origins (B671 and B672) showed the highest in-cloud particle concentrations of small particles relative to larger particles (Figure 4.9 (a) and (b)). The normalized concentrations at smaller diameters in the PSD for B672 were more than three times greater than for any other flight. The PSDs for B890, B894, and B895, flights which probed air of North American origin, (Figure 4.10(a), (b), (c)) are fairly consistent over all diameters. The skew of the PSDs observed from the oceanic air mass were 0.6 and 0.7; the skew of the PSDs observed from the North-American air mass were 0.3, 0.2 and -0.1. The more evenly distributed PSDs are more suggestive of heterogeneous nucleation since fewer crystals tend to nucleate simultaneously under this process and therefore due to a lack of competition for water vapour the crystals can grow at faster rates. The more positively skewed PSDs (B671 and B672) are more likely to be representative of homogeneous nucleation since a relatively high number of crystals will nucleate at one time and the high demand for water vapour in order for all of the crystals to grow may not be met which causes the crystals to remain relatively small.

The generally higher concentrations of smaller particles and the more positively skewed PSDs in combination with the ocean-only trajectory of the air-mass (fewer anthropogenic aerosols to act as IN) may suggest that the ice nucleation occurred homogeneously during the flight sections from B671 and B672. The opposite (fewer smaller particles, more evenly distributed PSDs, and continental air-mass origins) suggest that heterogeneous ice nucleation was likely during the sections of flights B890, B894, and B895. Therefore, since the ratio of lightly rough to moderately rough crystals is greater during flights B671 and B672 (ratios of 2.0 and 2.7 respectively) compared to flights B890, B894, and B895 (ratios of 0.6, 1.5, and 0.9 respectively) it is possible that the type of ice nucleation has had an impact on the particle roughness.

It may however be that the measurements taken during B890, B894 and B895 were conducted in older cloud and regions of nucleation were not probed. Therefore more evolved ice would have been measured which may have become larger and more complex. Flights have been investigated individually in greater detail to investigate potential links between roughness and atmospheric conditions in chapter 5 and 6.

4.3 Correlation with relative humidity and temperature

The particle roughness from the five flight sections was plotted against both relative humidity with respect to ice (RH_{ice}), and temperature in Figures 4.11 and 4.12 respectively. The temperature and roughness were also arranged into bins of width 1°C and the median values were calculated, as

shown in Figure 4.13. Neither plot showed a strong trend between roughness and RH_{ice}, temperature, or size; various degrees of roughness were observed over a range of temperatures and humidities. There are, however, no smooth particles observed at temperatures below -50°C, highlighting a potential (weak) trend.

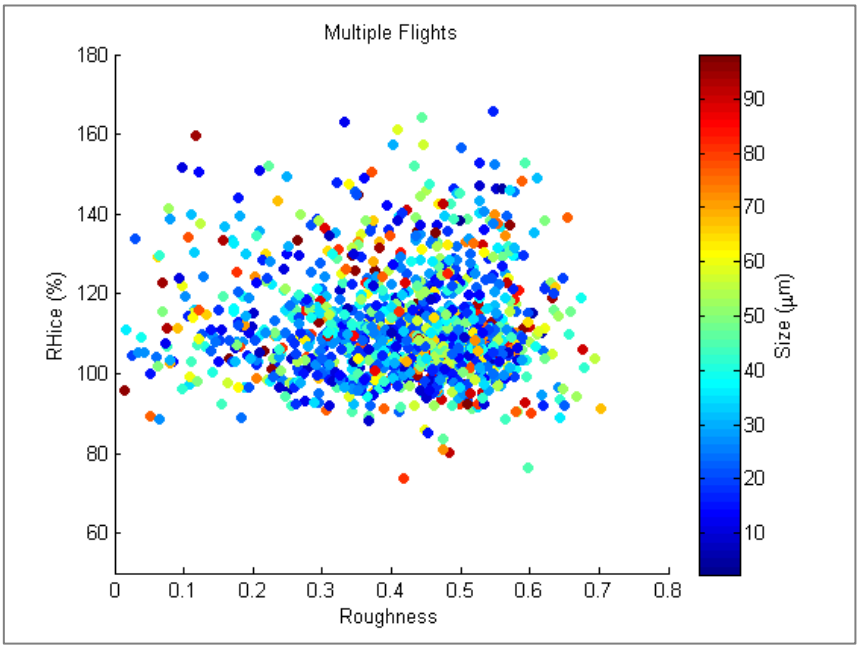

Figure 4.11: Relative humidity with respect to ice plotted against the particle roughness simultaneously observed during all five flight sections combined (B671, B672, B890. B894, B895). The data points have been shaded according to the size of the particle that they represent.

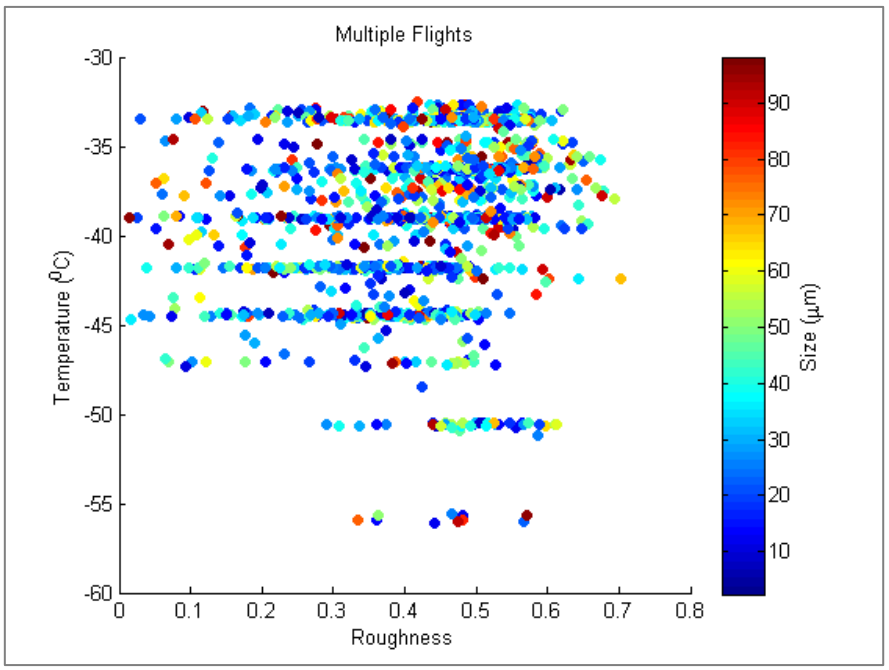

Figure 4.12: The measured temperature plotted against the particle roughness simultaneously observed during all five flight sections combined (B671, B672, B890. B894, B895). The data points have been shaded according to the size of the particle that they represent.

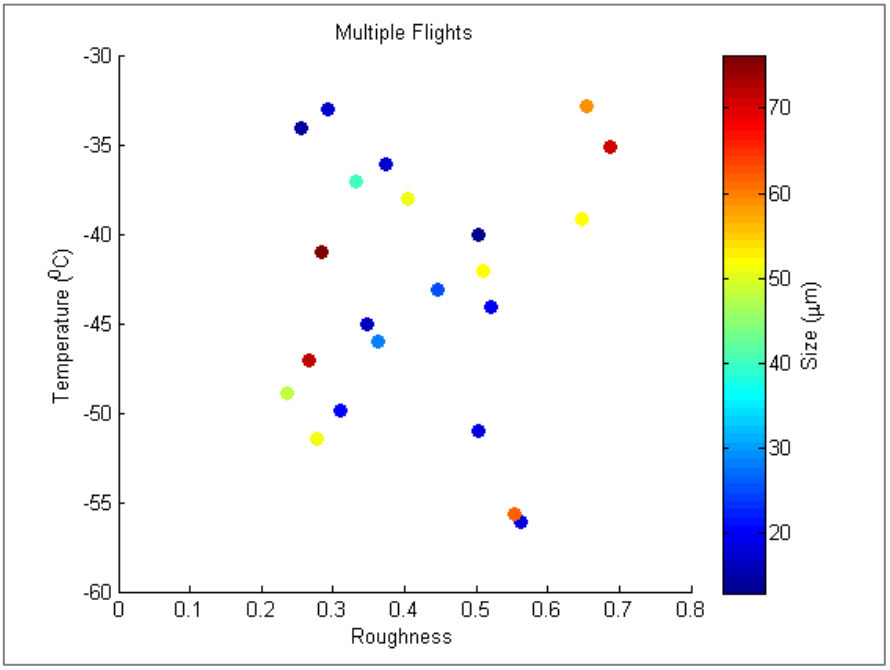

Figure 4.13: The median temperature plotted against the median observed particle roughness for all the five flight sections combined at each 1°C step. The data points have been shaded according to the median size of the particle observed in the corresponding temperature range.

The general lack of correlation is not entirely surprising due to the nature of the data collection: all of the measurements were instantaneous and therefore do not provide a history of the atmospheric conditions encountered by a particle before it is detected. It is not known in this case what the RH_{ice} and temperature were of the environment in which the ice crystals nucleated, and also what variations of these conditions the ice particle has encountered. Further information regarding an ice particle's point of nucleation and current stage of evolution is required for a link to be made between its roughness and the RH_{ice} and temperature. Flights have been investigated individually in greater detail to investigate potential links between roughness and atmospheric conditions in chapter 5 and 6. Both case studies are from flights which have been introduced in this chapter: chapter 5 addresses B672, a cirrus cloud study, whilst chapter 6 investigates B890, a wave cloud study.

5 *In Situ* Cirrus Case Study: B672

5.1 Flight Overview

Flight B672 was a cirrus flight which was executed as part of the UK Met Office PIKNMIX campaign out of Prestwick, Scotland, in January 2012. The flight path taken was a Lagrangian spiral descent through a thick layer of cloud (>5 km). This type of descent aimed to measure the evolution of ice crystals by probing them during a straight level run (SLR), and then profiling downwards to measure the same air parcels at a lower altitude after they had fallen under the influence of gravity. The profiles were spiral descents so that each SLR was conducted in roughly the same direction (northeast). The runs were started progressively further to the north-east such that the same air parcels were measured as the cloud moved due to a south-westerly wind. A simplified flight track has been plotted on a map in Figure 5.1 using the longitude and latitude measurements; the yellow corresponds to the profiles and the short runs which were used to get into position, whilst the other coloured lines represent a selection of SLRs from 4 to 22 (8.6 to 6km) to illustrate the nature of the measurements.

Figure 5.1: The flight track of the FAAM BAe 146 whilst performing a Langragian spiral descent throughout ice cloud just off the west coast of Scotland in January 2012. The yellow lines correspond to the aircraft profiling down and performing short runs in order to get into the desired position. The coloured lines represent the three minute runs of different altitudes which were designed to probe the same air mass as it fell under gravity.

The profiles of total water content (TWC) measured by the Nevzorov probe show similar characteristics throughout different altitudes, as illustrated in Figure 5.2. These are most

pronounced at lower altitudes (from run 18 to run 28) where the persistent peaks in TWC, at roughly the same points during each run relative to the cloud, suggest that the same fall streaks were measured at different altitudes. Therefore it is possible that the same air parcels were indeed measured at different altitudes as the ice crystals fell in the fallstreaks.

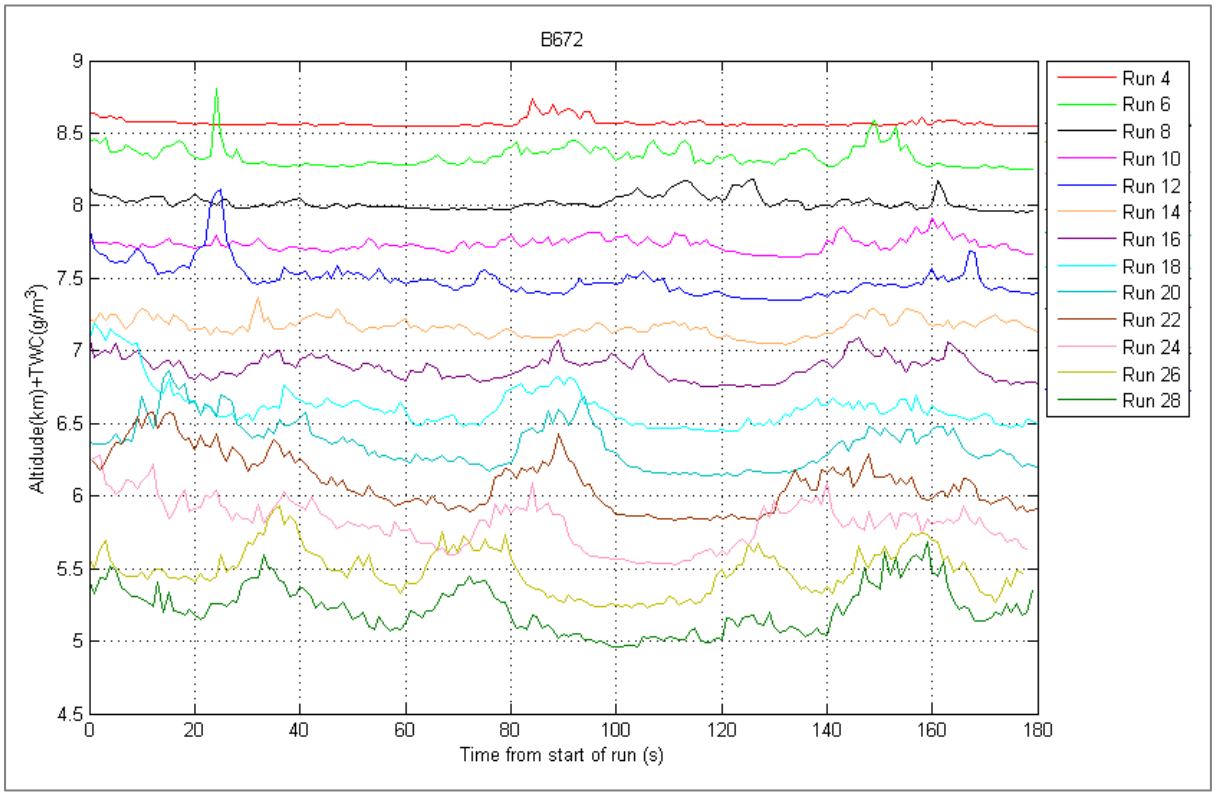

Figure 5.2: The total water content (TWC) across each straight level run (SLR) from 5.5km (run 4) to 4.8km (run 28) during B672 plotted against the time elapsed from the start of the SLR. The TWC (y-axis) has been added to the altitude of the corresponding SLR, which were roughly constant.

SLRs were conducted from 8.5km to 1.8km; SID-3 data was analysed from 8.5km down to 4.8km during which the aircraft was in-cloud, and a visual inspection of the SID-3 images indicated that the cloud consisted of ice between these altitudes. The size and roughness of individual ice particles were estimated from their scattering patterns using the methods described in Section 2.2.3.

5.2 Particle Size Distributions

From the size measurements, particle size distributions (PSDs) were calculated across different altitudes throughout the cloud, and were compared to those estimated by other cloud probes (SID-2, CDP, CIP15, CIP100, 2DC), a selection of which are shown in Figure 5.3. Each PSD in Figure 5.3 has

been averaged across an entire SLR (3 minutes), and the selection cover a range of altitudes (8.2km to 5.2km) and temperatures (-46°C to -21°C), both of which are roughly constant across each SLR.

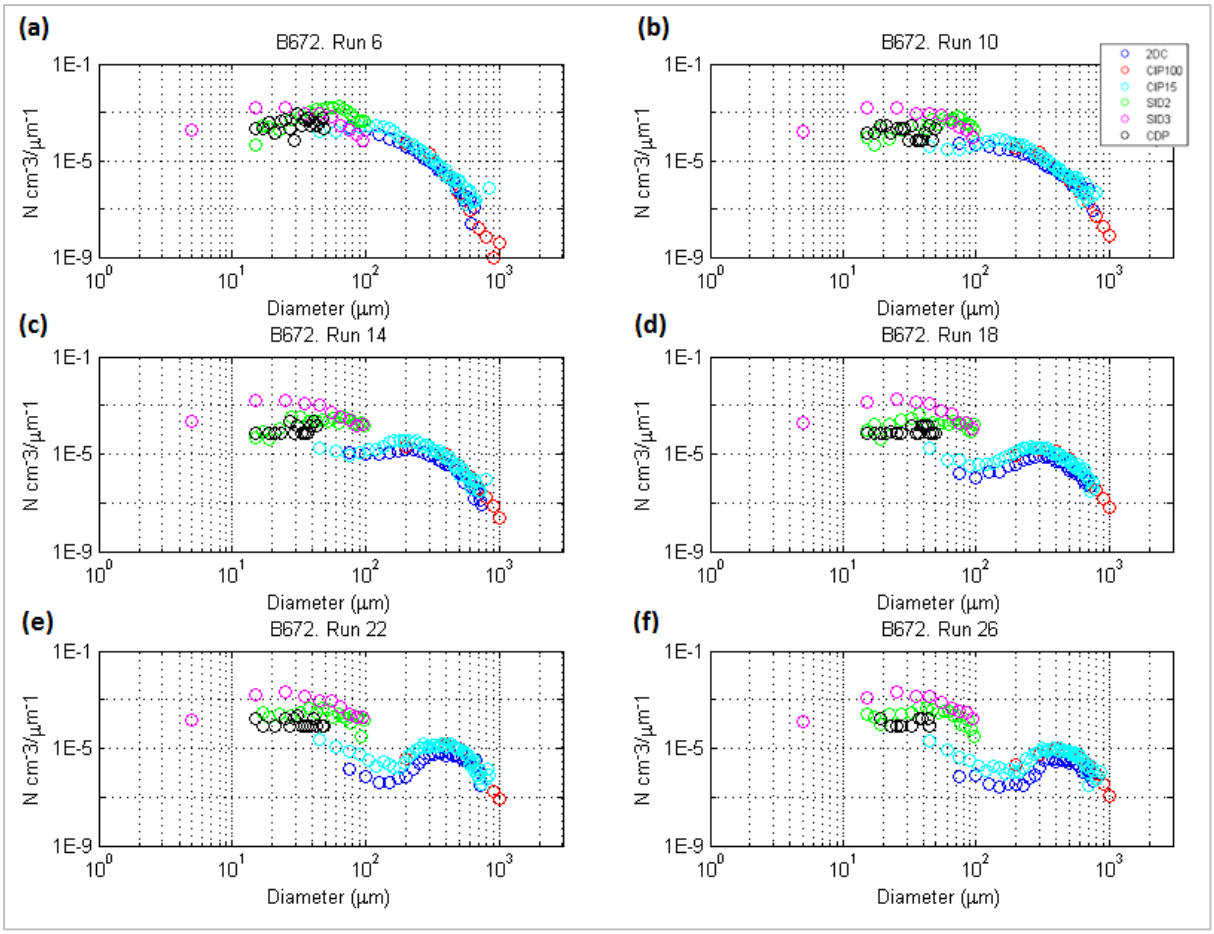

Figure 5.3: PSDs averaged over the length of 3 minute SLRs, executed over a range of altitudes and temperatures whilst in-cloud during flight B672. The magenta data points represent the PSDs estimated from the SID-3 scattering patterns. The black, green, light blue, dark blue, and red points represent the PSDs from CDP, SID-2, CIP15, 2DC, and the CIP100, respectively.

The method of determining size from SID-2 and CDP is different to that of SID-3: a Mie solution is fitted to the scattered light detected by CDP and SID-2, whereas the sizes from SID-3 data are derived from the scattering patterns, as described in section 2.2.3. Since the CDP and SID-2 methods use Mie solutions, all particles are assumed to be spherical, which can lead to the miss-sizing of nonspherical particles (Brenguier, et al., 2013). Not only are particles assumed to be spherical, but they are also assigned the same refractive index, which can also result in miss-sizing. Furthermore the relationship between particle size and the scattering cross section, which describes relative intensity of scattered light within the solid angle, and is a function of particle size, shape, and refractive index, is nonlinear (Brenguier, et al., 2013). Therefore particles of different sizes can have the same scattering cross section. The method of size retrieval from the SID-3 scattering patterns

does not require assumptions of crystal habit or refractive index and the scattering cross section is not used for size retrieval, however particles require a certain minimum degree of roughness to be sized correctly, section 3.2, which reduces the volume of size information of very smooth particles, as also illustrated in section 3.2. These variations in size determination may have led to slightly different concentrations at some diameters in the PSDs in Figure 5.3, however the PSDs are generally in good agreement considering the multiple uncertainties associated with cloud probes that use light-scattering techniques.

The main uncertainties include particle coincidence, ice particle shattering, counting uncertainties, and those associated with defining the sample volume (Brenguier, et al., 2013) (Cotton, et al., 2013) (Korolev, et al., 2011). Counting uncertainties are the consequence of poor sampling statistics, which can be an issue in the presence of very low concentrations. Uncertainties associated with coincidence, however, will be reduced in these cases. The issue associated with the greatest uncertainty is in defining the sample volume (Brenguier, et al., 2013). This is because the sample area is difficult to characterise: the instrument laser beam light intensity is not uniform, and the sample area is smaller for small particles which are likely to be measured in a limited fraction of the beam where the intensity is at maximum. It is also an issue at sizes approaching the upper size limit because the probability of particles crossing the beam edges increases. If most particles have diameters within the mid-region of the probes detection range then the uncertainty can be reduced to about 20% (Brenguier, et al., 2013). Uncertainties and limitations associated with light-scattering cloud probes are mentioned in more detail in section 2.1.1.

The composite PSDs in Figure 5.3 became bimodal with decreasing altitude; this distribution started to become visible in the PSD averaged over run 14(c) (7km, -35°C), and was enhanced as the SLR altitudes decreased. The change from a unimodal to a bimodal distribution is considered a consequence of aggregation (Cotton, et al., 2013); larger crystals becoming more common at these lower and warmer altitudes due to crystal aggregation as they fell through the cloud.

Aggregated crystals were present in the CPI (Cloud Particle Imager) images, and appeared to become more common with decreasing altitude. Examples of typical images at different altitudes are shown in Figure 5.4. Images taken towards cloud top where temperatures were colder than -40°C presented crystals with columnar features, with rosettes being prevalent, Figure 5.3(a,b). As temperatures increased over -40°C, but remained lower than -20°C, plate-like features became common, (c,d,e,f). These plate-like features grew on the originally columnar/rosette crystals as they precipitated from lower (<-40°C) to warmer temperatures (-40°C<T<-20°C), and are in agreement with the habit diagram created by Bailey and Hallett (2008).

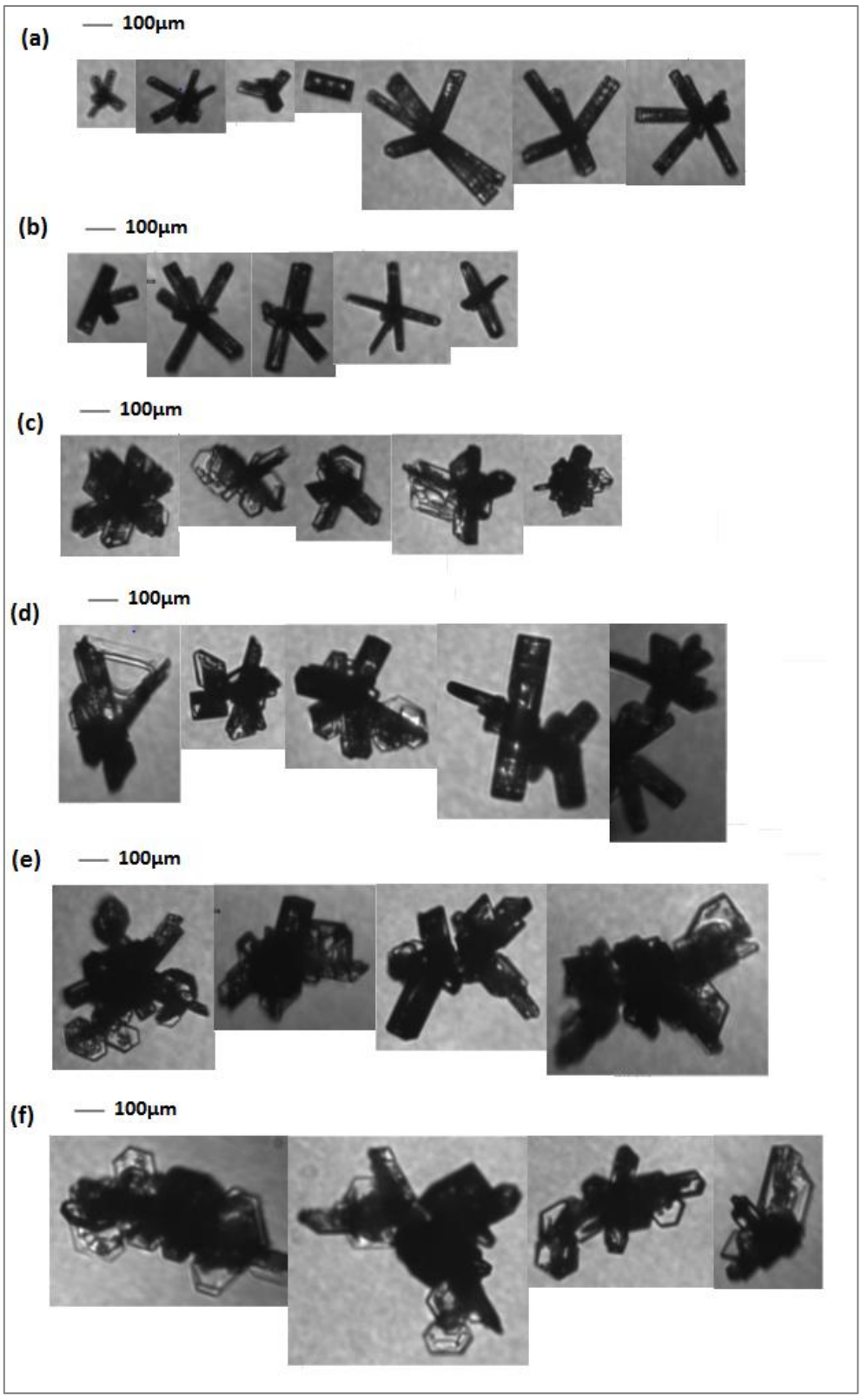

Figure 5.4: Ice particle images from the Cloud Particle Imager (CPI) during different SLRs in flight B672. Each row corresponds to a different SLR, descending in altitude and temperature from (a) to (f). The mean altitude and temperature for the corresponding SLR are (a) 8.2km, -46°C; (b) 7.6km, -40°C; (c) 7.0km, -35°C; (d) 6.5km, -29°; (e) 5.8km, -25°C; (f) 5.2km, -21°C. Columnar features dominate at the colder temperatures and higher altitudes, whilst plate-like features and irregularity become more apparent towards warmer temperatures and lower altitudes.

5.3 Particle Roughness

The roughness of particles were estimated from the degree of speckle present in their scattering patterns. Histograms were plotted which showed the percentage of particles with various levels of surface roughness/complexity in Figure 5.5. The roughness values were from the same particles whose sizes were used to estimate the PSDs in Figure 5.3.

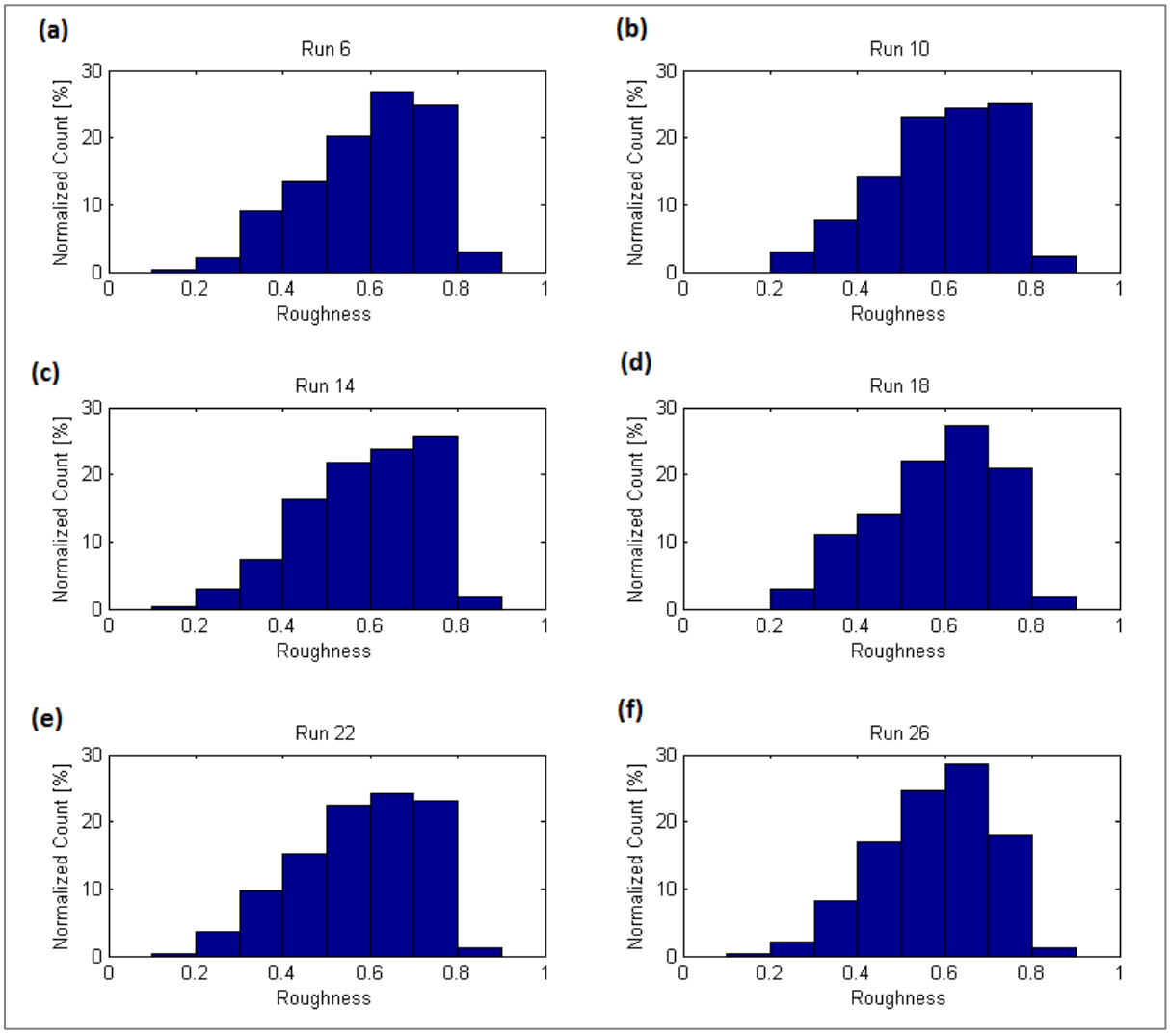

Figure 5.5: The percentage of particles with certain degrees of roughness observed over six different 3 minute SLRs during flight B672. The altitude consistently decreases from plot (a) to plot (f), and is held roughly constant for each SLR. Moderately rough particles tend to dominate across all altitudes.

Throughout all runs represented in Figure 5.5, which covered altitudes from 8.2km(a) down to 5.2km(f), the particle roughness distributions were very similar: smooth particles (0 to 0.25) were

uncommon at all altitudes, and the percentage of particles became progressively greater as the degree of roughness increased, up until the severely rough regime (~0.8) at which point particles once again became uncommon. The most prevalent particle roughness over all altitudes was moderately rough. The fewer numbers of smooth ice crystals relative to rough ice crystals could provide an explanation as to the rarity of halos. It has been seen in previous studies that the phase function of rough crystals are smoothed out and do not have peaks at the 22° and 46° angles, those at which scattering occurs when halos are observed (Yang & Liou, 1998; Liou, Takano, & Yang (1999); Ulanowski, 2005). The *in situ* measurements presented here suggest that rough crystals were much more numerous than smooth crystals (which were relatively rare), and therefore pronounced scattering by ice crystals at a 22° or 46° angle is not common.

The consistently high percentages of lightly to moderately rough crystals throughout the depth of the cloud illustrated that particle roughness can be maintained, however the low numbers of severely roughened crystals suggest that roughness may not be significantly enhanced. It is important to note, however, that these *in situ* measurements were instantaneous and did not necessarily provide information about the crystal origin.

The relative humidity with respect to ice, RH_{ice}, can provide an indication of the stage of evolution of the ice, i.e. nucleation, growth, sublimation etc. If the RH_{ice} is high, then ice is likely to be nucleating (or recently nucleated), homogeneously at higher values and heterogeneously at relatively lower supersaturation. As the ice grows, water vapour is depleted and the RH_{ice} in these circumstances will be approaching saturation (RH_{ice}≈100%). Below saturation much of the excess water vapour will have been used in particle growth and therefore particles can start to dissipate possibly through sublimation. Based on this generalised relationship between ice crystal regime and relative humidity, the roughness values of ice were sorted: roughness observed during periods of potential growth, and those observed during periods of potential nucleation were extracted and compared. Data collected during times of possible sublimation were not used due to low numbers of data. The periods of each regime during SLRs 4 to 28 are illustrated in Figure 5.6; the TWC was plotted against time from the start of the run, and coloured depending on the RH_{ice} estimated from WVSS2 data. The RH_{ice} values were used to define supersaturated, saturated, and subsaturated environnments, which were in turn associated with the different stages of crystal evolution. Supersaturated regions (black) were defined as periods where RH_{ice} was greater than 110%, saturated regions were between 105% and 95%, and subsaturated regions, which were not analysed due to too few data points, were defined as RH_{ice} lower than 95%. In the plot (Figure 5.6) gaps are present in the measurements as a consequence of defining the upper limit of saturation 5% lower than the lower limit of

supersaturation. This was applied to reduce any overlap of regime related to the relative humidity. For a full representation of the TWC during the SLRs from 4 to 28 refer to Figure 5.2.

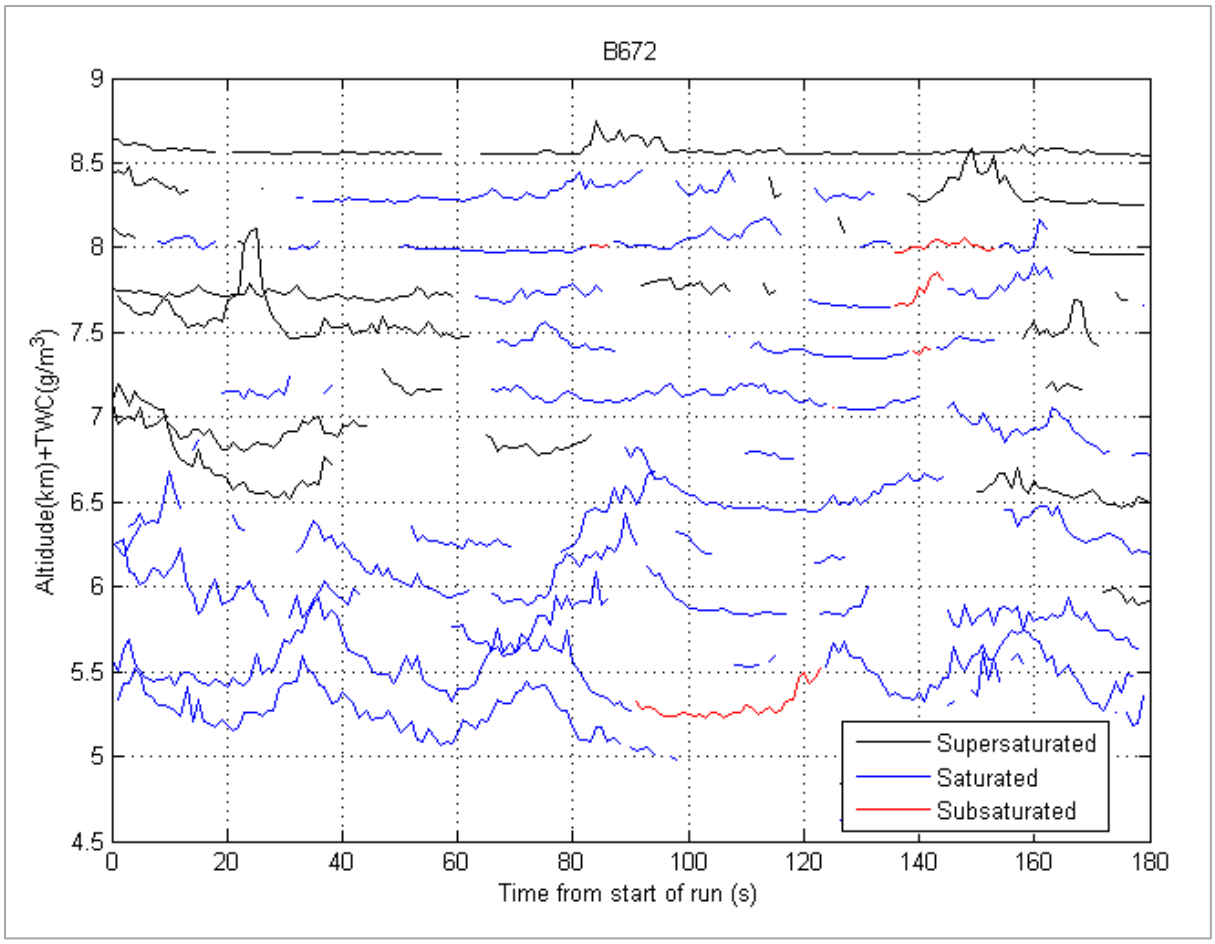

Figure 5.6: TWC measured by the Nevzorov across SLRs during flight B672 plotted against the time elapsed from the start of each SLR. The colours of the lines are dependent on whether the environment was supersaturated (RH_{ice} >110%) (black line), saturated (105%<RH_{ice}<95%) (blue line), or subsaturated (RH_{ice}<95%) (red line). The gaps in data are a consequence of the 5% gap between the limits in RH_{ice} for supersaturation and saturation.

Any recently nucleated crystals were expected to be observed in the supersaturated environments (shown in black on Figure 5.6) whereas crystals that were older and had experienced growth processes were expected in the saturated regions (blue line sections). Data from SLRs 6, 10, and 12 were selected to represent the supersaturated region because the RH_{ice} during these runs reached values at which nucleation could occur (125% to 135%), as shown in Figure 5.7(a). In contrast the RH_{ice} values measured during SLRs 24, 26, and 28 did not reach values at which nucleation is expected, Figure 5.7(b), and therefore it was unlikely that ice measured along these SLRs had been

recently nucleated. The relative humidity was high enough to enable nucleation for almost half of the sample period during SLR 4, and this run has been analysed individually.

The PSDs of ice for the two environments, supersaturated and saturated, are illustrated in Figure 5.8. The PSD of ice observed in supersaturated environments (a) was unimodal while the PSDs over saturated regions (b) were bimodal with the second peak at diameters around 500µm, suggestive of aggregation. In the supersaturated case the peak at the smaller diameters occurs between 10µm and 20µm in the SID-3 data and falls off much quicker than the peak in the saturated case which was broader and was shifted towards 20µm to 30µm.

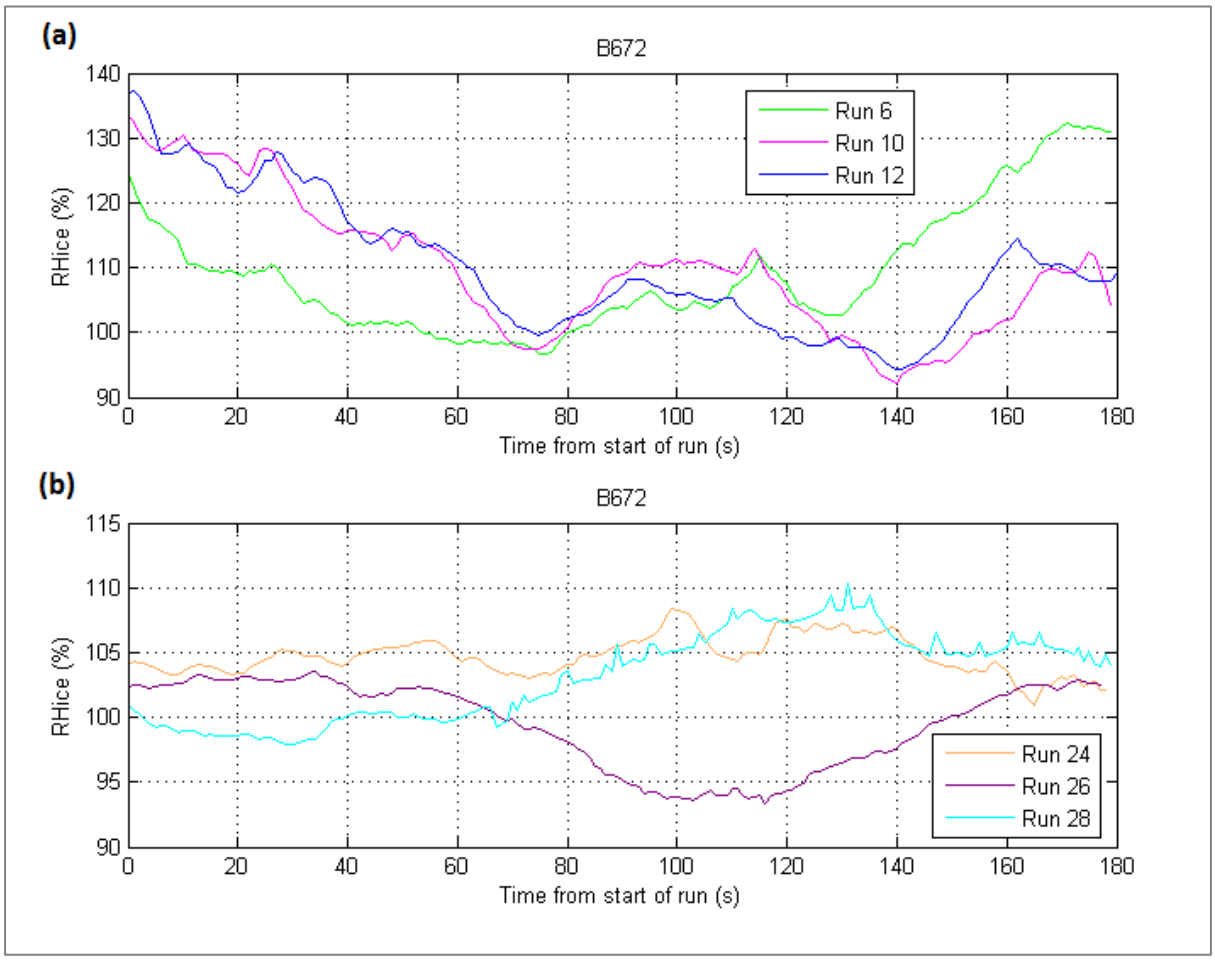

Figure 5.7: The observed relative humidity with respect to ice plotted against the time elapsed from the start of each SLR. In (a) RHice values are high enough that nucleation may be expected (higher altitude runs with higher observed relative humidity have been plotted); in (b) RHice values ae consisitently below nucleation thresholds (lower altitude runs with lower observed relative humidity have been plotted).

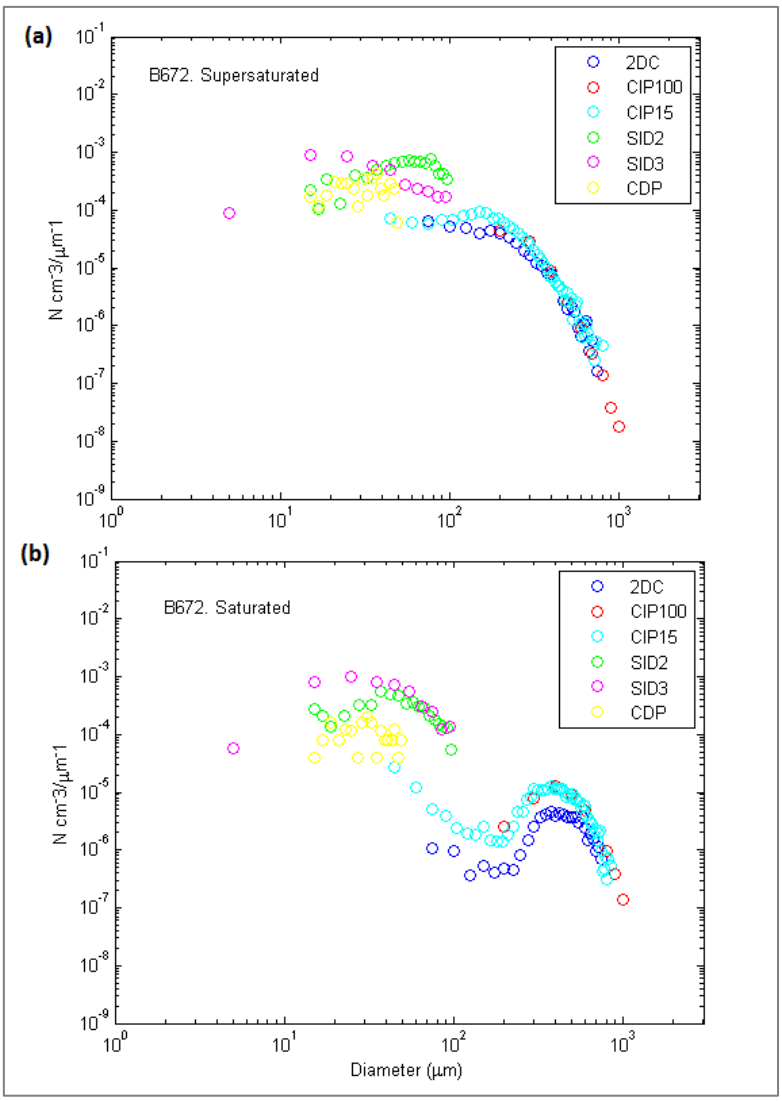

Figure 5.8: Particle size distributions estimated from data recorded whilst in (a) supersaturated in-cloud regions; (b) saturated in-cloud regions. The PSD with magenta data points was estimated from the size measurements that had been derived from the SID-3 recorded scattering patterns of ice crystals. PSDs from other cloud instruments have also been plotted (2DC (dark blue); CIP100 (red); CIP15 (cyan); SID2 (green); CDP (yellow)). The integrated PSD is unimodal in supersaturated regions, and becomes bi-modal in substaturated regions with a second peak at larger diameters of around 150µm.

The roughness values of particles observed in the selected supersaturated and saturated regions are shown in Figure 5.9. There were similar percentages of smooth particles measured in the supersaturated (light blue) and the saturated (dark blue) environments. The percentages of particles then increase with roughness for both environments, up to where they both peak between 0.6 and 0.7, i.e. moderately rough. For the roughness values leading up to the peak, and at the peak, i.e. lightly rough to moderately rough, the percentage of particles observed was greater for the

saturated case than for the supersaturated case. When the roughness values reached 0.7 there was a shift in the relative percentages and greater numbers of the rougher particles were observed in supersaturated conditions.

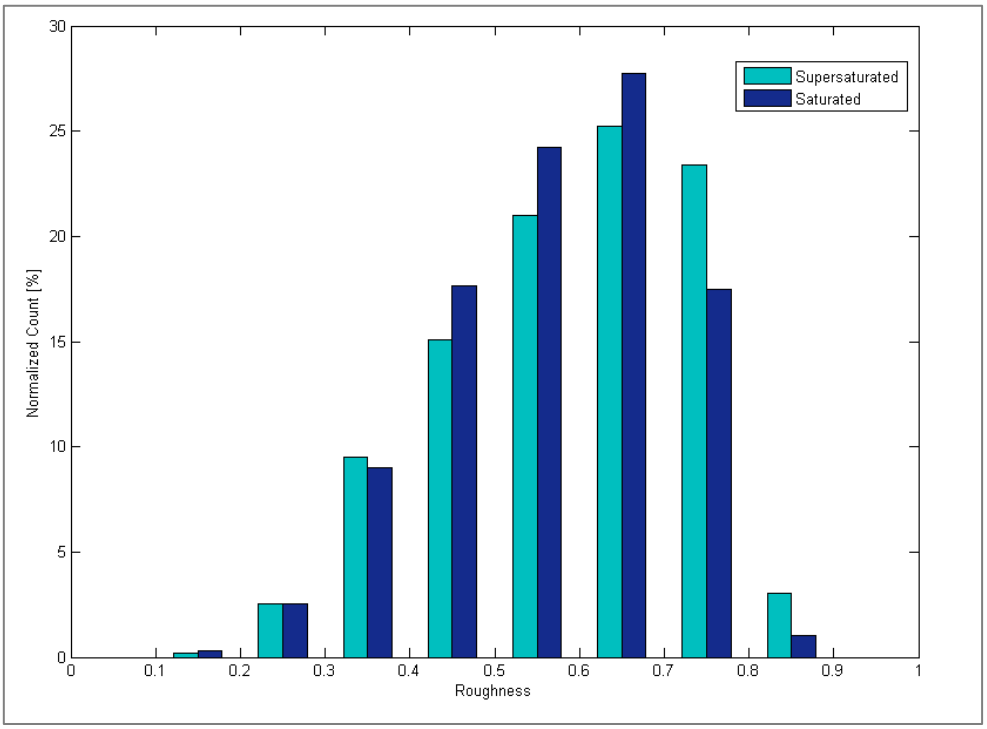

Figure 5.9: The percentages of particles which were observed with various degrees of roughness in supersaturated regions (light blue) and saturated regions (dark blue) during a selection of SLRs from flight B672. The roughness values were estimated from the SID-3 recorded scattering patterns.

A T-test was used to estimate the statistical significance of the trend seen in Figure 5.9; rougher particles are more common in supersaturated regions than in subsaturated regions. The T-test here was used to determine whether the difference between the two roughness distributions (in supersaturated, and in subsaturated environments) is not a chance finding. Measurements of the differences in the distribution were required across the roughness values, i.e. at 'smooth' values as well as 'rough' values; therefore a two-tailed T-test was applied. The t-value was calculated using Equation 5.1, and the degree of freedom using equation 5.2, both of which are required to assess the statistical significance of the difference between the two distributions.

$$t = \frac{\mu_{sup} - \mu_{sub}}{\sqrt{\frac{\sigma_{sup}^2}{n_{sup}} + \frac{\sigma_{sub}^2}{n_{sub}}}} \qquad [5.1]$$

$$d.f = (n_{sup} + n_{sub}) - 1 \quad [5.2]$$

Where t is the t-value, μ is the mean value, σ^2 is the variance, n is the sample size, d.f. is the degrees of freedom, and the subscripts 'sup' and 'sub' correspond to the roughness distributions measured in supersaturated and in subsaturated environments, respectively.

For the two distributions shown in Figure 5.9, the t-score was 3.640 and the degree of freedom was 1711. These values yielded a p-value of 0.000281 suggesting that the difference between the two distributions was significant. Therefore particles with a higher roughness value were more likely to be observed in supersaturated environments.

The SLR executed at the highest altitude within the cloud, SLR 4, was investigated separately because throughout half of the SLR duration the RH_{ice} was above 120%, and for around a third of the run the RH_{ice} was greater than 130%, as illustrated in Figure 5.10. If ice was present in these conditions it was likely that it had recently nucleated, and that the cloud instruments were probing nucleation regions. The PSD across the run (Figure 5.11) was suggestive of this since it was unimodal with a peak at the smaller diameters; at around 15μm in the SID-3 data.

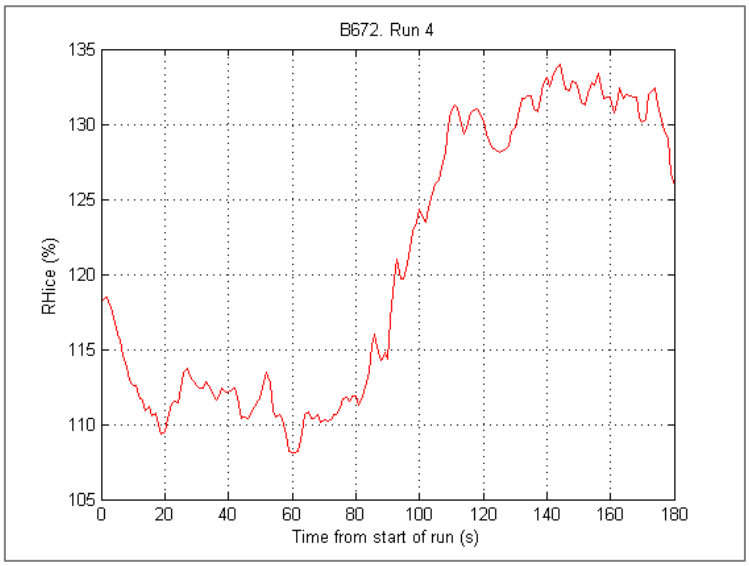

Figure 5.10: The relative humidity with respect to ice plotted against the time elapsed since the start of SLR 4,which was the highest altitude in-cloud run that was executed during B672. The RH_{ice} remains above saturation for the entirety of the run, and increases to very high supersaturation (130%) at around 110s from the start of the run.

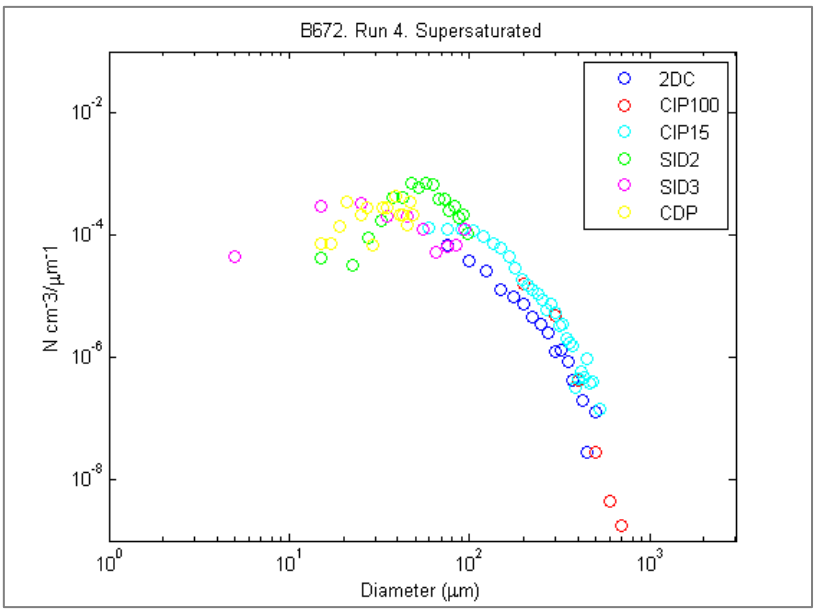

Figure 5.11: PSDs averaged over the period of SLR 4, during which the environment was consistently supersaturated. The magenta data points represent the PSDs estimated from the SID-3 scattering patterns. The black, green, light blue, dark blue, and red points represent the PSDs from CDP, SID-2, CIP15, 2DC, and the CIP100, respectively.

Similarly to the lower level SLRs presented in Figures 5.7 to 5.9, the ice crystal roughness values were sorted depending on the RH_{ice} measurement during which they were observed. The RH_{ice} did not drop below 105% during this SLR, and therefore the ice measurements were divided based on the extent of supersaturation; $110\% \leq RH_{ice} < 130\%$, and $RH_{ice} \geq 130\%$. The two groups of particle roughness measurements are shown in Figure 5.12, the dark blue bars represent roughness values observed in lower supersaturation, and the light blue bars correspond to particle roughness measured when the supersaturation was more extreme. The roughness distributions were similar in both cases; both increased progressively from 0.2 to 0.8 after which the distribution decreased rapidly. Smooth particles and severely rough particles were relatively rare during both periods, and moderately rough was the most common degree of roughness. There is no clear difference between the two distributions.

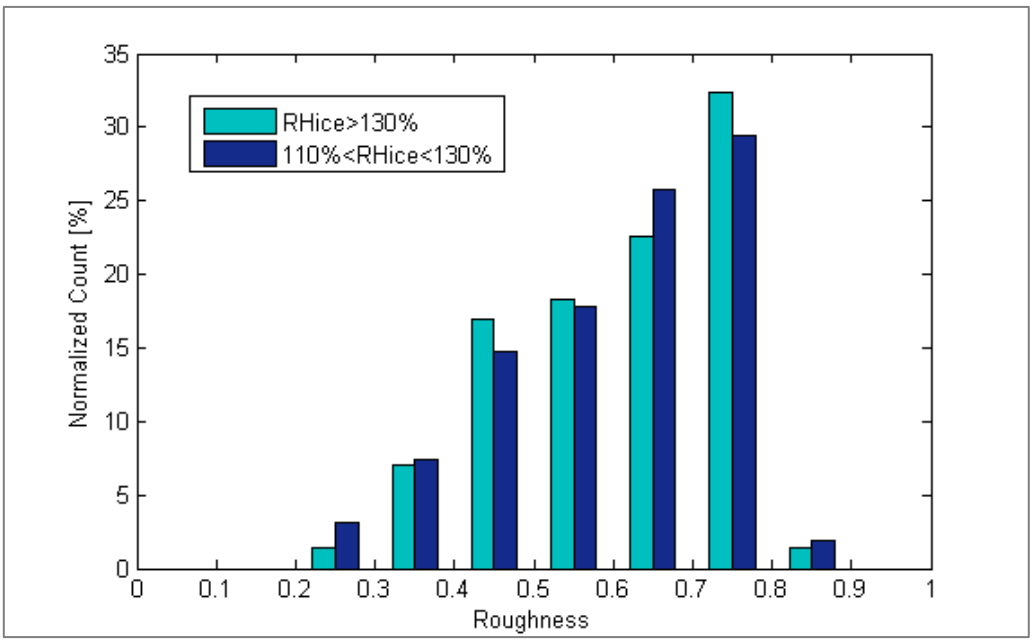

Figure 5.12: The particle roughness measurements estimated from SID-3 scattering patterns of particles which were detected in two different supersaturated regions during SLR 4. The light blue bars represent measurements which were conducted when the RH_{ice} was greater or equal to 130% and the dark blue lines represent measurements taken when the RH_{ice} was between 110% and 130%.

5.4 Conclusions

A cirrus cloud flight was conducted out of Prestwick, Scotland, in January 2012. The flight path taken was a Lagrangian spiral descent through a thick layer of cloud (>5 km). The type of descent aimed to measure the evolution of ice crystals by probing them during a straight level run (SLR), and then profiling downwards to measure the same air parcels at a lower altitude after they had fallen under gravity. The profiles of total water content (TWC) measured by the Nevzorov probe showed similar characteristics throughout different altitudes. These were most pronounced at lower altitudes where the persistent peaks in TWC, at roughly the same points during each run, relative to the cloud, suggested that the same fall streaks were measured at different altitudes. Therefore it is possible that the same air parcels were indeed measured at different altitudes as the ice crystals fell in the fallstreaks.

Crystal images from the CPI showed columnar features (mainly rosettes) at T<-40°C; crystals gained planar features as they precipitated down to altitudes at warmer temperatures (-40°C<T<-20°C). Aggregates were observed in the images and became more common with decreasing altitude. This was also seen in the composite PSDs which became bimodal, with the second peak appearing towards the larger diameters around 400µm.

Across all straight level runs throughout the depth of the cloud the most common roughness type was ‘moderate’; smooth and severely rough particles were rare. The particle roughness observed in supersaturated regions during SLRs 6, 10, and 12, and saturated regions during SLRs 24, 26, and 28 were compared. The peaks in both distributions were at the same degree of roughness (0.6 to 0.7), and the distributions were similar. There were more rougher particles (0.7 to 0.8) observed during supersaturated conditions and a two-tailed t-test was applied and showed that this was statistically significant. Therefore particles with higher degrees of roughness were more likely to be observed in supersaturated environments.

Particle roughness was maintained throughout the depth of the cloud. Although the RH_{ice} measurements can give an indication of the evolution stage in which the crystal occurred at the time of detection, the measurements were instantaneous and the history of the crystal was therefore not known. Subsequently the roughness of crystals when they have just nucleated was not known. A more reliable estimate of the roughness of particles which have recently nucleated can be provided by measurements in wave-cloud: since they have sharp leading edges the distance from the edge can act as a proxy for the time elapsed since nucleation. Furthermore, aggregation in wave clouds is theoretically negligible; therefore measurements of roughness should indicate single-particle surface roughness and complexity. A wave cloud case study has been presented in the next chapter.

6 *In Situ* Lee Wave Case Study: B890

There is not currently a method in place to discriminate between small-scale surface roughness and large-scale complexity from the SID-3 scattering patterns of particles; this includes complexity caused as a result of crystal aggregation. Aggregation is likely, and expected, in many cirrus cases as crystals grow and fall under gravity. In order to investigate how the surface roughness and shape of individual crystals differ under different atmospheric conditions, i.e. due to growth and sublimation (indicated by the relative humidity), wave cloud can provide a useful study since aggregation in these types of cloud is negligible.

6.1 Wave Cloud Concept

Theoretically a wave cloud occurs between the maximum and minimum of the vertical wind velocity, where the temperatures are below the mean value, Figure 6.1. The airflow through these clouds is typically laminar so an ice crystal's position in the cloud (relative to the cloud leading edge) can act as a proxy for the time elapsed since ice nucleation occurred. When an ice crystal is nucleated, it will travel along a streamline in the cloud, and since mixing between streamlines is negligible, the crystals detected can be assumed to have not become aggregated (Figure 6.2). Therefore, any roughness/complexity detected at the starting edge of the cloud is likely to have occurred at the time of ice crystal nucleation.

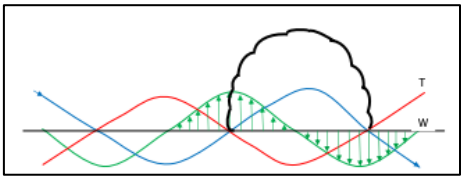

Figure 6.1: The theoretical location of wave cloud formation in the presence of atmospheric gravity waves; the cloud forms between the maximum upward velocity and the maximum downward velocity. The red line represents the temperature T, the green line is the vertical component of wind W, and the blue line is the parcel streamline (Cui, et al., 2012).

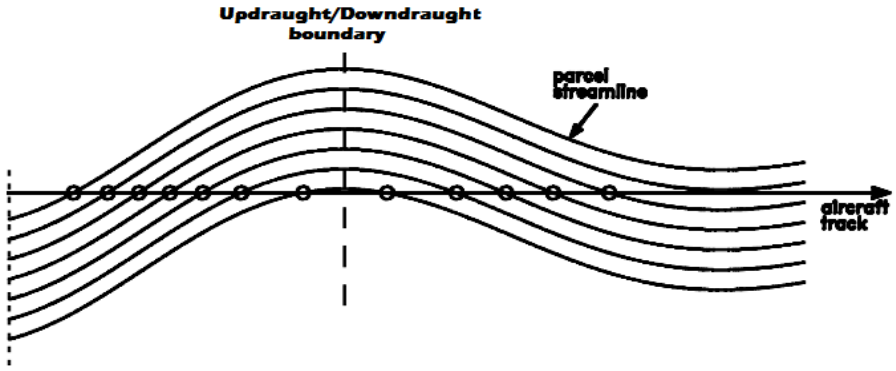

Figure 6.2: Schematic of how ice crystals and/or droplets move in a wave cloud from the updraught region to the downdraught region. The updraught-downdraught boundary corresponds to the point of the AGW where vertical velocity is zero (Cotton & Field, 2002). The particles follow the streamline and mixing between streamlines is negligible.

In a chain of mountain wave clouds, however, all clouds except the first to nucleate may not have formed in clear air since ice crystals from previously formed clouds are spread out by horizontal winds. The crystals, however, will still follow a laminar flow, and roughness/complexity due to aggregation will be negligible. This type of cloud could therefore provide an interesting insight into particle roughness estimated from the SID-3 2D scattering patterns, since aggregation, which is common in most cirrus, especially with decreasing altitude, can be assumed not to be the cause of high degrees of observed speckle in the scattering patterns. Rather, the roughness will be a consequence of atmospheric conditions at the time of nucleation, or due to growth and sublimation, potentially in cycles as a consequence of the cyclic nature of the vertical wind velocity.

6.2 B890 Flight Overview

Flight B890 was part of the COSMICS/CIRCCREX campaign out of Prestwick, Scotland, in March 2015. The flight took advantage of strong south-westerly winds over the Scottish Highlands which caused lee-waves as a consequence of air passing over the mountainous region. The flight was designed as a wind investigation as opposed to cloud, and so it was not an ideal wave cloud case study. It was chosen, in spite of this, as a case study because it was the first, and currently only, example of a wave cloud research flight during which SID-3 collected data. As a consequence the data presented in this chapter may be used to demonstrate the necessity for future wave-cloud flights in ice particle roughness research.

Seven straight level runs (SLRs) were executed at a range of altitudes between two fixed points relative to the ground, B and C in Figure 6.3(a), during which cloud was observed. The formation of these clouds was suspected to be a consequence of atmospheric gravity waves, i.e. lee waves. Six SLRs were made consecutively with decreasing altitude from 7.7km down to 1.7km. The aircraft then climbed up to 9.2km and a seventh SLR was performed between point B and C (Figure 6.3a).

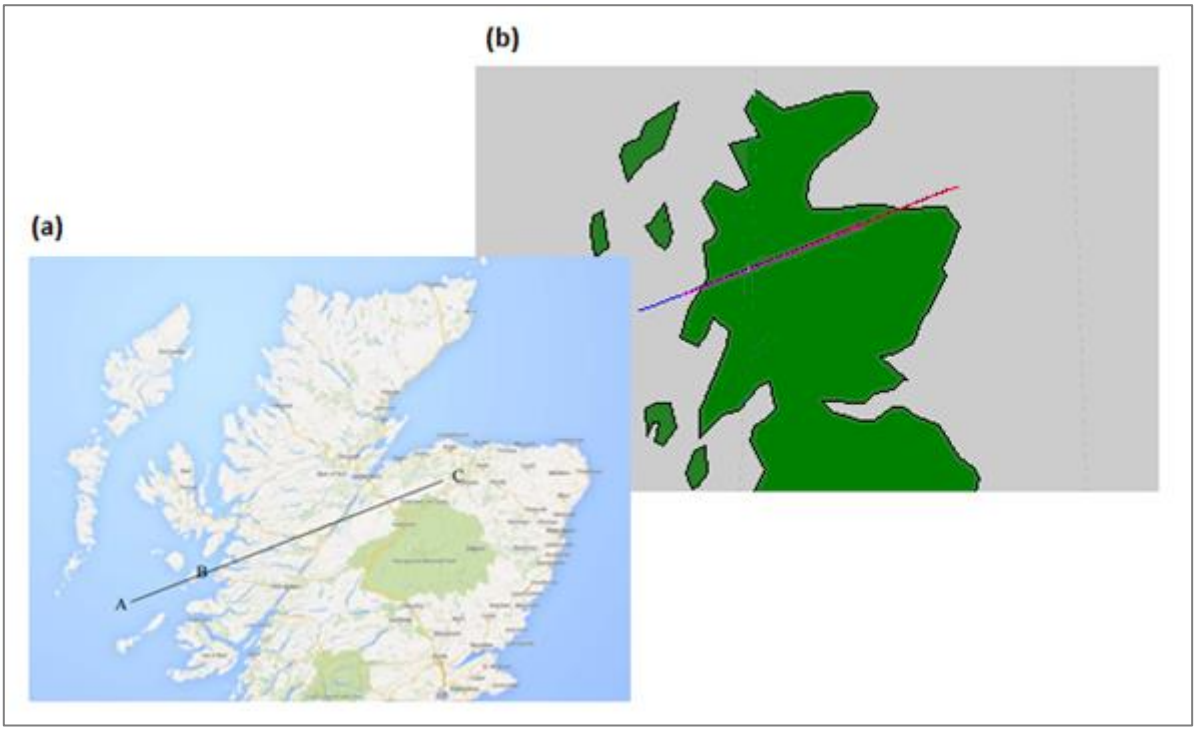

Figure 6.3: Area of operation during flight B890. Seven straight level runs were conducted at different altitudes between point B and point C. The planned track of the runs is shown in (a); the plot in (b) shows the location of runs from aircraft data. The white dotted line in plot (b) is part of a longitude line

6.3 Wave Cloud Identification

The cyclic variation in the vertical component of the wind velocity given by the AIMMS probe can be seen in Figure 6.4 for the seven SLRs conducted between points B and C. The latitude and longitude during the run were used to find the distance from a reference point (point B in Figure 6.3a) at each second of the run. These were plotted against the sum of the altitude and the vertical wind velocity each second (Figure 6.4) and illustrated the presence of AGWs which decreased in amplitude as they propagated upwards and their energy dissipated. The altitude of each run was kept constant, and was represented by the dashed lines in Figure 6.4 which also indicate where the vertical wind velocity was zero, i.e. the updraught-downdraught boundary.

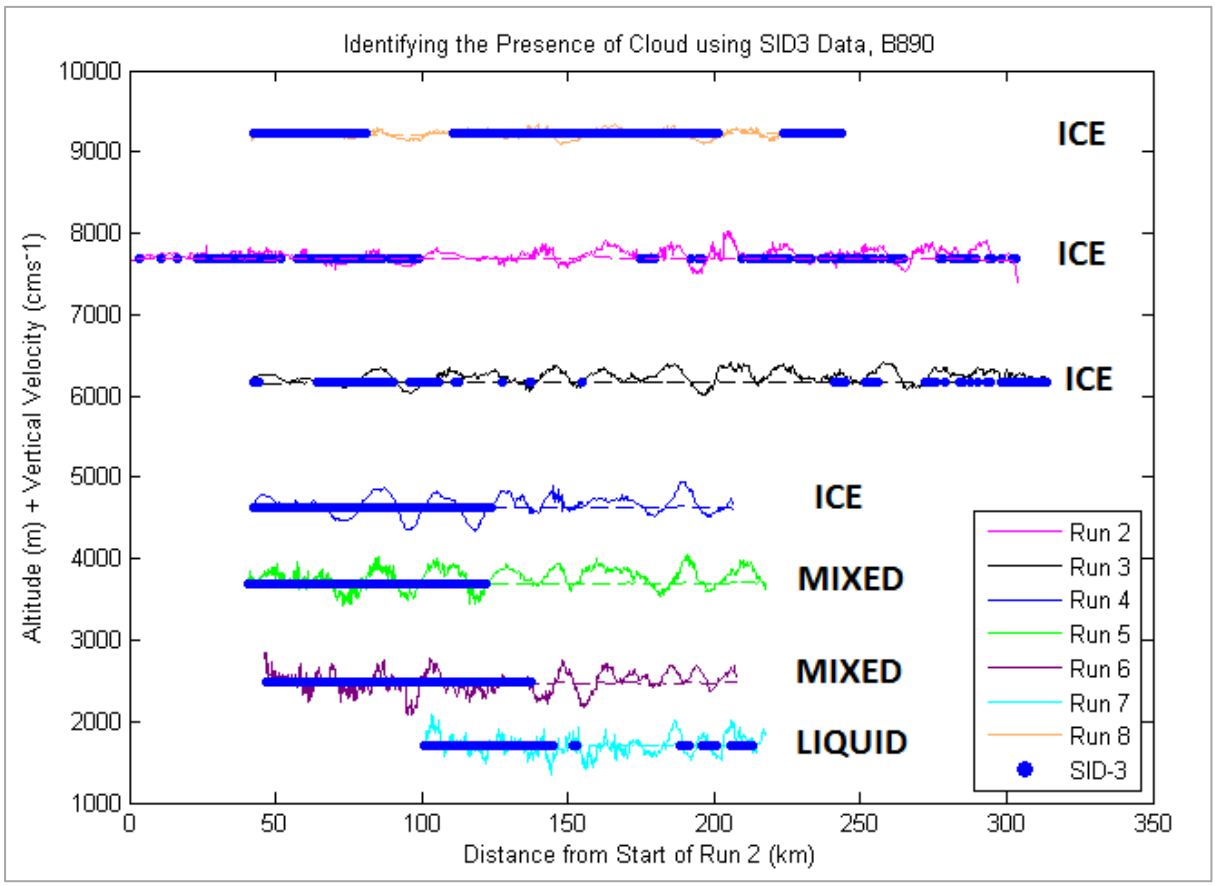

Figure 6.4: Seven straight level runs during B890. The altitude of the measurement was added onto the observed vertical wind velocity and plotted against the distance from a fixed reference point (point B on Figure 6.3(a)). The dashed lines are the measured altitude only against the distance, and correspond to a vertical wind velocity of zero. The blue dots correspond to where SID-3 detected ice or liquid water. The phase of the cloud obserbed during each of the SLRs is shown to the right of the corresponding plot, ICE denotes ice-cloud, MIXED represents mixed-phase (ice and liquid water), and LIQUID corresponds to a liquid-only part of the cloud; the top of the cloud was ice-only and gradually becomes mixed phase, and then liquid-only.

The SID-3 data were plotted over the wind data in Figure 6.4 to determine the distances relative to the fixed reference point at which the aircraft was in-cloud, for each run. The scattering images were inspected visually to determine the phase of the cloud at each altitude: ice-only (ICE) was observed during runs 2, 3, 4, and 8 (9.2km to 4.6km); liquid was observed with ice (MIXED) in runs 5 and 6 (3.7km to 2.5km); and liquid-only (LIQUID) was present during run 7 (1.7km). Runs 6 and 7 were rejected from further analysis due to the high concentrations of liquid water. Run 5 also contained liquid water; however, the concentrations were relatively low (≈1% of scattering patterns). Runs 2 to 5 were the focus of further investigation because not only did they contain all or mostly ice, they also showed fairly strong wave-like signatures with regards to cyclic variations in vertical wind velocity, which became less significant during run 8 (9.2km).

In-cloud sections with well-defined peaks and troughs in vertical velocity were chosen to confirm that the variations in vertical velocity were associated with AGWs, and the cloud is therefore a wave cloud. This confirmation was achieved by comparing the vertical wind velocity with the temperature since a signature of AGWs is a 90° phase shift between the two variables. Sections were picked out to include a peak and a trough in the vertical wind so that half the wavelength could be determined by subtracting the distance at which the peak occurred from that at which the trough occurred. This half-wavelength was then divided by two to determine the distance corresponding to a 90° phase shift of the wave. The vertical wind was plotted against the distance, and the temperature was over-plotted against the original distance plus the distance that corresponded to the phase shift, in Figure 6.5. The plots show the occurrence of a 90° phase shift between temperature and the vertical wind velocity, and therefore the cloud was most likely formed as a consequence of atmospheric gravity waves created by the disturbance of air as it passed over the mountainous regions in the west of the Scottish Highlands.

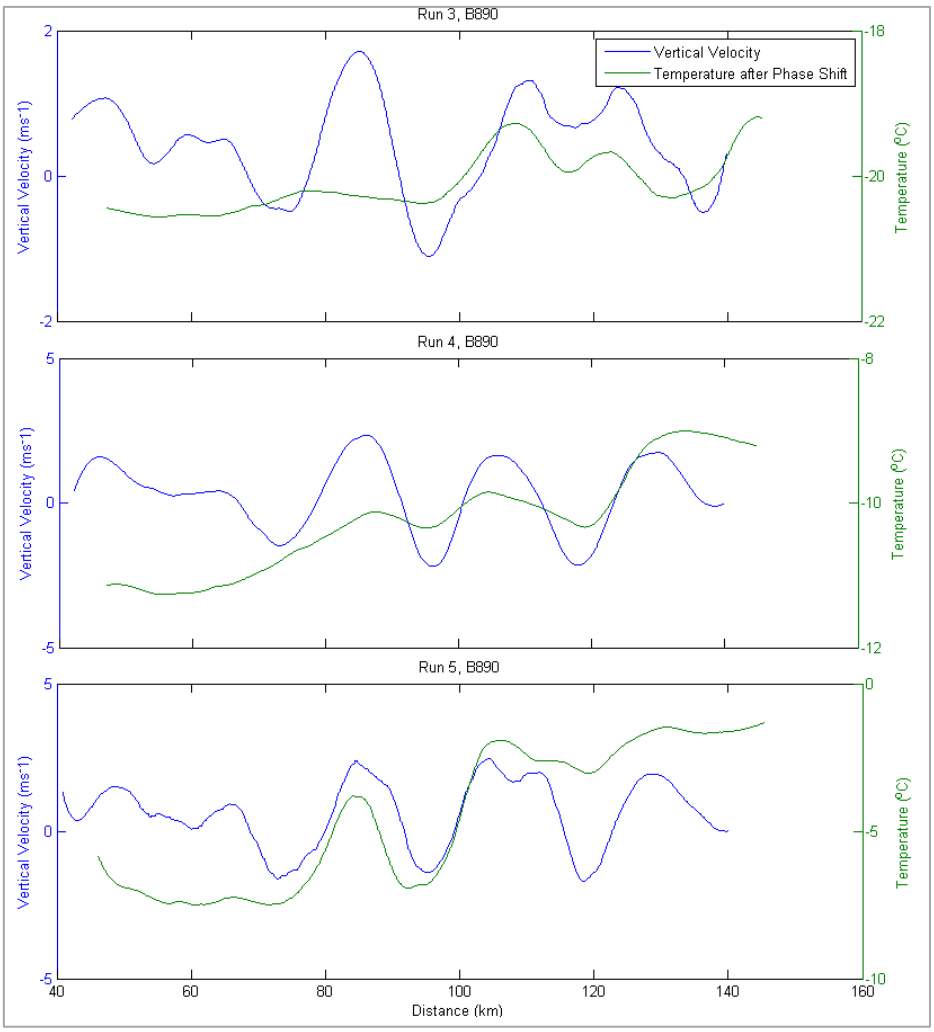

Figure 6.5: Vertical wind velocity (blue) plotted against distance from the reference point (point B in Figure 6.3(a)) for in-cloud sections during three straight level runs. Temperature has been plotted against the distance from the reference point with a 90° phase shift of the wave (green).

During most runs the cloud appears to have formed before first detection and has begun to spread downwind, i.e. the theoretical model for which wave cloud is formed and confined in the crest of the wave is not representative of this case. It is not clear from most of these runs at which point in reference to the AGW the cloud began to nucleate. Run 2, however, was the first to be performed in-cloud between points B and C (Figure 6.3a) and so the cloud detected during this run appears to hold a structure most consistent with the theoretical model introduced in Figure 6.1. It also had less time to spread as a consequence of horizontal winds, and started closer to the upwind reference point than any other run.

At around 24km (from the ref. point; start of run 2; point B in Figure 6.3(a)), there are sudden increases in total water content (TWC) measured by the Nevzorov probe, the ice crystal

concentration measured by SID-3, and the aerosol concentration measured by PCASP, Figure 6.6. It was difficult to say at which point along the wave this formation occurred since there appeared to be multiple waves with short periods which were superimposed on to the longer more persistent wave. When the wind data was smoothed to remove the waves with shorter periods, the formation point of the cloud lay between the peak and the next trough of a wave, as theoretically dictated. Figure 6.6 shows the smoothed wind data plotted over the TWC (Nevzorov), ice concentration (SID-3), and the aerosol concentration (PCASP); the purple box shows where the first increase in concentration and TWC occurred. The ice particle concentrations (SID-3) were consistent after this point, but the aerosol concentrations reduced rapidly suggesting that the nucleation region was at the sharp edge (24km). The particle concentrations and the TWC diminish at 50km around the time the next wave peak was reached. Shortly after this peak, and once again between peak and trough, a significant increase was observed in particle concentration, aerosol concentration and TWC (orange box) which diminished after around 30km due to the cloud spreading and dissipating. Since significant peaks in aerosol concentration were coincident with increases in both ice crystal concentration and TWC, they may be indicative of ice nuclei (IN) and therefore nucleation events. It is likely that these IN were enabling heterogeneous nucleation given that the relative humidity with respect to ice (RH_{ice}) was below the homogeneous threshold, and the mean temperature during the run only reached down to -34.4°C. Figure 6.7 shows the RH_{ice} and temperature during run 2.

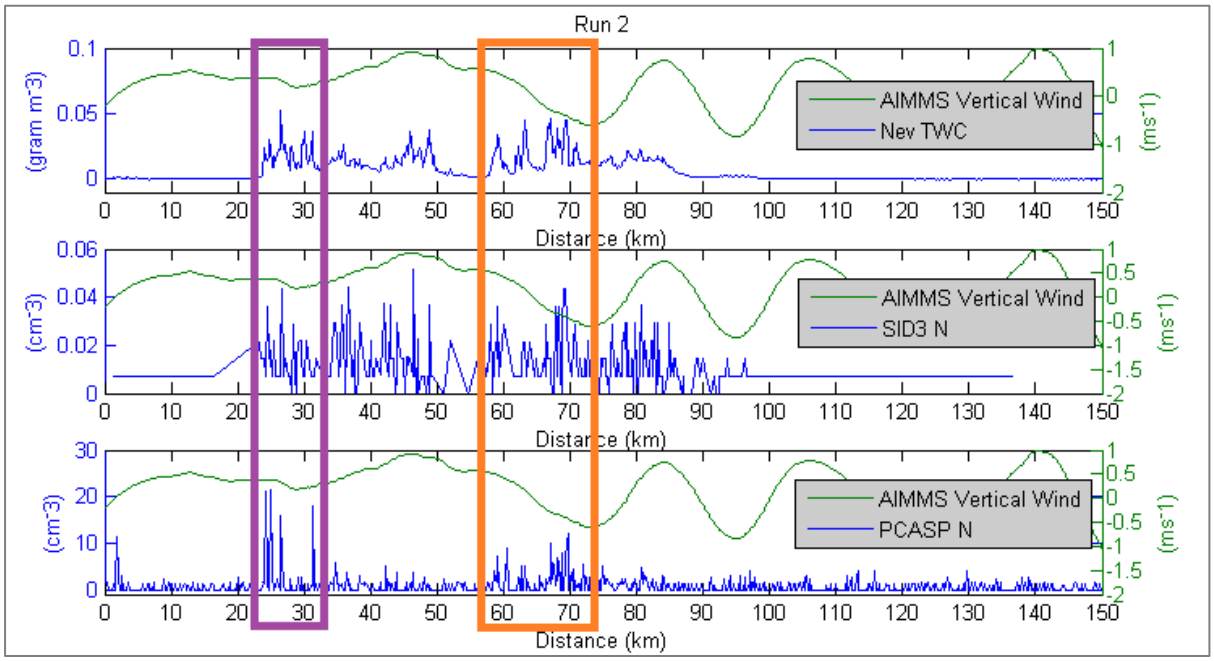

Figure 6.6: The vertical component of wind during run 2, which was smoothed in order to represent the most dominant AGW period, and plotted with (a) TWC, (b) ice crystal concentrations and (c) aerosol concentrations (0.3 to 0.8µm), all plotted as a function distance from the reference point (point B in Figure 6.3(a)). The coloured boxes highlight potential isolated wave clouds, detected before the horizontal wind caused the clouds to merge and/or dissipate.

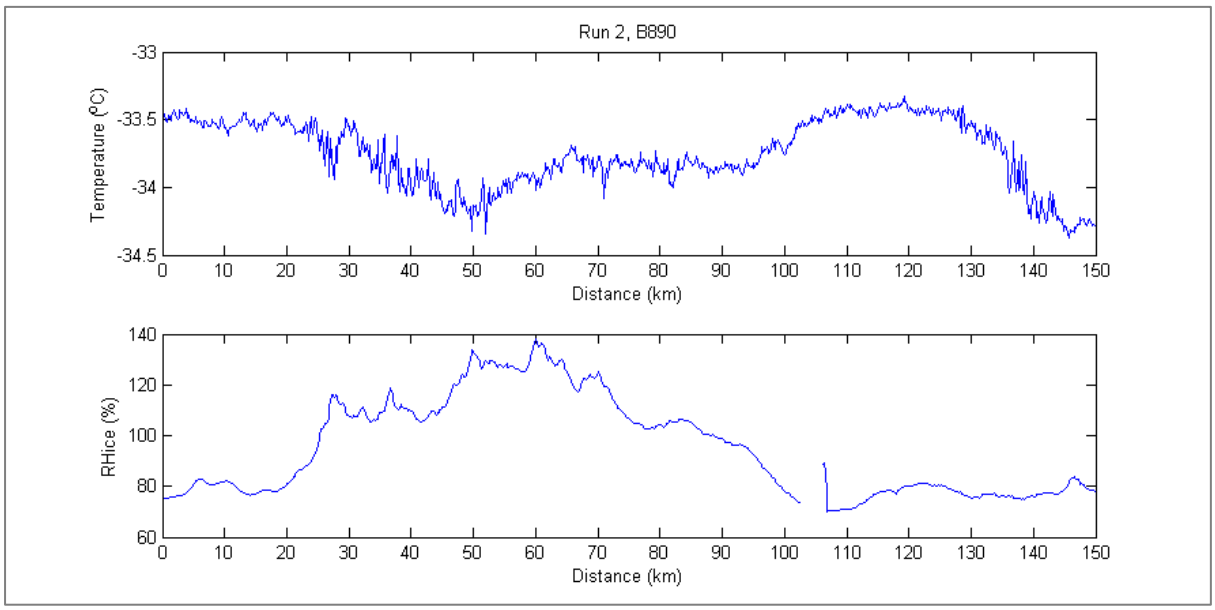

Figure 6.7: Temperature and relative humidity with respect to ice during SLR 2 as a function of distance from the reference point. The temperature is coldest (-34.4°C) whist the aircraft is in-cloud. Supersaturation occurs at the points where nucleation is suspected, and reduces to below saturation in the clear-air downwind of the wave cloud.

Since heterogeneous nucleation was suspected in the coldest part of the cloud (during run 2), it follows that any nucleation events in the lower altitude runs were also the consequence of heterogeneous nucleation and not homogeneous nucleation. Similarly to run 2, significant peaks occurred in aerosol concentration throughout the suspected formation region of the cloud, and became fewer and smaller with increasing distance downwind. The lack of isolated and relatively large peaks in ice particle concentration, however, suggest that by the time the runs were started the cloud had already formed, and had started to spread away from its nucleation point, and dissipate (Figure 6.8). The gradual reduction in both TWC and particle concentrations indicate this dissipation, possibly via sublimation since the air becomes dry at this point (well below saturation).

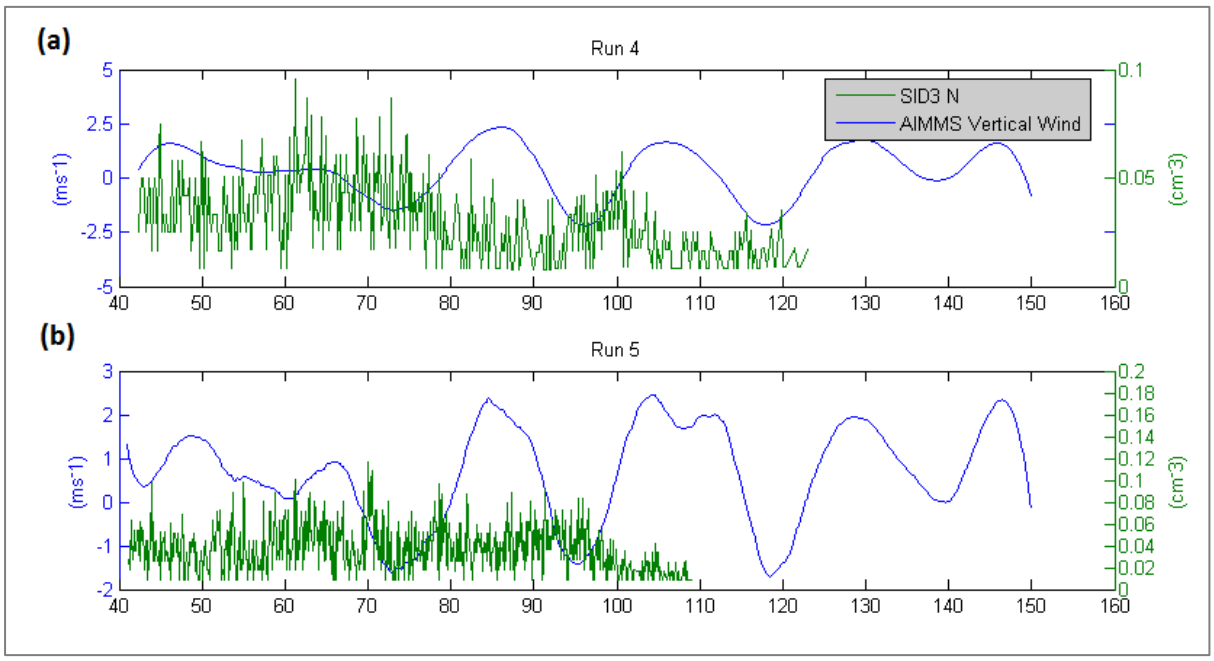

Figure 6.8: Particle concentrations (green) calculated from SID-3 data plotted against distance from the reference point during, (a) SLR 4, (b) SLR 5 of B890. Overplotted is the vertical wind velocity over ecah SLR against the distance from the reference point. The concentrations were more consistent than those that were observed over SLR 2, suggesting that there was a lack of isolated wave clouds forming in clear air, but rather cloud that had spread by horizontal winds and/or cloud that had formed due to regrowth of potentially sublimating particles.

6.4 Selecting SID-3 Data

The sizes of individual particles were retrieved from the scattering patterns captured by SID-3 during B890 when the minimum mean brightness was set to 32, and also when it was set to 64. In the previous chapter the lower minimum brightness setting (32) was used and particles with estimated diameters greater than 100µm were rejected (as outlined in section 3.3). The sections of cloud that were used to determine this criterion were cold (<-35°C) and dominated by small ice (≤100µm) so using the lower brightness enabled the smaller ice to be included in the analysis. In the case of B890, however, the cloud becomes significantly warmer (-5°C during run 5) and mixed phase as illustrated in Figure 6.4. The very small particles (≤15µm) were therefore not expected to be as influential as in the colder cases (i.e. B672 where temperatures reached -50°C), and mid-sized particles (around 50µm) and larger particles (≥100µm) were expected to be more common during this flight. Furthermore, coincidence becomes more probable in warmer mixed-phase clouds as concentrations increase. This can manifest in scattering patterns similar to those shown in Figure 6.9, where a large portion of the image is black. If the minimum mean brightness required of an image is low (32) then the possibility of these coincidences being included in analysis is increased. To identify the optimum

brightness requirement for these data the PSDs were calculated, and compared, from the size retrieved from the scattering patterns when the minimum brightness was set to 32, and when it was set to 64. Figure 6.10 shows the two SID-3 PSDs plotted with the PSDs that were calculated from 2DS data.

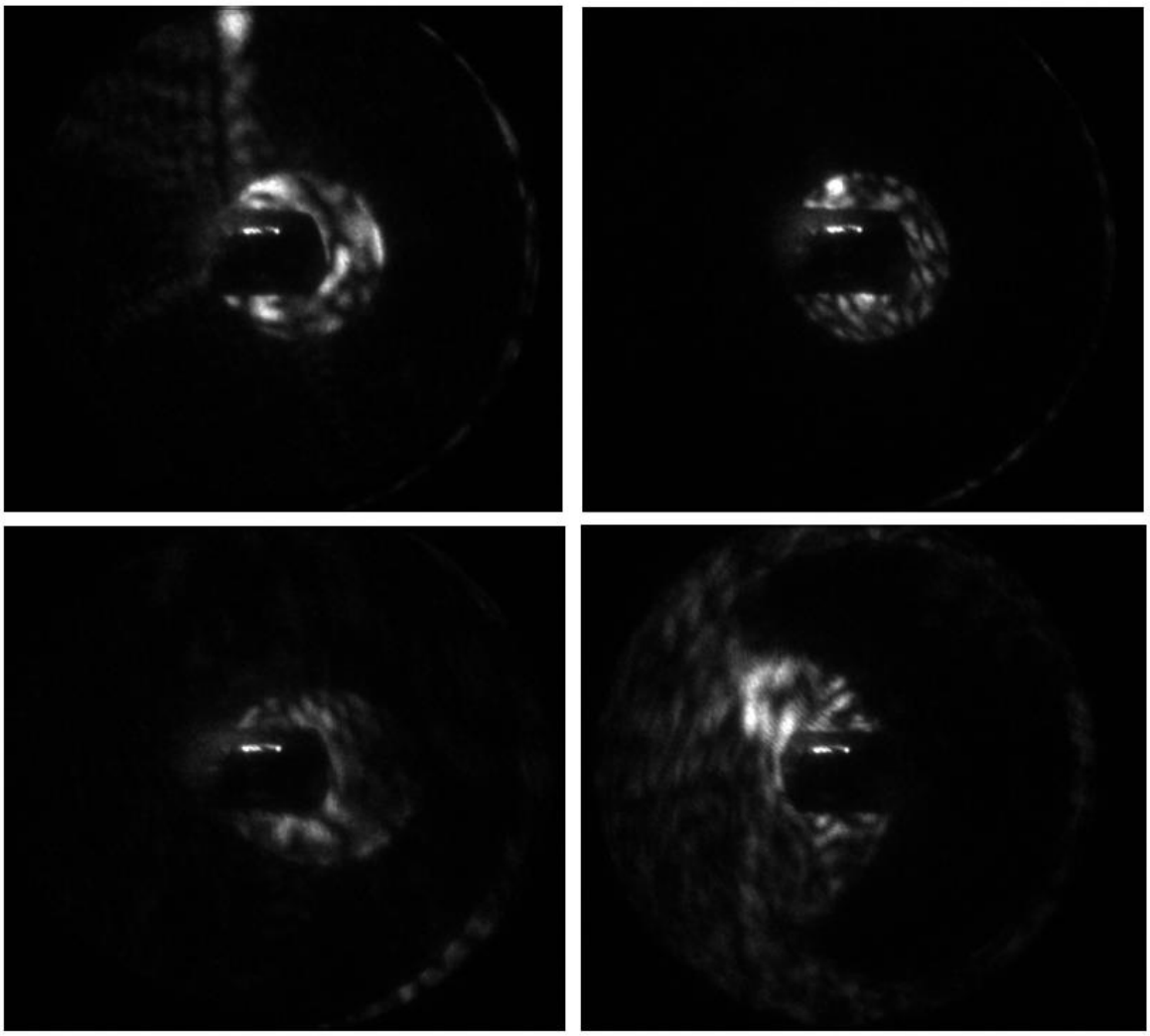

Figure 6.9: SID-3 recorded images of the scattering patterns of ice particles that were observed during flight B890. The scattering patterns have been affected by particle coincidence, as in evident by the dark areas in the patterns, analogous to as if one object were covering another object.

The PSDs calculated from SID-3 data fit those from the 2DS data most accurately when the higher minimum brightness was used (64; pink dots) for images collected during runs 3, 4, and 5, and also allowed a broader size range to be represented; whereas for run 2 the lower minimum brightness setting (32) provided more consistency between the SID-3 and 2DS data. The mean temperature during run 2 was -33°C; for runs 3, 4, and 5 it was -21°C, -10°C, and -3°C respectively. Therefore, for

warmer ice cloud (certainly warmer than -22°C), and mixed phase cloud, using a higher minimum brightness setting (64) provided more reliable PSDs. Using a lower brightness setting (32) resulted in more accurate PSDs when the cloud was colder, less dense, and ice only.

In the particle roughness analysis in this chapter run 2 was considered separately from runs 3, 4, and 5. Therefore a lower minimum mean brightness (32) was set for run 2, and the higher setting (64) was used for the other three runs (3, 4, and 5), which were compared to each other. Following the criteria set out in section 3.3, when the lower setting (32) was used the PSD was truncated at 100µm.

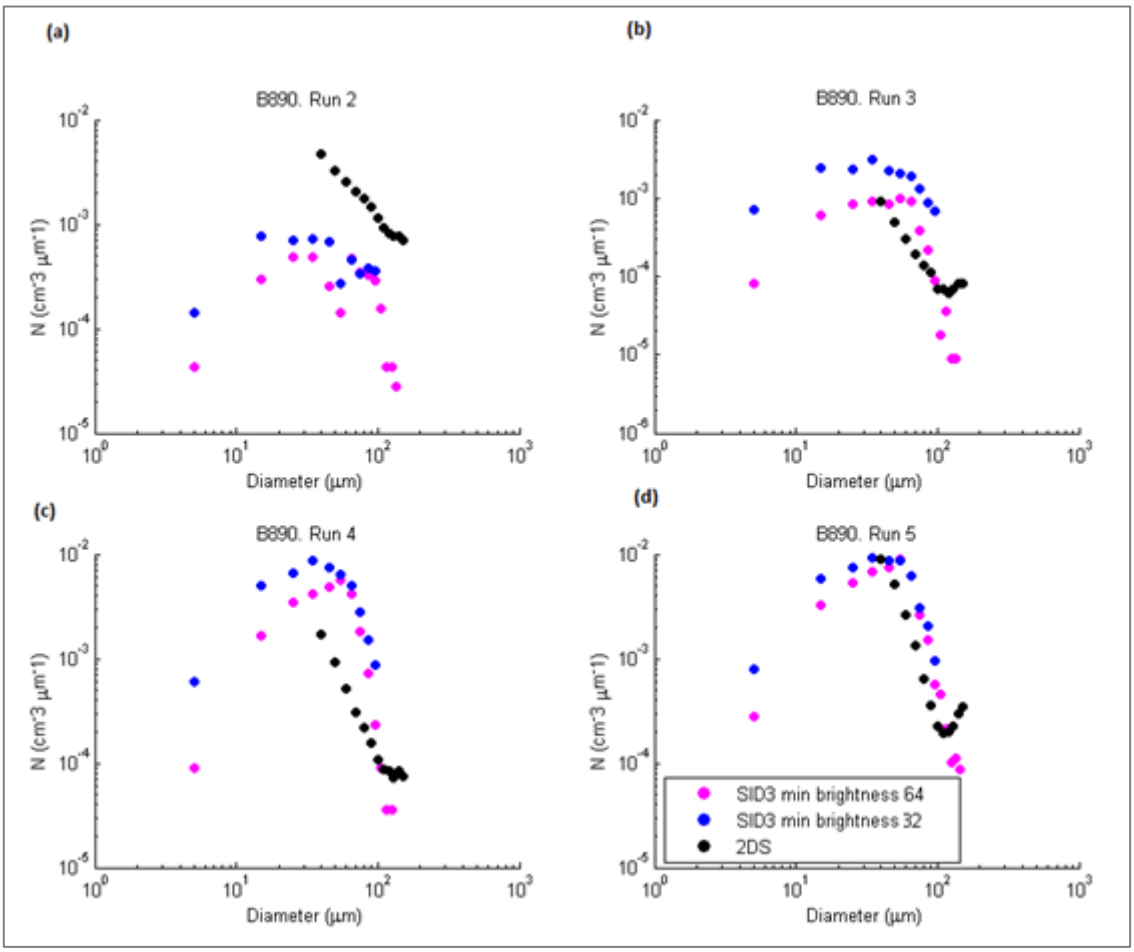

Figure 6.10: PSDs calculated over four different SLRs (a to d) which were conducted during flight B890. The pink data points represent the PSD calculated using the particle size information derived from those SID-3 recorded scattering patterns that had a minimum brightness of 64. The blue points also represent SID-3 data, but the image minimum mean brightness was set to 32 and so include size information estimated from dark images. The black dots represent data from the 2DS.

6.5 Particle Roughness

6.5.1 At the cloud starting edge

The roughness of each particle was calculated based on the amount of speckle present in the scattering patterns; more speckle equates to more roughened and/or complex crystals. A range of roughness values were observed throughout run 2 with the degree of roughness varying from smooth to severely rough, i.e. 0 to 0.9. The range in roughness values is illustrated through the histogram in Figure 6.11 with examples of scattering patterns observed at various values.

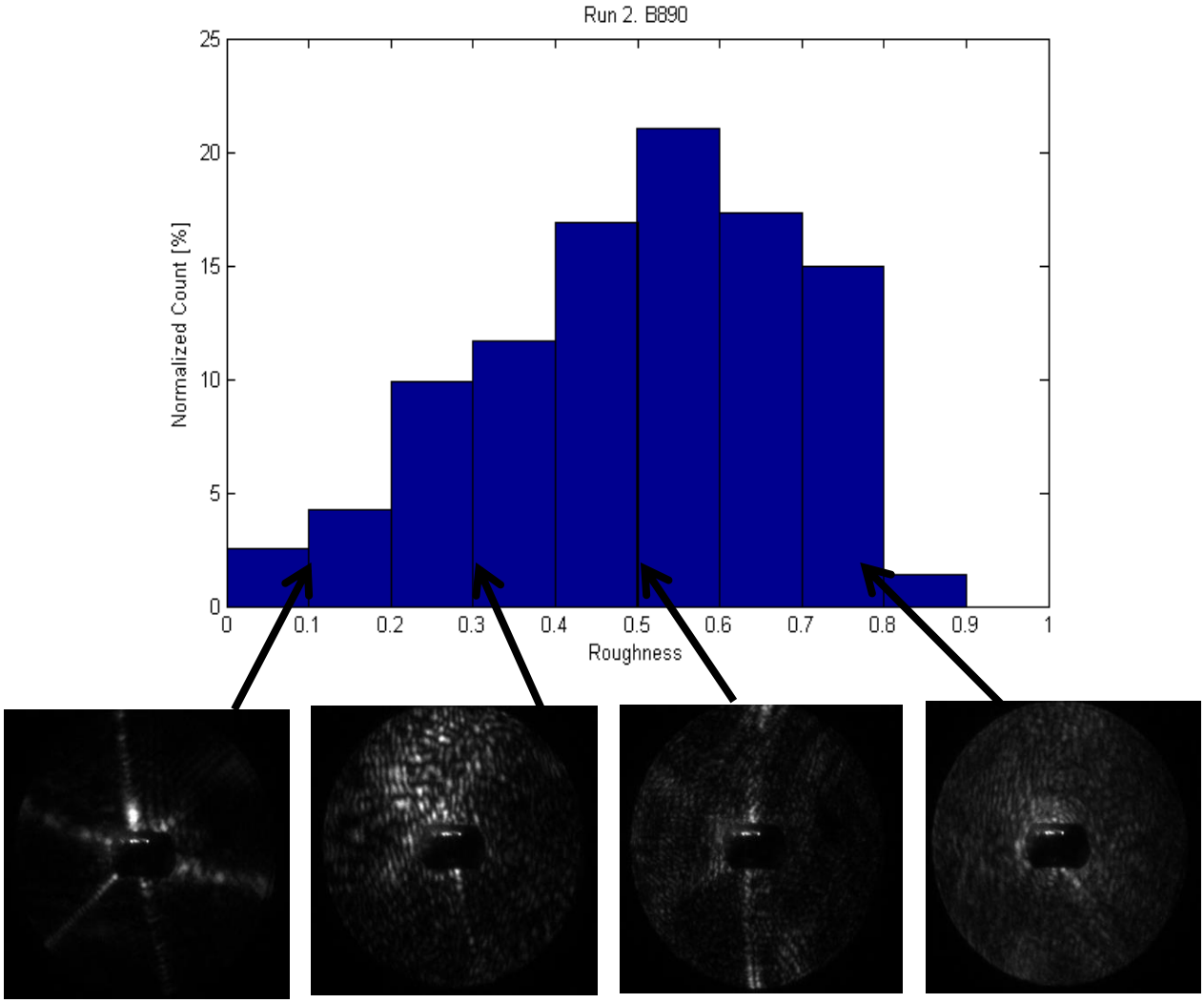

Figure 6.11: The percentage of particles observed with different degrees of particle roughness throughout SLR 2 (0 to 150km from the reference point). The roughness values were estimated from SID-3 scattering patterns. Examples of the scattering patterns imaged by SID-3 during this SLR are shown under the histogram roughly below the degree of roughness to which they corresponded; the arrows show more exactly which roughness value was estimated from each of the images.

The roughness of particles observed at the sharp edge of the wave cloud during run 2, illustrated by the purple box in Figure 6.6, was investigated. The median roughness value each second was calculated at the edge (23.5km - from the ref point; start of run 2; point B in Figure 6.3(a)) and further downwind (up to 40km) where the TWC, particle concentrations and aerosol concentrations became significantly reduced. A range of roughness values were observed throughout the region as illustrated by Figure 6.12. The data were divided into two categories based on their distance from the leading edge, as dictated by the orange line in Figure 6.12. To the left of the orange line (<31km) many peaks in TWC occurred, including the first peak which represented the leading edge of the cloud where recently nucleated ice was expected. To the right of the orange line (>31km) fewer peaks occurred and the TWC gradually reduced towards zero suggesting relatively older ice which had spread as a result of horizontal winds and had started to dissipate. The particle roughness values observed before 31km (orange line), and after 31km were plotted in two separate histograms (Figure 6.13). The histograms represent the percentage of particles with certain roughness values at (a) the cloud leading edge, and (b) further downwind away from the cloud edge; the roughness values of every particle detected by SID-3 were included.

A range of particle roughness values from 0 to 0.8 were seen throughout the cloud leading edge region (Figure 6.13(a)). Further downwind (b), however, smoother particles (0 to 0.2) were not observed.

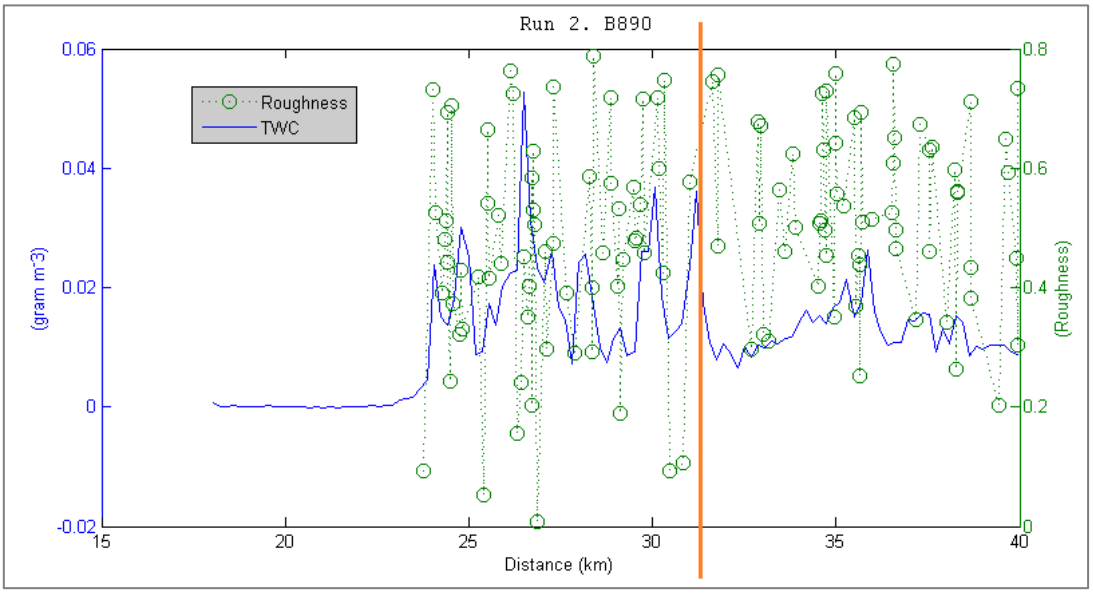

Figure 6.12: The median particle roughness (green) observed each second at the sharp edge of the wave cloud during SLR 2 and then further downwind during SLR 2 have been plotted against the distance from the reference point. The TWC (blue) during the SLR 2 has been over plotted against the distance from the reference point. The orange line separates the distances at which high peaks in TWC were observed and where TWC became more stable.

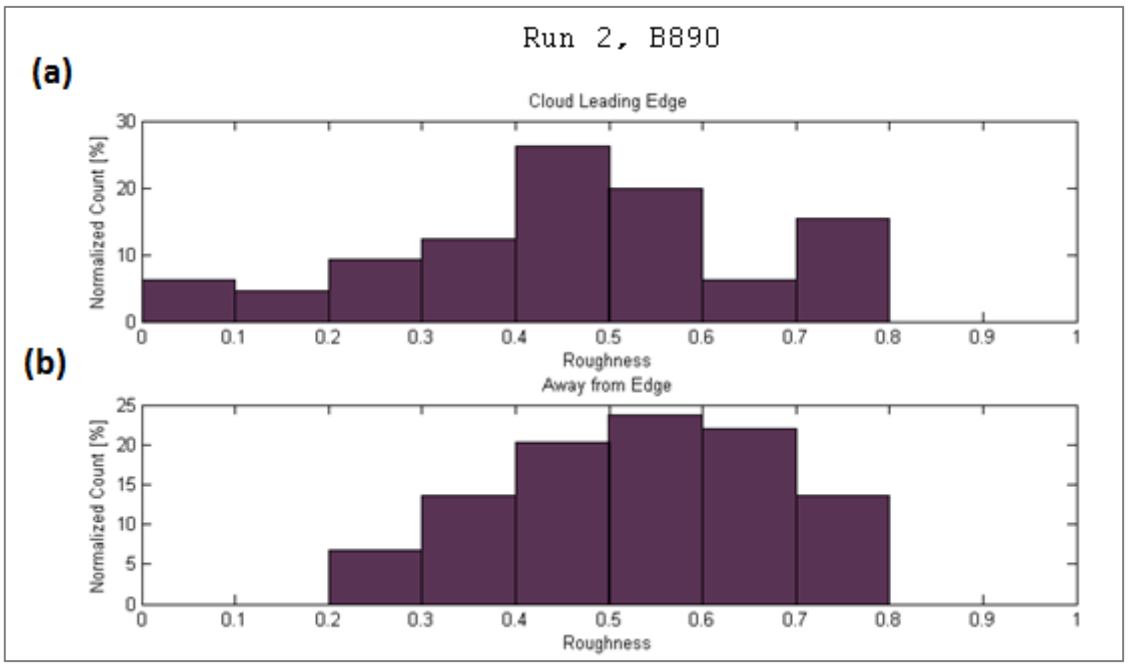

Figure 6.13: Percentage of particles with certain degrees of roughness estimated from the SID-3 recorded scattering patterns (a) at and towards the sharp leading edge of the cloud, and (b) further downwind of the starting edged during SLR 2 B890.

The second cloud section illustrated by the orange box in Figure 6.6 was similarly investigated; the median particle roughness each second was plotted in Figure 6.14 with the TWC. Whereas the first isolated cloud section had a well-defined starting region with high TWC values which decreased downwind, the second cloud section consisted of multiple peaks in TWC interspersed with periods of low TWC. The section of cloud could not therefore be split up into a nucleation region and a growth/dissipation region. Instead the data was split up into two categories based on the TWC; (i) sections with sharp peaks in TWC which were suggestive of nucleation, and (ii) sections downwind of the initial peak which had lower TWC and were therefore expected to host only older crystals. The percentage of particles with specific roughness values were plotted for each of the regions, Figure 6.15.

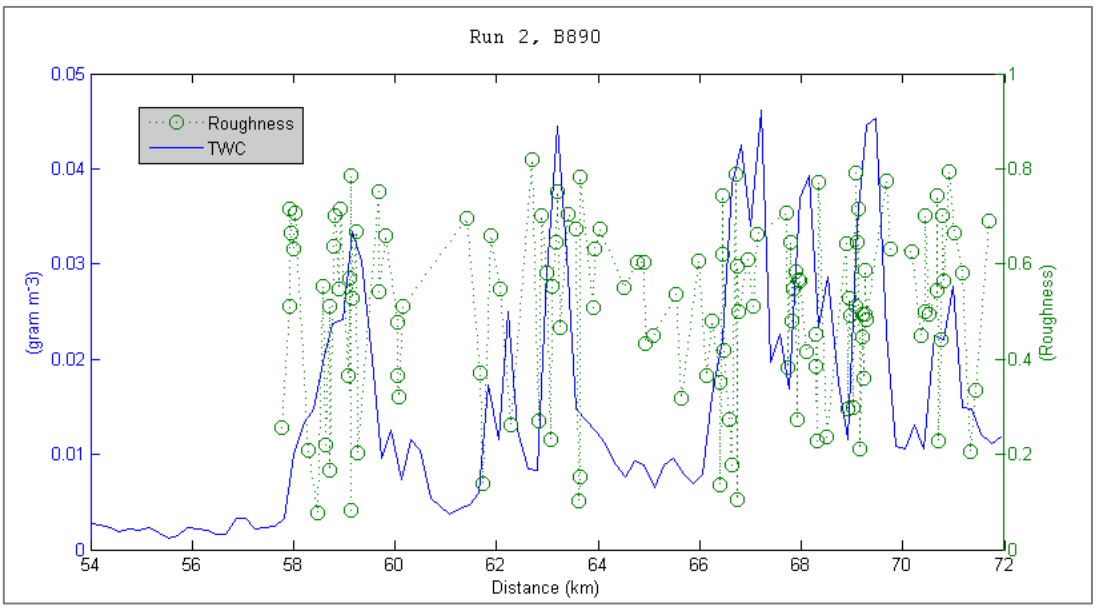

Figure 6.14: The median particle roughness (green) observed each second at the second sharp edge of the wave cloud during SLR 2 and then further downwind during SLR 2 have been plotted against the distance from the reference point. The TWC (blue) during the SLR 2 has been over plotted against the distance from the reference point.

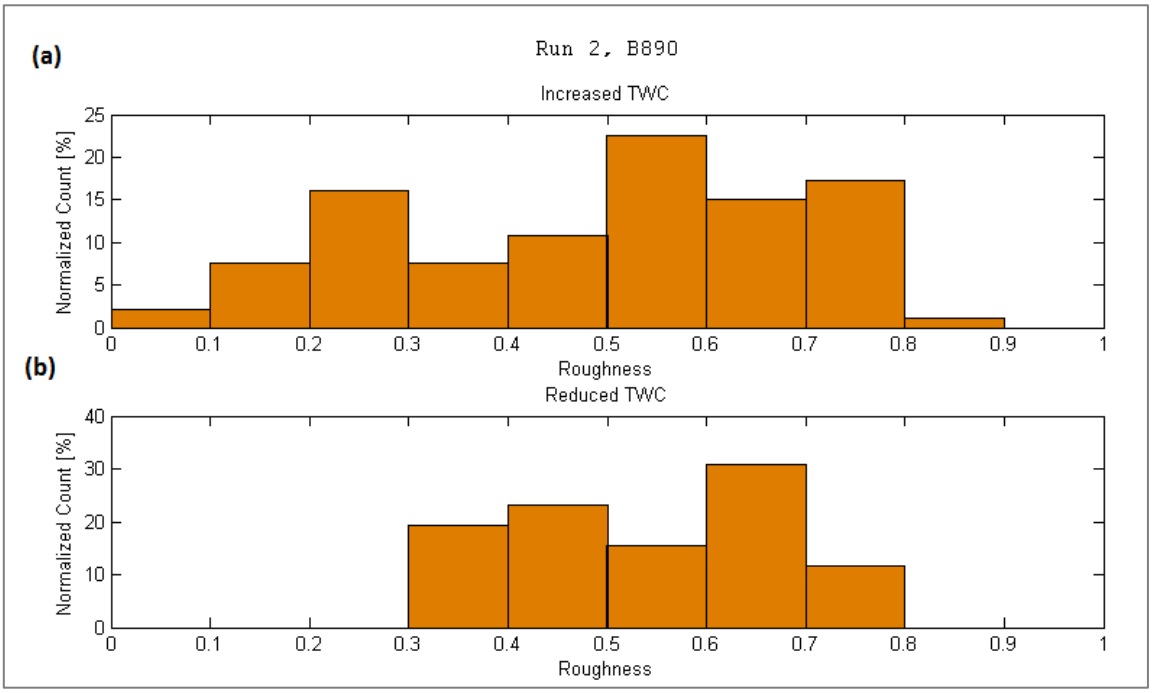

Figure 6.15: Percentage of particles with certain degrees of roughness estimated from the SID-3 recorded scattering patterns (a) in the presence of sharp peaks in TWC, and (b) whilst TWC is lower during SLR 2 B890.

A range of particle roughness values from 0 to 0.9 were observed in suspected nucleation regions when peaks in TWC were present (Figure 6.15(a)). In the cloud sections defined by low TWC

downwind of a TWC peak (b), however, smoother particles (0 to 0.3) were not observed. In this case and in that of the first sharp cloud edge (Figure 6.13), smooth particles were only observed in suspected nucleation regions, suggesting that particles can form with smooth facets and simple shapes, but these features are not maintained, and older crystals tend towards roughness.

The roughness histograms in Figure 6.13 and 6.15 also reveal that rough crystals were observed in the nucleation regions and that this roughness (0.3 to 0.8) was maintained throughout the run.

6.5.2 In supersaturated and subsaturated conditions

The sharp leading edge of the wave cloud which was observed during run 2 was not present during the lower altitude runs 3, 4, and 5: the latter runs started further downwind than run 2 and consequently the first 40km from the reference point were not probed at altitudes below run 2.

During runs 3, 4, and 5, however, regions of both subsaturation and supersaturation were common; subsaturated regions were very rare during run 2. Therefore the data collected during runs 3, 4, and 5 were used to investigate possible differences in particle roughness during periods of potential growth and sublimation.

Particles were categorized depending on whether they were detected in supersaturated regions, which were defined as those where RH_{ice} was greater than or equal to 110%, subsaturated regions where RH_{ice} was less than or equal to 90%, or in saturated regions defined as periods when the RH_{ice} was between 90 and 110%. The saturated regions were further split into two, one from RH_{ice} 100% to 110%, and the other from 90% to 100%. These four different regions are shown in Figure 6.16; only in-cloud regions are shown during runs 3, 4, and 5.

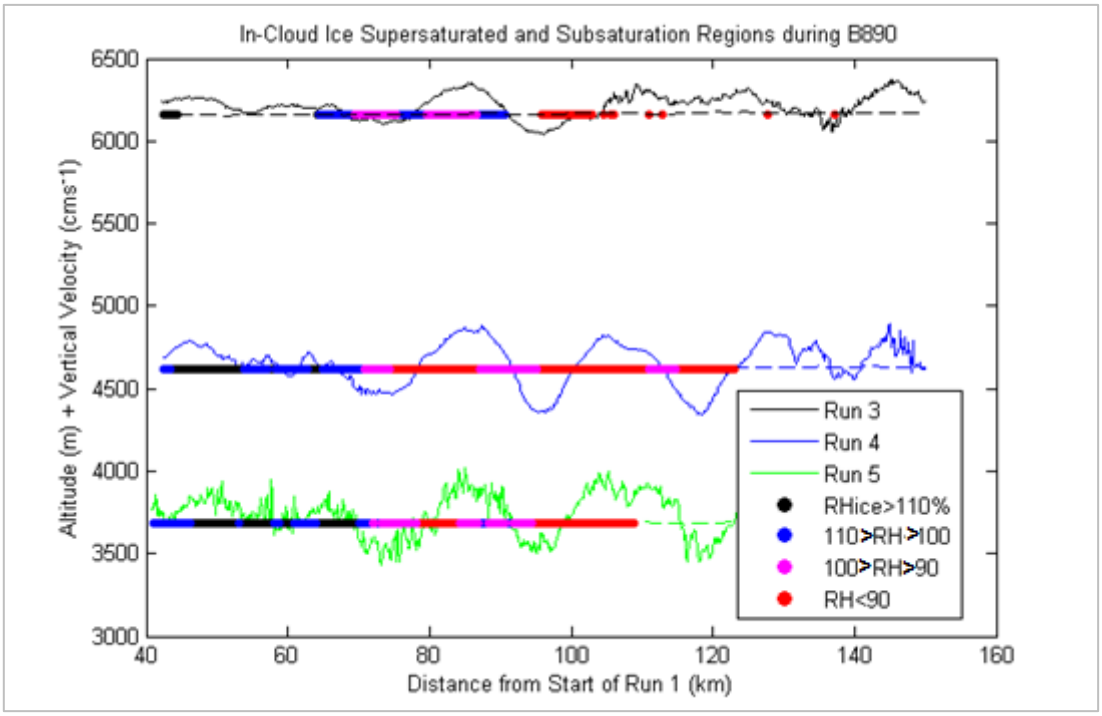

Figure 6.16: Across 3 SLRs (3, 4, and 5) the altitude of the measurement was added onto the observed vertical wind velocity and plotted against the distance from a fixed reference point (point B on Figure 6.3(a)). The dashed lines are the measured altitude only against the distance, and correspond to a vertical wind velocity of zero. The coloured horizontal lines made up of dots correspond to where measurements were taken whilst in environments which had specific ranges of RH_{ice}. Regions of supersaturation were denoted by black dots (RH_{ice}>110%), saturation corresponding to either blue or pink dots (110%>RH_{ice}>100%; 100%>RH_{ice}<90%) , and subsaturation was represented by red dots (RH_{ice}<90%).

During run 3, the environment changed from supersaturated towards the leading edge of the cloud, to saturated further into the cloud, and finally to subsaturated towards the trailing edge of the cloud. The degrees of particle roughness observed in these three environments were compared, as illustrated in Figure 6.17. Similarly to the particles observed during run 2, the particles closer to the cloud leading edge during run 3 dominated the smoother roughness values (0 to 0.2). Although smooth particles were also seen in the subsaturated environment towards the trailing edge of the cloud, moderately rough particles were substantially more common under these subsaturated conditions. The moderately rough particle regime was significantly dominated by particles observed under subsaturation, and the lightly rough particles were most common in the saturated conditions. This suggests that smooth particles tended to occur in supersaturated regions at the cloud leading edge; lightly rough particles were more likely to be observed further into the cloud; and further into the cloud still, towards the trailing edge, particles were most likely to be moderately rough. It is important to note, however, that smooth, lightly rough, and moderately rough crystals were

observed throughout all cloud regions. Severely rough ice was only present in the saturated regions, and only in very low numbers (<3% of all ice observed in the saturated region).

A two-tailed T-test was used to evaluate the statistical significance of the hypothesis that rougher particles tend to be detected in subsaturated conditions, whilst smoother particles are more common in supersaturated conditions. The null hypothesis being that there is no trend between particle roughness and supersaturation/subsaturation. The roughness distributions observed in supersaturated conditions and in subsaturated conditions during run 3 resulted in a t-score of 2.7507, with a degree of freedom of 244. These values gave a p-value of 0.006393 which meant that the null hypothesis could be rejected. Therefore the correlation between particle roughness and supersaturation/subsaturation is statistically significant; that is rougher particles tend to be more common in subsaturated environments, whereas smoother particles are more prevalent under supersaturated conditions.

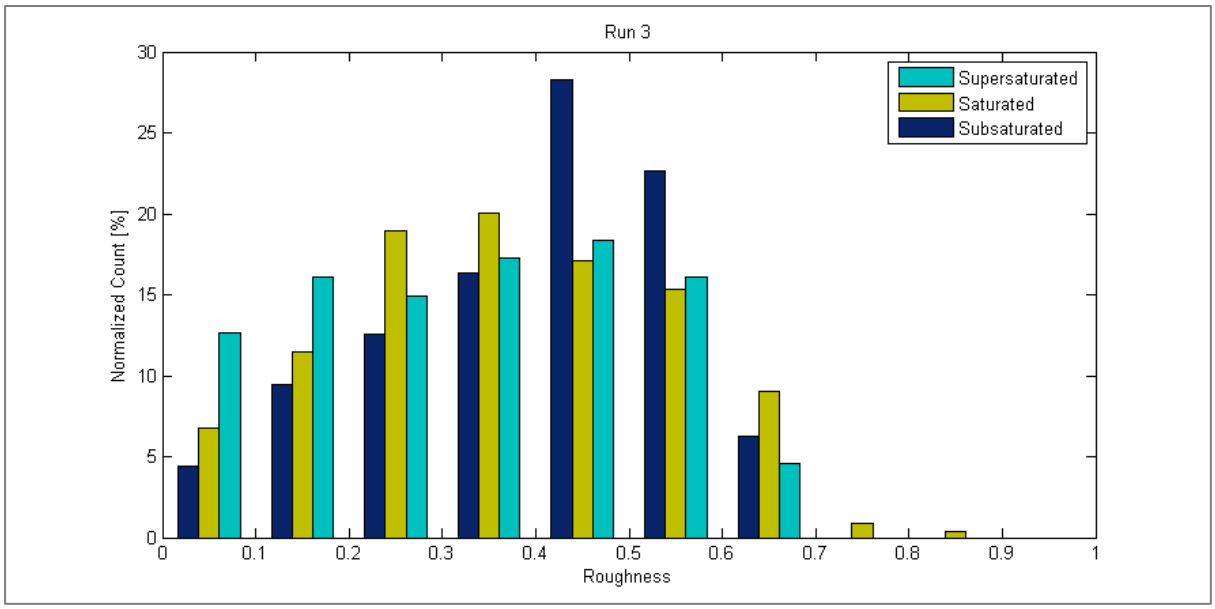

Figure 6.17: The percentage of particles with specific degrees of roughness estimated from the SID-3 recorded scattering patterns which were observed during SLR 3 of B890 in subsaturated (dark blue), saturated (olive green), and supersaturated (light blue) environments, with respect to ice.

A comparison of roughness in supersaturated regions (RH_{ice}>110%) and in subsaturated regions (RH_{ice}<90%) during runs 3, 4, and 5 combined also revealed that smoother and lightly rough particles were more common in supersaturated regions, and moderately to severely rough particles were more common under subsaturated conditions, as shown in Figure 6.18. The ratios of particles that were observed in supersaturated regions to those observed in subsaturated regions are shown in

Table 6.1 for multiple degrees of roughness. The highest ratio was for roughness values of 0 to 0.1 (1.7) and steadily decreased as the degree of roughness increased, i.e. more smoother particles were observed in supersaturated conditions, and more moderately rough crystals were observed in subsaturated regions. Similarly to the data collected during run 3, a two-tailed T-test was used was used to evaluate the statistical significance of this hypothesis. The roughness distributions observed in supersaturated conditions and in subsaturated conditions during runs 3, 4, and 5 resulted in a t-score of 5.8391, and with a degree of freedom of 3210. These values gave a p-value less than 0.00001 meaning that the hypothesis 'rougher particles are more common in subsaturated environments, whilst smoother particles are more common in supersaturated conditions' was statistically significant.

This result is in agreement with the work of Kobayashi and Ohtake (1974), and Pfalzgraff et al., (2010), who have also observed changes in ice crystal surface roughness associated with variation in relative humidity have been observed previously: Kobayashi and Ohtake (1974) found that the facets of crystals which had nucleated in air at temperatures between -26°C and -42°C became grooved during sublimation, but became smooth during re-growth. Pfalzgraff et al., (2010) observed similar behaviour on the facets of hexagonal ice crystals grown in a Scanning Electron Microscope (SEM): roughness in the form of trans-prismatic strands appeared 5-10μm apart during sublimation, but disappeared during re-growth resulting in smooth facets.

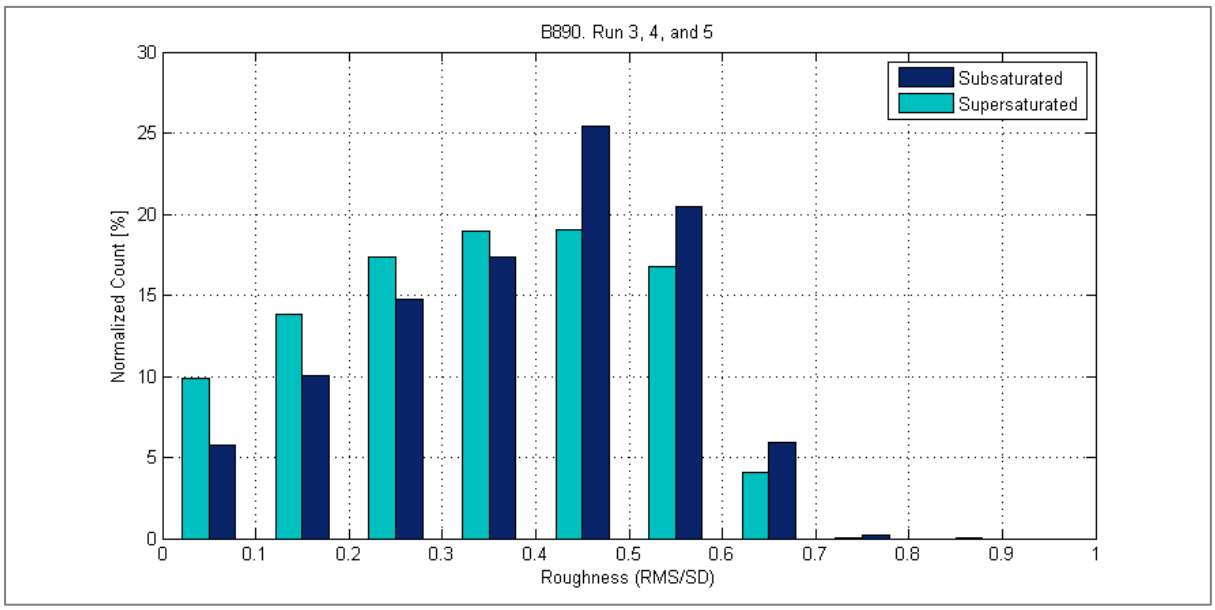

Figure 6.18: The percentage of particles with specific degrees of roughness estimated from the SID-3 recorded scattering patterns which were observed during SLR 3, 4, and 5 (combined) of B890 in subsaturated (dark blue), and supersaturated (light blue) environments, with respect to ice.

Roughness (bin centre)	Ratio of normalized percentages of particles observed in supersaturated regions to those in subsaturated regions
0.05	1.71
0.15	1.38
0.25	1.18
0.35	1.09
0.45	0.75
0.55	0.82
0.65	0.68
0.75	0.45
0.85	0
0.95	N/A

Table 6.1: Ratios of the particles observed in a given roughness range under supersaturated conditions to those observed under subsaturated conditions during runs 3, 4, and 5. Supersaturation was here defined as RH_{ice}>110%, and subsaturation as RH_{ice}<90%.

6.5.3 Effect of Cyclic RH_{ice} Changes on Particle Roughness

Voigtlaender et al., (2013) imaged scattering patterns of crystals in a cloud chamber as they underwent growth and sublimation cycles. Contrary to Kobayashi and Ohtake (1974), and Pfalzgraff et al., (2010), they found that the crystals became roughened during regrowth, and smoother during sublimation; however, repeated cycles resulted in generally rougher crystals.

The only obvious cyclic humidity behaviour occurred during run 3 occurred around half-way through the length of the cloud that was probed, at which point the RH_{ice} switched between (i) 110%>RH_{ice}>100%, and (ii) 100%>RH_{ice}>90% multiple times. This region of cloud was split up into multiple sections to investigate the influence that the cyclic change in RH_{ice} had on the particle roughness. The cyclic change in RH_{ice} along the run is highlighted by the yellow box in Figure 6.19, whch shows the RH_{ice} values during the in-cloud measurement of run 3 as a function of distance from the reference point.

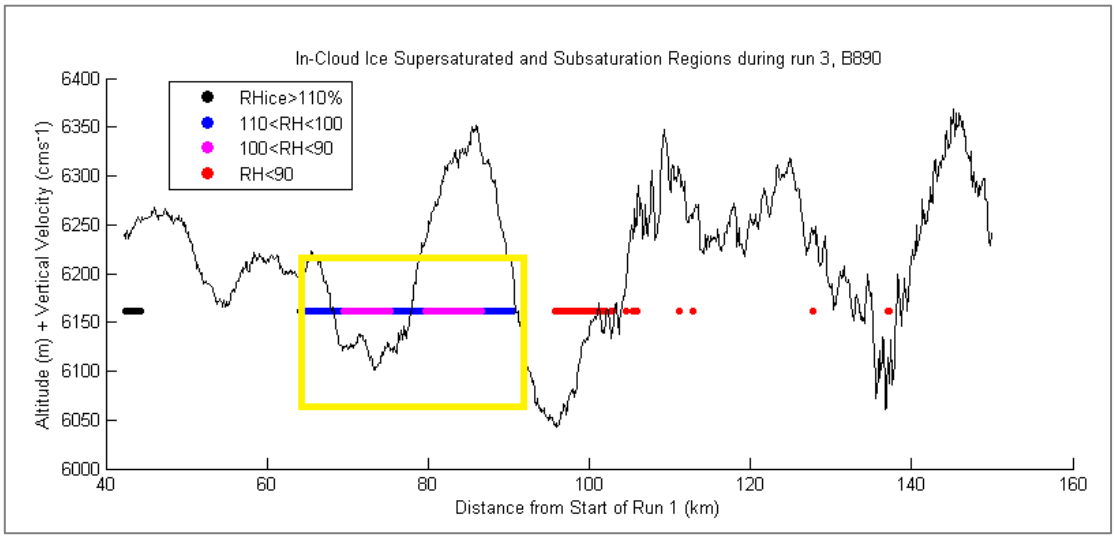

Figure 6.19: The altitude of the measurement during SLR 3 was added onto the observed vertical wind velocity and plotted against the distance from a fixed reference point (point B on Figure 6.3(a)). The dashed lines are the measured altitude only against the distance, and correspond to a vertical wind velocity of zero. The coloured horizontal lines made up of dots correspond to where measurements were taken whilst in environments which had specific ranges of RH_{ice}. Regions of supersaturation were denoted by black dots (RH_{ice}>110%), saturation corresponding to either blue or pink dots (110%>RH_{ice}>100%; 100%>RH_{ice}<90%) , and subsaturation was represented by red dots (RH_{ice}<90%). The cyclic change in RH_{ice} from just over 100% to just below 100% has been highlighted by the yellow box.

Each section was given a name relating to whether RH_{ice} was HIGH (110%>RH_{ice}>100%) or LOW (100%>RH_{ice}>90%) followed by a number to denote its position in the cyclic sequence: HIGH1, LOW1, HIGH2, LOW2, HIGH3; these names are used as labels in Figure 6.20. The roughness of all particles

detected in each of these sections was retrieved from the scattering patterns recorded by SID-3. The percentage of particles of a specified roughness (10 bins from 0 to 1) were plotted in Figure 6.20(a) for each of the sections separately; the roughness values were then sorted into 4 bins to reduce the number of bars in the plot and make visualising the general changes in roughness easier. The order of the bars corresponds to the regions position in the cyclic RH_{ice} sequence.

It is assumed that particles passed through the five regions consecutively due to the strong horizontal winds and the laminar flow in wave clouds. Therefore if the humidity values were fairly stable then a particle which was detected in the fifth region (HIGH3) would have previously passed through all of the other regions in order.

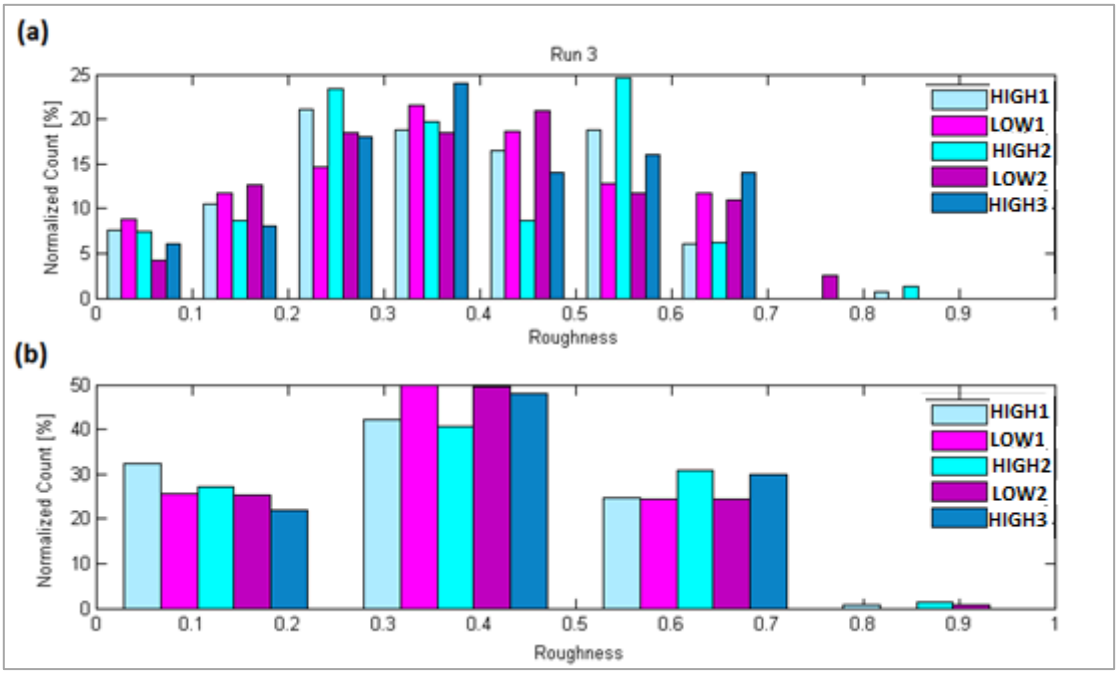

Figure 6.20: The percentage of particles with specific degrees of roughness estimated from SID-3 recorded scattering patterns which were observed in the presence of alternating RH_{ice}; the blue represents particles observed when RH_{ice} was between 100% and 110%, and the magenta when RH_{ice} was between 90 and 100%. The four regions are shown separately and have been sorted into (a); 10, and (b) 4 roughness bins ranging from 0 to 1, where 0 is smooth and 1 is very rough.

The data presented in Figure 6.20, however, did not illustrate the cyclic changes in roughness with cyclic changes in RH_{ice} that have been seen in controlled laboratory experiments (Voigtlaender, et al., 2013; Kobayashi & Ohtake, 1974; Pfalzgraff, et al., 2010). There are, however, higher percentages of rougher crystals observed *in situ* after they have gone through multiple cycles of growth and sublimation as illustrated by Figure 6.21, which agrees with the cloud chamber experiments by

Voigtlaender et al., (2013). The correlation, however, was fairly weak and a one-tailed T-test could not show that the correlation between particle roughness and growth/sublimation cycles was statistically significant.

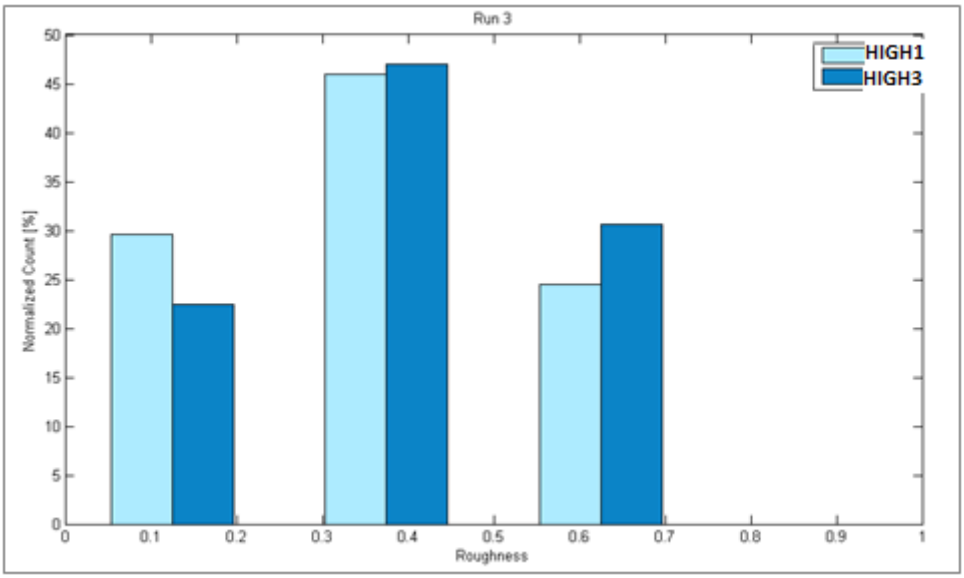

Figure 6.21: The percentage of particles with various degrees of roughness estimated from SID-3 recorded scattering patterns which were observed in supersaturated regions only. The first region, HIGH1 (light blue), was followed by regions of both supersaturation and subsaturation. The second plotted region, HIGH3 (dark blue), then followed these. The regions are shown separately and have been sorted into 4 roughness bins from roughness values of 0 to 1.

6.6 Conclusions and Further Work

A wave cloud was detected over the Scottish Highlands during flight B890 on the 6th March 2015. The cloud was expected to have formed as a consequence of strong updrafts due to the occurrence of atmospheric gravity waves (AGWs). The AGWs were confirmed by the presence of a 90° phase shift between temperature and the vertical component of wind. Straight level runs (SLRs) were executed at multiple altitudes between two points relative to the ground. Ice water was predominant throughout the SLRs performed between 9.2km and 3.7km. Liquid water dominated during runs at altitudes of 2.451km and below. These latter runs were not considered in the analysis presented here.

A range of ice crystal roughness values were observed at all altitudes. This range covered smooth/non-complex particles, low and medium degrees of roughness/complexity, and severely roughened crystals.

Two sharp cloud edges were identified during run 2 by sudden and significant increases in TWC. These were accompanied by peaks in ice particle concentration and aerosol concentration suggesting nucleation, which at the temperatures measured (-33°C) was likely to be heterogeneous. In these regions various degrees of particle roughness were observed including smooth particles (roughness ≤ 0.2), which were not present further away from the leading edge. Therefore in supersaturated conditions smoothness was present at the time of nucleation, but was not maintained; crystals became anywhere between lightly rough (0.25 to 0.5) and severely rough (0.75 to 1.0), although moderately rough particles (0.5 to 0.75) marginally dominated over the entire run. The percentages of particles which were smooth, lightly rough, moderately rough, and severely rough were 12%, 34%, 47%, and 7%, respectively.

The particle roughness observed in supersaturated regions and subsaturated regions during runs 3, 4, and 5 were compared. Smooth particles were more common in supersaturated regions; lightly rough particles were present in both regions in roughly equal numbers; and moderately rough crystals were more common in subsaturated regions. Severely rough particles were not widely observed (<1% of the total particles). This suggests that crystals are more likely to tend towards rougher values when observed in subsaturated environments (a statistical T-test showed this hypothesis to be statistically significant); however, it is not to say that crystals cannot also become less rough, since the broad range in degree of roughness (0 to 0.8) was generally maintained between the two regions, i.e. the smoother crystals were still present in the subsaturated region, but in fewer numbers.

In a region of cyclic RHice variation (from 110%>RH_{ice}>100% to 100%>RH_{ice}>90% thrice) no correlation between the cycles and particle roughness variation was observed. Rougher particles were, however, more common after multiple changes in RH_{ice} (which could promote cycles of particle growth and sublimation). The correlation was weak however, and could not be shown to be statistically significant.

Cycles of crystal growth and sublimation have been shown to affect crystal roughness in the laboratory (Voigtlaender, et al., 2013; Pfalzgraff, et al., 2010; Kobayashi & Ohtake, 1974) but further research is required to provide insight into the effect of this process *in situ*. Wave cloud should provide an ideal study for this since it typically has relatively well defined starting edges where crystals grow/regrow, and trailing edges where crystals can undergo sublimation. Furthermore aggregation is negligible in these clouds, and therefore any observed speckle in the scattering patterns will be a consequence of particle roughness which has occurred under specific atmospheric conditions, i.e. sublimation.

The wave cloud study presented here was not initially intended as a cloud study, but as a wind study; it was purely coincidental that cloud was present. As a consequence of this, the cloud leading edge was not probed at most altitudes; and any possible smaller isolated clouds had spread into each other due to the strong horizontal winds. A fully planned wave cloud flight would be required to identify variations in ice crystal roughness as they experience growth and sublimation cycles *in situ*.

7 Conclusions and Summaries

Crystal habits, crystal size, growth processes, and nucleation modes can all affect the radiative forcing of clouds to different degrees (Zhang, et al., 1999; Mitchell, et al., 2008; Haag & Kärcher, 2004; Jensen, et al., 2001; Liou & Takano, 1994; Mitchell, et al., 1996; Mitchell, et al., 1996b). Due to limitations in measuring small ice crystals (previously mentioned in section 1.1.3), there are still large uncertainties in cirrus microphysics and hence their net radiative forcing. Further research is required to identify and quantify the occurrence of small ice particles in cirrus. As well as size, particle roughness can also have a significant effect on cloud forcing. Ulanowski et al (2006) made measurements of scattering patterns of laboratory grown ice analogue crystals and revealed that rough surfaces could reflect almost twice as much incident solar SW radiation as smooth surfaces. The difference in the cooling effect between a cloud of only severely roughened ice and a cloud of only smooth ice is comparable to the magnitude of warming by the greenhouse gases (Yi, et al., 2013). This highlights the importance of current and future research into ice particle roughness in cirrus.

7.1 Refining requirements of images for reliable results

Objective: *Execute and use laboratory measurements using ice analogues and SID-3 to refine pre-existing data-processing techniques and assess the reliability of existing data, i.e. whether particle characteristics can be accurately estimated from dark scattering pattern images.*

The Small Ice Detector 3 (SID-3) can be used to uniquely determine particle size and roughness/complexity from two-dimensional scattering patterns that are imaged when a particle passes through the laser path and the light scattered in the forward direction (6-25°) is directed onto an intensified charge-coupled device (ICCD). Since this method of retrieval is novel, for atmospheric ice particles, laboratory experiments were setup to test and improve the characterization techniques.

These experiments were used to determine:

1. The maximum number of saturated pixels allowed before images were unrepresentative of the corresponding particle (section 3.2).
2. The amount of speckle required for accurate size estimation (3.3).
3. The minimum mean brightness required over the entire image for accurate particle property retrieval (3.4).

4. Whether images recorded under different camera settings could be reliably compared (3.5).

It was shown that many saturated pixels could cause the apparent merging of speckle spots, which increased the median spot area, and therefore caused the imaged particle to be undersized. Multiple values for the maximum allowed number of saturated pixels were investigated. The relative error (%) was calculated for each particle used in the experiment and the particles were then grouped, in roughly equal numbers, dependent on the number of saturated pixels present in their scattering patterns and the root-mean-square value of each group was calculated (Table 3.1).

The errors were considerably lower when only images with fewer than 1087 saturated pixels were used in analysis; above this threshold the errors become substantially more significant. The maximum number of pixels allowed before the images were rejected was therefore set to 1087. Figure 3.4 shows two regression plots between measured and estimated particle diameter when the maximum pixel criterion was set, and when no criterion was set.

Similarly a criterion was chosen for the image minimum mean brightness required for the size and roughness retrieval to be reliable. This was investigated as a direct consequence of unexpected particle size distributions (PSDs) estimated from *in situ* measurements, which were noticed to have occurred in the presence of many dark images. Consequential laboratory experiments showed that dark images of small particles (<12µm) could provide accurate size values, but could also provide values which were significantly over-estimated (>100µm), there was no obvious in-between, as shown in Figure 3.12. Therefore since small particles were the priority in this project, and the dark images were suspected of representing these, in order to retain as much information about small particles as possible dark images were included in much of the analysis of *in situ* data. Consequently particles with estimated diameters greater than 100µm were rejected in order to minimise the number of miss-sized particles from the dark images.

There was however an exception to this criterion: if measurements were expected to be in the presence of particles which were not necessarily as small, and consisted of many larger particles (>15µm). This occurred at relatively warmer temperatures and lower altitudes during flight B890. Furthermore, at these warmer temperatures where cloud was approaching mixed-phase (mixed-phase at lower altitude), the concentrations were greater and therefore coincidence was more likely. Coincidence exhibits itself in the SID-3 images as darkened areas, analogous to an object being covered by another object, as illustrated in Figure 6.9. Therefore the dark image criterion was not set here, and dark images were rejected, in order to reduce the possibility of analysing scattering patterns that exhibited coincidence.

Another experiment was run to investigate the degree of speckle required to achieve accurate size estimation. The degree of speckle was equivalent to the estimated roughness of the particle from the scattering patterns, i.e. 0 to 1. Increasing the amount led to increasingly more accurate results (up to 0.4), but also decreased the volume of data. Therefore a compromise was made based on the laboratory results and *in situ* results (from flight B672). The laboratory results showed significant improvement in accuracy when changing the minimum degree of speckle (particle roughness) from 0.15 to 0.2, although 0.4 did provide the best accuracy, Figure 3.5. The *in situ* particle size distributions, however, were very similar shapes when either 0.2 was used or when 0.4 was used as a minimum, with only the concentrations being reduced for the latter setting, Figure 3.6. It was therefore decided that particles with a minimum roughness of 0.2 would have reliable estimated diameters associated with them, and would therefore be used in further analysis.

Finally, the effect of changing the camera intensifier gain of the SID-3 instrument was investigated since it has not always been set to the same value during field campaigns; the intensifier gain can be changed to suit the general size of the particles that are being measured. Generally a combined measure of roughness is used, as described in detail in section 2.2.3.1, which contains the contributions of three statistical measures. These measures and the combined measure were all compared to find the most consistent over different intensifier gains. The fit between estimated diameters measured from scattering patterns recorded when the gain was high and then when it was low (a separation of 10units) was most consistent when the log kurtosis measure was used for small particles (<30µm), and when the RMS/SD of the image brightness was used for particles greater than 30µm. These are illustrated by Figures 3.15 and 3.17 where the former consists of particles with measured diameters less than 30µm, and the latter includes particles with measured diameters between around 30µm and 150µm.

Although these two roughness measures were the most consistent across different gains, there were still discrepancies between measurements when ten bins were used for roughness, 0 to 1 in steps of 0.1. The discrepancies were reduced significantly when only four bins were used, as illustrated in Figure 3.22. The four bins were categorized as containing ‘smooth particles’, ‘lightly rough particles’, ‘moderately rough particles’, and ‘severely rough particles’, and were used only when data collected using different intensifier gains were compared. If the gain was consistent then the combined roughness was used and the roughness values were sorted into ten bins.

7.2 Roughness *in situ*

7.2.1 The degree of roughness observed *in situ*

Objective: *From the 2D scattering patterns of ice particles captured in situ by SID-3, quantify the degrees of ice particle roughness observed during multiple ice cloud research flights.*

Sections of five flights were chosen for particle roughness analysis and comparison. Two of the flights were executed during the PIKNMIX campaign in January 2012 (B671, B672), and the other three during the CIRCCREX campaign in March 2015 (B890, B894, B895). All five flights were conducted out of Prestwick airport and measurements were taken in the surrounding area. The flights were chosen based on the presence of ice cloud. Each section occurred at an altitude of over 6km, above which ice clouds are expected to form (Hamblyn, 2008). Where the temperature was 233K (-39°C) or less, and the RH_{ice} was 100% or greater the cloud was expected to consist of entirely ice (Irvine, et al., 2012), and these sections were chosen. In order to extend the amount of data and the number of different ice cloud cases, however, sections were included which may have fallen short of these requirements. In these cases the SID-3 scattering patterns were inspected visually to ensure that only ice was present and no liquid water droplets were detected, i.e. there were no scattering patterns which resembled concentric rings.

The criteria defined by the laboratory experiments in Chapter 3 and the analysis methods described in Section 2.2.3 were used to retrieve ice-particle roughness values from the scattering patterns. The roughness values were sorted into four categories corresponding to different degrees of roughness: smooth, lightly rough, moderately rough, and severely rough.

When all the flights were combined the majority of particles (51%) were categorised as lightly rough; the second most common roughness type was moderately rough (39%). Smooth particles made up 10% of the total particles, and <0.02% were classed as severely rough (Figure 4.6).

When considering the flights separately, for the flight sections from B671, B672, and B894 lightly rough particles were the most common (61%, 64%, 53% respectively); the most common degree of roughness during B890 and B895 were moderately rough, which made up 59% and 46% of the total particles, respectively. Over all five flights the percentages of smooth particles were fairly consistent (8% to 11%), and the same applies to severely rough particles (≈0%).

The roughness values were investigated in more depth for B890 (Chapter 6) since wave cloud was probed and these tend to have well-defined edges where nucleation occurs; hence distance from the starting edge can act as a proxy for time since nucleation. Sharp edges were seen during only

one straight level run (SLR2) as a consequence of the following SLRs starting in the cloud; this flight was not initially intended as a wave-cloud study, but as a wind study. Throughout the SLR, as seen in Figure 4.6, the most common degree of roughness was moderately rough; although a range of values were observed from 0 to 0.9 (smooth to severely rough). The percentages of particles which were smooth, lightly rough, moderately rough, and severely rough were 12%, 34%, 47%, and 7%, respectively.

7.2.2 Roughness and meteorological values

Objective: *Investigate potential influences of meteorological conditions on particle roughness*

Two sharp cloud edges were identified during B890 SLR2 by sudden and significant increases in TWC. These were accompanied by peaks in ice particle concentration and aerosol concentration suggesting nucleation, which at the temperatures measured (-33°C) was likely to be heterogeneous. In these regions various degrees of particle roughness were observed including smooth particles (roughness ≤ 0.2), which were not present further away from the leading edge. Therefore at the cloud leading edges smoothness was present at the time of nucleation, but was not maintained; crystals became anywhere between lightly rough (0.25 to 0.5) and severely rough (0.75 to 1.0), although moderately rough particles (0.5 to 0.75) dominated over the entire run. This is illustrated in Figure 6.13 and 6.15.

During the wave-cloud flight B890 SLRs 3, 4 and 5 there were sections of supersaturation and subsaturation. The particle roughness values observed in both of these regions were compared. Smooth particles were more common in supersaturated regions; lightly rough particles were present in both regions in roughly equal numbers; and moderately rough crystals were more common in subsaturated regions. Severely rough particles were not widely observed (<1% of the total particles). These degrees of roughness were illustrated in Figure 6.21. The result suggested that crystals are more likely to tend towards rougher values when observed in subsaturated environments (a statistical T-test showed this hypothesis to be statistically significant); however, it is not to say that crystals cannot also become less rough, since the broad range in degree of roughness (0 to 0.8) was generally maintained between the two regions, i.e. the smoother crystals were still present in the subsaturated region, but in lower numbers.

In a region of cyclic RH_{ice} variation (starting from 110%>RH_{ice}>100% and changing to 100%>RH_{ice}>90% three times) no correlation between the cycles and particle roughness variation was observed. Rougher particles were, however, more common after multiple changes in RH_{ice} (which could

promote cycles of particle growth and sublimation). The correlation between roughness and growth/sublimation cycles, however, was not able to be proven statistically significant by a T-test.

The relationship between relative humidity and ice particle roughness was also investigated for the sections taken from multiple flights. There were, however, no identifiable trends. The general lack of correlation is not entirely surprising due to the nature of the data collection: all of the measurements were instantaneous and therefore do not provide a history of the atmospheric conditions encountered by a particle before it is detected. This is more so true of cirrus cases than wave-cloud cases, the latter of which, as previously mentioned, have more easily defined nucleation regions.

The same issue with instantaneous measurements was expected to explain the lack of correlation between particle roughness and temperature for the same flight sections. There were no strong trends between the two variables, however there were no smooth particles observed at temperatures below -50°C, highlighting a potential (weak) trend.

The air mass origins of the five flight sections, in combination with the PSDs, were calculated in order to investigate the reason for the differences between the most common degrees of roughness during each flight. Generally higher concentrations of smaller particles in the PSDs which were more positively skewed were observed for flights B671 and B672. This was seen in combination with an ocean-only 5 day back-trajectory of the air-mass (fewer anthropogenic aerosols to act as ice nuclei). The opposite (fewer smaller particles, more evenly distributed PSDs, and continental air-mass origins) were observed during the sections of flights B890, B894, and B895. The more positively skewed PSDs (B671 and B672) are more likely to be representative of homogeneous nucleation since a relatively high number of crystals will nucleate at one time and the high demand for water vapour in order for all of the crystals to grow may not be met which causes the crystals to remain relatively small. Therefore, since the ratio of lightly rough to moderately rough crystals is greater during flights B671 and B672 (ratios of 2.0 and 2.7 respectively) compared to flights B890, B894, and B895 (ratios of 0.6, 1.5, and 0.9 respectively) it is possible that the type of ice nucleation had an impact on the particle roughness. Although the chosen flight sections contained the highest relative humidities, and lowest temperatures in order to reduce the possibility of analysing older well-evolved ice, it is entirely possible that the measurements taken during B890, B894 and B895 were conducted in older cloud where ice had become larger and more complex as a consequence of time as opposed to nucleation method. Again, this can be a limitation of making instantaneous *in situ* measurements from which a crystal's history is not known.

7.3 Future work

Due to limitations associated with instantaneous measurements, it can be challenging to observe how ice particles evolve *in situ*, since the history of the individual crystals is unknown. It is possible to build a picture on a larger scale by considering the evolution of ice-cloud on the whole, i.e. by assuming that crystals nucleated at cloud top and will grow and fall towards cloud base. For many ice clouds, such as cirrus, assumptions may be made based on, for example, relative humidity and temperature measurements, to identify regions of potential nucleation. Orographic clouds, however, can provide the more robust estimation since they generally have sharp-leading edges where nucleation events are expected to occur. They are therefore a good case study for the degree of roughness and/or complexity associated with ice crystals which have recently nucleated. Furthermore since the particles follow streamlines and mixing between these streamlines is negligible, it is not unreasonable to assume that measurements throughout the cloud are those of single crystals as opposed to aggregated particles. Since crystals follow these streamlines, the distance from the sharp-leading edge can act as a proxy for time since nucleation. The mapping of ice crystals' roughness as a function of time since nucleation can be assumed to be estimated more accurately using wave-cloud data than for other cloud types. Therefore measurements of wave-cloud should be used to further investigate the degree of ice crystal roughness present *in situ*, and the processes and atmospheric conditions that can induce it.

During these flights the Small Ice Detector 3 (SID-3) would be used to record the scattering patterns of particles, from which the roughness can be retrieved using the method described in section 2.2.3. A more recently developed probe the Aerosol Ice Interface Transition Spectrometer (AIITS) could also be used for the retrieval of particle-roughness information. AIITS was created at the University of Hertfordshire as an addition to the Small Ice Detector range of probes. It works on the same principles as SID-3: it records the scattering patterns created from the forward scattering of light (6-25°) by particles which pass through a λ532nm laser beam. AIITS, however, has an additional camera, which means that the number of scattering patterns recorded in a second can be increased from 30 (SID-3) to 60. The intensifier gains of the two cameras can be set to two different values, which can increase the useful size range of particles measured. This could also help to reduce the number of dark images recorded, without compromising the number of larger particles being measured, i.e. one gain would be high such that the images of very small particles were bright enough for analysis, and the other gain would be lower so that the number of saturated pixels in an image is not too high for larger particles to be rejected from further analysis. These two issues associated with image brightness have arisen with SID-3 data and were discussed in detail in Chapter

3. The roughness (and size) of particles can be retrieved from the scattering patterns in the same way as for SID-3.

AIITS has been involved in one flight campaign since it was created in 2015. As part of the Coordinated Airborne Studies in the Tropics (CAST) campaign, AIITS flew on NASA's Global Hawk in February 2015. It is due to be certified to fly on the FAAM BAe-146 research aircraft in the upcoming year.

Using AIITS and SID-3 simultaneously during the same flight could provide the user with a database of scattering patterns three times as large as if only SID-3 was used. Depending on the camera intensifier gain settings, the particles measured by each of the cameras could be similar sizes, different sizes with some overlap, or three different size ranges. The former two may provide a way to validate the instruments; the latter, although it may still only cover the range 1 to 150µm, will result in potentially more measurements over that range and therefore lower uncertainties associated with counting statistics.

7.4 Acknowledgements

I would like to thank my supervisor Prof. Joseph Ulanowski, secondary supervisor Dr. Evelyn Hesse at the Centre for Atmospheric and Instrumentation research at UH, and Dr Richard Cotton at the UK Met Office for their support and advice throughout this project. I would also like to thank Dr Edwin Hirst, Dr Richard Greenaway and Dr Chris Stopford at UH for assistance and support with the Small Ice Detector 3.

I am grateful to UH for funding this PhD studentship and to NERC for the funding of the CIRCCREX campaign. Many thanks to everyone involved in the planning, execution, and support of the campaign, including the teams from FAAM, OBR at the Met Office, the University of Manchester, and the TAFTS team at Imperial. Particular thanks go to the FAAM team for providing much appreciated core data and cloud data, and for their support post campaign with the data.

Many thanks also go to my family, especially my parents for their support and generosity throughout my education.

Finally, thank you to Alan for being a brilliant proof-reader during the final year of my PhD. Thanks for all the encouragement and support.

REFERENCES

Ahrens, C. D., 2012. *Meteorology Today: An Introduction to Weather, Climate, and the Environment.* s.l.:Cengage Learning.

Anon., n.d. *Sky and Telescope.* [Online]
Available at: http://www.skyandtelescope.com/astronomy-news/observing-news/summer-quest-noctilucent-clouds/
[Accessed 5 August 2015].

Arnott, W., Dong, Y., Hallett, J. & Poellot, M., 1994. Role of small ice crystals in radiative properties of cirrus: A case study, FIRE II, November 22, 1991. *Journal of Geophysical Research: Atmospheres (1984-2012),* pp. 1371-1381.

Bailey, M. & Hallet, J., 2004. Growth rates and habits of ice crystals between-20 and-70 C. *Journal of the Atmospheric Sciences,* pp. 514-544.

Bailey, M. & Hallett, J., 2002. Nucleation effects on the habit of vapour grown ice crystals from− 18 to− 42 C. *Quarterly Journal of the Royal Meteorological Society,* pp. 1461-1483.

Bailey, M. & Hallett, J., 2008. A comprehensive habit diagram for atmospheric ice crystals: Confirmation from the laboratory, AIRS II, and other field studies.. *Journal of the Atmospheric Sciences 66(9),* pp. 2888-2899..

Bailey, M. & Hallett, J., 2009. A comprehensive habit diagram for atmospheric ice crystals: Confirmation from the laboratory, AIRS II, and other field studies. *Journal of the Atmospheric Sciences,* pp. 2888-2899.

Bailey, M. & Hallett, J., 2009. A comprehensive habit diagram for atmospheric ice crystals: Confirmation from the laboratory, AIRS II, and other field studies. *Journal of the Atmospheric Sciences 66(9),* pp. 2888-2899.

Baker, B. & Lawson, R., 2006. In situ observations of the microphysical properties of wave, cirrus, and anvil clouds. Part I: Wave clouds. *Journal of the Atmospheric Sciences,* pp. 3160-3185.

Barahona, D., Rodriguez, J. & Nenes, A., 2010. Sensitivity of the global distribution of cirrus ice crystal concentration to heterogeneous freezing. *Journal of Geophysical Research: Atmospheres (1984-2012).*

Baum, B. A. et al., 2011. Improvements in shortwave bulk scattering and absorption models for the remote sensing of ice clouds. *Journal of Applied Meteorology and Climatology,* pp. 1037-1056.

Baumgardner, D., Chepfer, H., Raga, G. B. & Kok, G. L., 2005. The shapes of very small cirrus particles derived from in situ measurements. *Geophysical Research Letters 32(1).*

Cactus2000, 2015. *Air Humidity Calculation.* [Online]
Available at: www.cactus2000.de/js/calchum.pdf

Cole, B. H. et al., 2013. Ice particle habit and surface roughness derived from PARASOL polarization measurements. *Atmospheric Chemistry and Physics,* pp. 3739-3750.

Connolly, P. et al., 2007. Calibration of the cloud particle imager probes using calibration beads and ice crystal analogs: The depth of field. *Journal of Atmospheric and Oceanic Technology,* pp. 1860-1879.

Connolly, P. J. et al., 2009. Studies of heterogeneous freezing by three different desert dust samples. *Atmospheric Chemistry and Physics,* pp. 2805-2824.

Connolly, P. et al., 2005. Aircraft observations of the influence of electric fields on the aggregation of ice crystals. *Quarterly Journal of the Royal Meteorological Society,* pp. 1695-1712.

Cotton, R. & Field, P., 2002. Ice nucelation of an isolated wave cloud. *Quarterly Journal of the Royal Meteorological Society 128(585),* pp. 2417-2437.

Cotton, R. & Field, P., 2002. Ice nucleation characteristics of an isolated wave cloud. *Quarterly Journal of the Royal Meteorological Society,* pp. 2417-2437.

Cotton, R. et al., 2013. The effective density of small ice particles obtained from in situ aircraft observations of mid-latitude cirrus. *Quarterly Journal of the Royal Meteorological Society, 139(676),* pp. 1923-1934.

Cotton, R. J. et al., 2013. The effective density of small ice particles obtained from in situ aircraft observations of mid-latitude cirrus. *Quarterly Journal of the Royal Meteorological Society,* pp. 1923-1934.

Cui, Z. et al., 2012. Aircraft measurements of wave clouds. *Atmospheric Chemistry and Physics 12(20),* pp. 9881-9892.

DeMott, P. J. & al., e., 1998. he role of heterogeneous freezing nucleation in upper tropospheric clouds: Inferences from SUCCESS. *Geophysical Research Letters,* pp. 1387-1390.

DMT, 2009. *Data Analysis Users Guide: Chapter 1: Single Particle Light Scattering.* [Online] [Accessed 29 September 2015].

Eidhammer, T. et al., 2010. Ice initiation by aerosol particles: Measured and predicted ice nuclei concentrations versus measured ice crystal concentrations in an orographic wave cloud. *Journal of the Atmospheric Sciences,* pp. 2417-2436.

Field, P. R. et al., 2003. A test of cirrus ice crystal scattering phase functions. *Geophysical Research Letters.*

Field, P. R. et al., 2012. Ice in clouds experiment-layer clouds. Part II: testing characteristics of heterogeneous ice formation in Lee wave clouds. *Journal of the Atmospheric Sciences,* pp. 1066-1079.

Field, P. R. et al., 2006. Some ice nucleation characteristics of Asian and Saharan desert dust. *Atmospheric Chemistry and Physics,* pp. 2991-3006.

Garrett, T. J., 2008. Observational quantification of the optical properties of cirrus cloud. *Light Scattering Reviews 3,* pp. 3-26.

Garrett, T. J., Hobbs, P. V. & Gerber, H., 2001. Shortwave, single-scattering properties of arctic ice clouds. *Journal of Geophysical Research: Atmospheres (1984-2012),* pp. 15155-15172.

Gayet, J. F. et al., 2012. On the observation of unusual high concentration of small chain-like aggregate ice crystals and large ice water contents near the top of a deep convective cloud during the CIRCLE-2 experiment. *Atmospheric Chemistry and Physics,* pp. 727-744.

Gayet, J. F. et al., 2011. Optical properties of pristine ice crystals in mid-latitude cirrus clouds: a case study during CIRCLE-2 experiment. *Atmospheric Chemistry and Physics,* pp. 2537-2544.

Gordon, A., 1998. *Dynamic Metorology: A Basic Course.* s.l.:Arnold.

Guignard, A., Stubenrauch, C., Baran, A. & Armante, R., 2012. Bulk microphysical properties of semi-transparent cirrus from AIRS: a six year global climatology and statistical analysis in synergy with geometrical profiling data from CloudSat-CALIPSO. *Atmsopheric Chemistry and Physics,* pp. 503-525.

Haag, W. & Kärcher, B., 2004. The impact of aerosols and gravity waves on cirrus clouds at midlatitudes. *The Journal of Geophysical Research: Atmospheres (1984-2012).*

Hallett, J., 1987. Faceted Snow Crystals. *JOSA,* pp. 581-588.

Hamblyn, R., 2008. *The Cloud Book: How to Understand the Skies.* first ed. UK: David and Charles.

Hamblyn, R., 2008. *The Cloud Book: How to Understand The Skies.* s.l.:F+W Media.

Hamblyn, R., 2009. *Extraordinary Clouds: Skies of the Unexpected from the Beautiful to the Bizarre.* s.l.:F+W Media.

Hargreaves, J. K., 1992. *The Solar-Terrestrial Environment: An Introduction to Geospace - the Science of the Terrestrial Upper Atmosphere, Ionosphere, and Magnetosphere.* s.l.:Cambridge University Press.

Hendricks, J., Kärcher, B. & Lohmann, U., 2011. Effects of ice nuclei on cirrus clouds in a global climate model. *Journal of Geophysical Research: Atmospheres (1984-2012).*

Heymsfield, A. J. & al, e., 1998. Upper-tropospheric relative humidity observations and implications for cirrus ice nucleation. *Geophysical Research Letters,* pp. 1343-1346.

Holler, S. et al., 1998. Two-dimensional angular optical scattering for the characterization of airborne microparticles. *Optics Letters,* pp. 1489-1491.

Holler, S. et al., 2004. Multivariate analysis and classification of two-dimensional angular optical scattering patterns from aggregates. *Applied Optics,* pp. 6198-6206.

Hoyle, C. R., Luo, B. P. & Peter, T., 2005. The origin of high ice crystal number densities in cirrus clouds. *Journal of the Atmospheric Sciences,* pp. 2568-2579.

Immler, F. et al., 2008. Cirrus, contrails, and ice supersaturated regions in high pressure systems at northern mid latitudes. *Atmospheric Chemistry and Physics,* pp. 1689-1699.

Irvine, E., Hoskins, B. & Shine, K., 2012. The dependence of contrail formation on the weather pattern and altitude in the North Atlantic. *Geophysical Research Letters,* 39(12).

Jakob, C., 2002. Ice clouds in numerical weather prediction models. *Cirrus,* pp. 327-345.

Jensen, E. J. et al., 2001. Prevalence of ice-supersaturated regions in the upper troposphere: Implications for optically thin ice cloud formation. *Journal of Geophysical Research,* pp. 17253-17266.

Jones, R. & Wykes, C., 1989. *Holographic and Speckle Interferometry, second edition.* s.l.:Cambridge University Press.

Jourdan, O. et al., 2010. Coupling of the microphysical and optical properties of an Arctic nimbostratus cloud during the ASTAR 2004 experiment: Implications for light-scattering modeling. *Journal of Geophysical Research: Atmospheres (1984-2012).*

Kärcher, B. & Lohmann, U., 2003. A parameterization of cirrus cloud formation: Heterogeneous freezing. *Journal of Geophysical Research: Atmospheres (1984-2012).*

Kaye, P. H. et al., 2008. Classifying atmospheric ice crystals by spatial light scattering. *Optics Letters,* pp. 1545-1547.

Kaye, P. et al., 2008. Classifying atmospheric ice crystals by spatial light scattering. *Optics Letters 33(13),* pp. 1545-1547.

Keller, V. W. & Hallett, J., 1982. Influence of air velocity on the habit of ice crystal growth from the vapor. *Journal of Crystal Growth,* pp. 91-106.

Kobayashi, T. & Ohtake, T., 1974. Hexagonal twin prisms of ice.. *Journal of the Atmospheric Sciences, 31(5),* pp. 1377-1383.

Korolev, A. et al., 2011. Small ice particles in tropospheric clouds: Fact or artifact? Airborne Icing Instrumentation Evaluation Experiment. *Bulletin of the American Meteorological Society,* pp. 967-973.

Korolev, A., Strapp, J., Isaac, G. & Nevzorov, A., 1998. The Nevzorov airborne hot-wire LWC-TWC probe: Principle of operation and performance characteristics. *Journal of Atmospheric and Oceanic Technology 15(6),* pp. 1495-1510.

Krämer, M. et al., 2009. Ice supersaturations and cirrus cloud crystal numbers. *Atmospheric Chemistry and Physics,* pp. 3505-3522.

Krämer, M. et al., 2009. Ice supersaturations and cirrus cloud crystal numbers. *Atmospheric Chemistry and Physics,* 9(11), pp. 3505-3522.

Lamb, D. & Verlinde, J., 2011. *Physics and Chemistry of Clouds.* s.l.:Cambridge University Press.

Lampert, A. et al., 2009. Microphysical and radiative characterization of a subvisible midlevel Arctic ice cloud by airborne observations–a case study. *Atmospheric Chemistry and Physics,* pp. 2647-2661.

Liou, K. N. & Takano, Y., 1994. Light scattering by nonspherical particles: remote sensing and climatic implications. *Atmospheric Research,* pp. 271-298.

Liou, K., Takano, Y. & Yang, P., 1999. Light scattering and radiative transfer in ice crystal clouds: Applications to climate research. In: *Light Scattering by Nonspherical Particles: Theory, Measurements, and Applications.* s.l.:Academic Press, pp. 417-449.

McFarquhar, G. M. & Heymsfield, A. J., 1996. Microphysical characteristics of three anvils sampled during the Central Equatorial Pacific Experiment. *Journal of the Atmospheric Sciences,* pp. 2401-2423.

Mitchell, D. et al., 1996. Modeling cirrus clouds. Part I: Treatment of bimodal size spectra and case study analysis. *Journal of the Atmospheric Sciences,* pp. 2952-2966.

Mitchell, D. L. et al., 1996. Modeling cirrus clouds. Part I: Treatment of bimodal size spectra and case study analysis. *Journal of the Atmospheric Sciences,* pp. 2952-2966.

Mitchell, D. L., Liu, Y. & Macke, A., 1996b. Modeling cirrus clouds. Part II: Treatment of radiative properties. *Journal of the Atmospheric Sciences,* pp. 2967-2988.

Mitchell, D. L. et al., 2008. Impact of small ice crystal assumptions on ice sedimentation rates in cirrus clouds and GCM simulations. *Geophysical Research Letters.*

Möhler, O. et al., 2006. Efficiency of the deposition mode ice nucleation on mineral dust particles. *Atmospheric Chemistry and Physics,* pp. 3007-3021.

Murphy, D. & Koop, T., 2005. Review of the vapour pressures of ice and supercooled water for atmospheric applications. *Quarterly Journal of the Royal Meteorological Society 131(608),* pp. 1539-1565.

NASA, 2010. *NASA Earth Observatory.* [Online]
Available at: http://earthobservatory.nasa.gov/Features/CarbonCycle/page5.php
[Accessed 28 August 2015].

NASA, 2015a. *NASA Terra Satellite.* [Online]
Available at: http://terra.nasa.gov/about
[Accessed 27 October 2015].

NASA, 2015b. *NASA MODIS.* [Online]
Available at: http://eartheobservatory.nasa.gov/GlobalMaps/view.php?d1=MODAL2_M_CLD_FR
[Accessed 5 August 2015].

Nazaryan, H., McCormick, M. & Menzel, W., 2008. Global characterization of cirrus clouds using CALIPSO data. *Journal of Geophysical Research: Atmospheres (1984-2012).*

NC-Climate, n.d. *NC-Climate.* [Online]
Available at: http://www.nc-climate.nscu.edu/edu/k12/.WaterCycle
[Accessed 8 August 2015].

Nelson, J., 1998. Sublimation of Ice Crystals. *Journal of the Atmospheric Sciences, 55(5),* pp. 910-919.

Neshyba, S. P. et al., 2013. Roughness metrics of prismatic facets of ice. *Journal of Geophysical Research: Atmospheres,* pp. 3309-3318.

Orikasa, N. & Murakami, M., 2015. Ice Crystal Shapes in Midlatitude Cirrus Clouds Derived from Hydrometeor Videosonde (HYVIS) Observations.

Pfalzgraff, W. C., Hulscher, R. M. & Neshyba, S. P., 2010. Scanning electron microscopy and molecular dynamics of surfaces of growing and ablating hexagonal ice crystals. *Atmospheric Chemistry and Physics, 10(6),* pp. 2927-2935.

Popp, P. et al., 2007. Condensed-phase nitric acid in a tropical subvisible cirrus cloud. *Geophysical Research Letters.*

Saha, K., 2008. *The Earth's Atmosphere: Its Physics and Dynamics.* s.l.:Springer.

Salby, M. L., 2012. *Physics of the Atmosphere and Climate.* s.l.:Cambridge University Press.

Sanderson, B. M. et al., 2008. Towards constraining climate sensitivity by linear analysis of feedback patterns in thousands of perturbed-physics GCM simulations. *Climate Dynamics,* pp. 175-190.

Shcherbakov, V. et al., 2006. Light scattering by single ice crystals of cirrus clouds. *Geophysical Research Letters, 33(15).*

Spichtinger, P. & Gierens, K., 2009. Modelling of cirrus clouds – Part 2: Competition of different nucleation mechanisms. *Atmospheric Chemistry and Physics,* pp. 2319-2334.

Stith, J. L. et al., 2002. Microphysical observations of tropical clouds. *Journal of Applied Meteorology,* pp. 97-117.

Stubenrauch, C. J. et al., 2006. Cloud Properties and their seasonal and diurnal variability from TOVS Path-B. *Journal of Climate,* pp. 5531-5553.

Ulanowski, Z., 2005. Ice analog halos. *Appl. Opt. 44(27),* pp. 5754-5758.

Ulanowski, Z., Hesse, E., Kaye, P. H. & Baran, A. J., 2006. Light scattering by complex ice-analogue crystals. *Journal of Quantitative Spectroscopy and Radiative Transfer,* pp. 382-392.

Ulanowski, Z., Hirst, E., Kaye, P. & Greenaway, R., 2012b. Retrieving the size of particles with rough and complex surfaces from two-dimensional scattering patterns. *Journal of Quantitative Spectroscopy and Radiative Transfer,* pp. 2457-2464.

Ulanowski, Z. et al., 2014. Incidence of rough and irregular atmospheric ice particles from Small Ice Detector 3 measurements. *Atmospheric Chemistry and Physics, 14(3),* pp. 1649-1662.

Ulanowski, Z. et al., 2012. *Rough and Irregular Ice Crystals in Mid-Latitude Clouds.* s.l., s.n.

Ulanowski, Z. et al., 2014. Incidence of rough and irregular atmospheric ice particles from Small Ice Detector 3 measurements. *Atmospheric Chemistry and Physics,* pp. 1649-1662.

Ulanowski, Z. et al., 2014. Incidence of rough and irregular atmospheric ice particles from Small Ice Detector 3 measurements. *Atmospheric Chemistry and Physics, 14(3),* pp. 1649-1662.

Van Diedenhoven, B., Fridlind, A. M., Ackerman, A. S. & Cairns, B., 2012. Evaluation of hydrometeor phase and ice properties in cloud-resolving model simulations of tropical deep convection using radiance and polarization measurements. *Journal of Atmospheric Sciences,* pp. 3290-3314.

Vance, A., Abel, S., Cotton, R. & Woolley, A., 2014. Performance of WVSS-II hygrometers on the FAAM Research Aircraft. *Atmospheric Measurement Techniques Discussions 7 ,* pp. 8643-8667.

Vance, A. et al., 2011. Final Report on the WVSS-II Sensors fitted to the FAAM BAe 146. *Met Office,* pp. 0-31.

Videen, G. et al., 1998. Asymmetry parameter and aggregate particles. *Applied Optics, 37(6),* pp. 1104-1109.

Voigtlaender, J. et al., 2013. A new experimental setup to investigate nucleation, dynamic growth and surface properties of single ice crystals. *EGU General Assembly Conference Abstracts,* Volume 15, p. 4206.

Wendisch, M. & Brenguier, J., 2013. *Airborne Measurements for Environmental Research.* Wienheim: WILEY-VCH.

Yang, P. et al., 2013. Spectrally consistent scattering, absorption, and polarization properties of atmospheric ice crystals at wavelengths from 0.2 to 100 µm. *Journal of the Atmospheric Sciences,* pp. 330-347.

Yang, P. & Liou, K., 1998. Single-scattering properties of complex ice crystals in terrestrial atmosphere.. *Beitrage zur Physik der Atmosphare-Contributions to Atmospheric Physics, 71(2),* pp. 223-248.

Yi, B. et al., 2013. Influence of ice particle surface roughening on the global cloud radiative effect. *Journal of the Atmospheric Sciences,* pp. 2794-2807.

Yi, B. et al., 2013. Influence of ice particle surface roughening on the global cloud radiative effect. *Journal of the Atmospheric Sciences,* 70(9), pp. 2794-2807.

Zhang, Y., Macke, A. & Albers, F., 1999. Effect of crystal size spectrum and crystal shape on stratiform cirrus radiative forcing. *Atmospheric Research,* pp. 59-75.